Developing Structural Mass Spectrometry Approaches for Therapeutic Antibody Characterization

by

Yuwei Tian

A dissertation submitted in partial fulfillment
of the requirements for the degree of
Doctor of Philosophy
(Chemistry)
in The University of Michigan
2018

Doctoral Committee:

Professor Brandon T. Ruotolo, Chair
Professor Kristina I. Håkansson
Professor Robert T. Kennedy
Assistant Professor Anna Schwendeman
Professor Steven P. Schwendeman

Yuwei Tian

yuwtian@umich.edu

ORCID iD: 0000-0002-7715-9875

DEDICATION

I dedicate this dissertation to my parents: Gang Tian and Xinke Li. Without their love and support, this accomplishment would not have been possible.

ACKNOWLEDGEMENTS

First and foremost, I would like to acknowledge my advisor, Professor Brandon T. Ruotolo, for his guidance and support during the past five years. His enthusiasm and excellence in science have inspired me to pursue my scientific goals with passion. Without Brandon's continuous encouragement and insightful advice, I would not have achieved what I did.

I would also like to thank Professors Robert Kennedy, Kristina Håkansson, Anna Schwendeman, and Steven Schwendeman for serving as my committee members. Their insightful questions and advice helped improve my understanding of my research, and contributed to the composition of this dissertation.

Over the past five years, I have had the great privilege to work with a group of excellent peer scientists, both in our lab, in the chemistry department, and across the campus. The Ruotolo lab has always been filled with intelligent and kind people who have offered me immense help during my entire time of graduate school. Special thanks to Linjie Han, who trained me on the instruments and guided me into the biotherapeutic field when I joined the lab. I'm also thankful for working with other senior lab members, Yueyang Zhong, Russ Bornschein, Molly Hopper, and Shuai Niu, who have always been helpful when I had any questions in the lab. Warm thanks to Jessica Gibbons and Joseph Eschweiler, who have developed the CIUSuite platform, making the data generation and processing for my whole dissertation way much easier. It's been an honor to work with these two great scientists on the CIU development. Other lab members whom I have spent the majority of time in my graduate school with are also of great inspiration. Sugyan Dixit, Dan Polasky, Sarah

Fantin, Chunyi Zhao, and Cara D'Amico, thank you for all your critical insights and comments. I really enjoyed our discussions both in the lab and outside the lab. Daniel Vallejo, I'm sure you will be the expert in biotherapeutics and take this project to the whole new level. Furthermore, I would like to thank all my collaborators, especially Karthik Pisupati, Jukyung Kang, and Alex Benet from the Schwendeman Group, and Iain Campuzano, Jennifer Lippens, and Chawita (Jelly) Netirojjanakul at Amgen. I would also like to acknowledge my supervisors during my Eli Lilly internship, Ning Wang and Lihua Huang.

Last but not least, I would like to express my special thanks to my family. My parents have been extremely supportive over the past few years. I would not have made this far without their unconditional love and care. For my husband, Yang Gao, who has always been there for me with patience, love and support.

Table of Contents

LIST OF FIGURES

LIST OF TABLES

LIST OF APPENDICES

LIST OF ABBREVIATIONS

AC	alternating current
ADC	antibody drug conjugate
ADCC	antibody dependent cell-mediated cytotoxicity
ADH	alcohol dehydrogenase
AS	ankylosing spondylitis
ATD	arrival time distribution
AUC	analytical ultracentrifugation
bsAb	bispecific antibody
CCS	collision cross sections
CD	circular dichroism
CDC	complement dependent cytotoxicity
CDR	complementarity-determining regions
CE	capillary electrophoresis
CID	collision induced dissociation
cIEF	capillary isoelectric focusing
CIU	collision induced unfolding
Con A	concanavalin A
CQA	critical quality attribute
CRM	charged residue model
CXL	chemical cross-linking
DAR	drug-to-antibody ratio
DC	direct current
DLS	dynamic light scattering
DNA	deoxyribonucleic acid
DSC	differential scanning calorimetry

DT	drift tube
EDTA	ethylenediaminetetraacetic acid
ESI	electrospray ionization
Fab	antigen binding fragment
Fc	crystallizable fragment
FDA	Food and Drug Administration
FPOP	fast photochemical oxidation of proteins
FTICR	Fourier transform ion cyclotron resonance
Fuc	fucose
FWHM	full width at half maximum
Gal	galactose
GlcNAc	N-acetylglucosamine
HC	heavy chain
HDX	hydrogen/deuterium exchange
HIC	hydrophobic interaction chromatography
HILIC	hydrophilic interaction chromatography
HOS	higher order structure
IBD	inflammatory bowel disease
IEM	ion evaporation model
IEX	ion-exchange chromatography
Ig	immunoglobulin
IM-MS	ion mobility-mass spectrometry
IV	intravenous
LC	light chain, liquid chromatography
LLPS	liquid-liquid phase separation
m/z	mass-to-charge
mAbs	monoclonal antibodies
MALDI	matrix-assisted laser desorption ionization
MAM	multiple attribute monitoring
MS	mass spectrometry
nESI	nano-electrospray ionization

NMR	nuclear magnetic resonance spectroscopy
PBS	phosphate buffer saline
PD	pharmacodynamics
PDB	Protein Database Bank
PK	pyruvate kinase, pharmacokinetics
PTM	post-translational modification
RA	rheumatoid arthritis
RC	Remicade
RF	radiofrequency
RMSD	root-mean-square deviation
RPLC	reversed phase liquid chromatography
RS	Remsima
S.D.	standard deviation
SAP	spatial aggregation propensity
SC	subcutaneous
SEC	size exclusion chromatography
TEM	transmission electron microscopy
TNFα	tumor necrosis factor α
ToF	time-of-flight
TWIM	traveling wave ion mobility
UV	ultraviolet
XRD	X-ray diffraction

ABSTRACT

Therapeutic monoclonal antibodies (mAbs) and mAb-based therapeutics represent the fastest growing class of biopharmaceuticals over the past few decades. In comparison with the small molecule drugs, these large complex biomolecules offer higher specificity, efficacy, and fewer side effects, owing to their diverse compositions and modes of action. The comprehensive structural characterization of therapeutic antibodies is of critical importance for the successful discovery and development of such biopharmaceuticals, yet poses many challenges to modern measurement science. To address these challenges, in this dissertation we develop structural mass spectrometry-based approaches, including ion mobility-mass spectrometry (IM-MS) combined with collision induced unfolding (CIU) methods, and hydrogen/deuterium exchange mass spectrometry (HDX -MS), for assessing the structure, stability, and dynamics of such therapeutics.

First, we demonstrated the capacity of CIU for characterizing intact antibodies with minimal sample preparation and purification. In Chapter 2, four human IgG isoforms containing different disulfide bridges were rapidly differentiated using CIU. The CIU analysis was also able to capture the conformational changes in the mAb induced by the removal of entire glycans from the protein. Furthermore, we validated this CIU protocol through a systematic statistical evaluation of its reproducibility. In Chapter 3, we evaluated the ability of CIU to detect the impact of subtle changes to N-linked glycan composition on overall antibody structure. Subtle structural alterations and decrease in gas-phase stabilities were detected in both intact mAbs and antibody Fc fragments, as a result of sequential eliminations of terminal sugars in the glycosylation. We found evidence for

a strong correlation between the gas-phase stabilities of antibody ions and the amount of sugars attached to their sequences.

We continued by developing native IM-MS methods in combination with CIU analysis for characterization antibody drug conjugates (ADCs) in Chapter 4. By using mAb-biotin conjugates as model ADCs, we show that despite nearly identical ground state structures, subtle structural differences can be detected upon biotin conjugation using CIU. Our analysis involves the global comparison of CIU datasets, width analysis of the arrival time distributions, and the detection of gas-phase unfolding transitions. We then integrated the native IM-MS and CIU approaches with other state-of-the-art MS techniques for a comprehensive evaluation of the biosimilar and originator infliximab in Chapter 5. These two mAb products displayed identical primary structures, highly similar modifications, comparable higher order structures, and similar degradation pathways under stress. However, the differences in the glycoforms and Fc receptor bindings were observed, suggesting potential differences in the efficacy profiles for these two drugs.

Finally, a novel HDX-MS strategy was developed in Chapter 6 for high concentration mAb formulations. This method was used to study the liquid-liquid phase separation behavior of an IgG4. Decreased deuterium uptake levels were observed for mAbs in the high-density phase compared to those in the depleted lower density phase, revealing evidence of conformational changes for this mAb as a function of overall protein concentration.

Chapter 1. Introduction

Elements of this chapter are taken from:

Yuwei Tian, Brandon T. Ruotolo, The Growing Role of Structural Mass Spectrometry in the Discovery and Development of Therapeutic Antibodies, *Analyst*, 2018, (DOI:10.1039/c8an00295a.)

1.1 Therapeutic Antibody and Related Products

Over the past few decades, biopharmaceuticals have emerged as an important class of therapies, evidenced by the number of approved therapies in this class for indications ranging from cancers to autoimmune diseases.[1] This family of pharmaceuticals comprises a variety of engineered biomolecular products, such as protein-based and gene-based therapeutics, with diverse compositions and mechanisms of action. Monoclonal antibodies (mAbs) and related therapeutics, such as antibody-drug conjugates (ADCs) and bispecific antibodies (bsAbs), are undoubtedly the most promising and fastest growing of these subclasses, owing to their high specificity, high efficacy and fewer side effects.[2–6] Since the approval of the first mAb product in 1986, the market of mAb products has increased dramatically. In 2013, mAbs accounted for global sales of nearly $75 billion taking up ~50% of the total sales of all biopharmaceutical products.[1] However, as the benefits of biopharmaceuticals are often attributed to their complex molecular compositions and diverse conformations, the challenging task of their comprehensive biophysical characterization is exceptionally important during discovery and development.

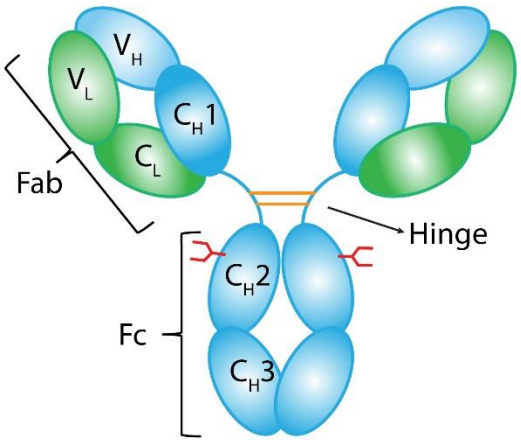

Figure 1-1. Cartoon of an IgG antibody. Light chains are shown in green and the heavy chains are shown in blue.

1.1.1 Structure of mAbs and Related Therapeutics

Antibodies also known as immunoglobulins (Ig) are glycoproteins produced by the body's immune system in response to antigens. Over all five classes of human antibodies – IgA, IgD, IgE, IgG, and IgM, antibodies have a general Y-shaped structure. Despite of the commonality in the individual unit structure, antibody classes have different propensities for forming oligomers, with IgA found in the dimeric form and IgM in the pentameric form.[7] Of the five antibody classes, IgGs have been the dominant antibody class used as therapeutics, with more than forty products approved and marketed in the United States and Europe.[3,8]

Naturally occurring IgGs are ~150 kDa proteins consisting of two identical light chains (~25 kDa each) and two identical heavy chains (~50 kDa each) held in place by inter- and intra-chain disulfide bonds as well as noncovalent interactions (Figure 1-1).[9] The variable domains of the light chains and heavy chains (V_H and V_L) are responsible for highly specific antigen-binding. The constant region of light chains (C_L) interacting with the first constant domain of heavy chains (C_H1), along with the variable domains are known as the antigen binding fragment (Fab). The two heavy chains are connected in the hinge region through disulfide bonds and further secured by the interactions in the crystallizable fragment (Fc) that consists of heavy chain constant domains C_H2 and C_H3. The Fc region accounts for the effector function, i.e., antibody dependent cell-mediated cytotoxicity (ADCC) and complement dependent cytotoxicity (CDC).[4] All mAbs are

glycoproteins containing one conserved N-glycosylation site in the C_H2 domain of each heavy chain.[10,11] These sites are typically occupied by complex biantennary oligosaccharides containing a core heptasaccharide structure with variable addition of outer arm sugar residues, such as fucose and galactose. These N-linked glycans are known to play a key role in antibody effector function, immunogenicity, plasmatic clearance, and resistance towards proteases.

The large-scale production of mAbs is typically achieved through recombinant DNA technology, generating bulk drug substances with homogeneous primary sequence.[12,13] However, structural heterogeneities in the mAbs often can be found resulting from the post-translational modifications (PTMs) or degradations that can occur during multiple stages of production, from upstream cell culture to downstream purification and formulation. Those modifications and degradation products have been widely reported including deamidation, oxidation, disulfide shuffling, sequence variants, glycation, N-terminal pyroglutamate formation, C-terminal lysine truncation, aggregation, etc.[9,14] These inherent heterogeneities could potentially alter protein functions, affect the drug efficacy, and raise safety risks.[15]

In comparison with the naturally occurring mAbs, mAb related drug products can possess a greater level of complexity. For instance, antibody-drug conjugates (ADCs) are mAbs covalently attached to highly potent small-molecule drugs via labile linkers.[5,16,17] Most ADCs are either conjugated at the cysteine residues available from interchain disulfide reduction or linked at the lysine residues. Linkers can be either cleavable or non-cleavable. Thus, the diverse conjugation strategies could add to the complexity of ADCs. They are often highly heterogeneous regarding the drug loads and distribution, in addition to the inherent structural heterogeneities of the parent mAb. Bispecific mAbs are hybrid proteins comprised of fragments from two antibodies, allowing the ability to target two different antigens simultaneously.[18,19] The production process for such bispecific mAbs

is intrinsically more complicated compared to the production of standard mAbs, resulting in various molecular species associated with unintended light chain and heavy chain combinations.

1.1.2 Toolbox for mAb Structural Characterization

The biological activity, pharmacokinetics (PK) and pharmacodynamics (PD) of a mAb are usually key determinants for its clinical success. These factors, along with the clearance, safety, and immunogenicity of biopharmaceuticals are all highly dependent upon protein structures.[20] In this scenario, a comprehensive understanding of both mAb activities and structures can help rationally engineer candidate molecules that are more efficacious, homogeneous, and stable, with higher possibility of success. Thus, all the structural properties and stabilities of the protein therapeutics have to be fully assessed during development and closely monitored prior to commercial release.

One of the most important analytical techniques for mAb characterization is liquid chromatography (LC), which has been widely utilized to separate mAb main isoform from the variants and impurities.[21,22] Instrument manufacturers offer a wide range of LC columns packed with particles having various sizes, porosities, and modifications to meet diverse analytical needs in biopharmaceutical industry. Among all types of chromatographic methods, ion-exchange (IEX), hydrophobic interaction (HIC), hydrophilic interaction (HILIC), reversed phase (RPLC), size exclusion (SEC) chromatography are most used in the discovery and development of mAbs. These LC techniques can characterize mAbs at multiple levels, from intact mAb and protein subunit characterization, to peptide and glycan analysis. IEX can separate the target mAb from process impurities.[23] IEX is also largely utilized for profiling the charge heterogeneity of mAbs, arising from modifications such as C-terminal lysine truncation, deamidation, glycation, etc.[24,25] SEC separates analytes based on their size or molecular weight and can use mild mobile phase

conditions that are close to physiological pH and ionic strength, allowing for the retention of native mAb conformations.[26] Therefore, SEC is mostly used to characterize antibody aggregation and fragmentation.[27,28] RPLC separates molecules according to their hydrophobicity and is a highly robust technique suitable for use in a routine environment, i.e. quality control before releasing batches to clinical use.[29] When choosing appropriate RPLC column and mobile phase gradient, RPLC separation can be performed at various levels, e.g. intact protein, subunits, and peptides level. As RPLC is the compatibility with MS detection given the volatile solvent, both identity and quantity information on the analytes and impurities can be obtained. HIC is another type of chromatographic mode that separates molecules based on hydrophobicity, but without using organic solvent for mobile phase.[30] Thus, HIC has been widely used for characterizing drug loading in ADCs, as the conjugation of small molecule drugs typically alters mAb hydrophobicity.[31]

In addition to chromatographic methods, the toolbox for mAbs structural characterization also includes many biophysical techniques capable of producing information at various levels of resolution. For example, X-ray diffraction (XRD)[32] and nuclear magnetic resonance spectroscopy (NMR)[33] are both capable of the direct characterization of protein structure at atomic resolution. Since the very first X-ray crystal structures of antibodies were solved in the 1970s, many atomic structures of antibody fragments and associated complexes have been deposited into the Protein Database Bank (PDB).[34] Despite this, intact antibodies are difficult to crystalize because of their structural flexibility and heterogeneity, resulting in only four intact IgG structures currently available in the PDB.[35–38] In addition, there are long-standing questions surrounding the relationship between the mAb XRD data and native protein structures in solution. NMR, in contrast to XRD, is capable of characterizing protein structures and dynamics in solution at atomic

resolution.[39] This technique works by measuring the magnitude of nuclear magnetic moments of the nuclei immersed in a static magnetic field and exposed to a second oscillating magnetic field. Many parameters measured by NMR, such as dipolar cross relaxation (NOE) rate constants and scalar coupling constants, are sensitive to protein conformation, thus can be used as restraints for protein structure determination.[40] Nonetheless, NMR may not be suitable for biopharmaceutical development mainly due to its requirement of large amount of protein samples and limitations associated with high molecular weight and sample heterogeneity, leading to line broadening that results in a significant decrease in spectral information content.

In order to meet the requirements of higher order structure (HOS) characterization in the developmental stages of therapeutic antibodies, the pharmaceutical industry has long relied upon an array of biophysical assays including: circular dichroism (CD), Fourier-transform infrared spectroscopy (FTIR), and differential scanning calorimetry (DSC).[41–43] Although these techniques provide only low-resolution domain fingerprints of the mAbs, they are robust and amenable to the samples typically available during mAb development cycles. CD experiments provide direct information on the molecular configurations by measuring the differences between the left- and right-handed circular polarized light absorbed by the molecules.[44] CD signal in the far-UV wavelength range (190 – 250 nm) can characterize and quantify the content of protein secondary structures, as alpha-helix, beta-sheet, and unordered structure each gives rise to characteristic CD response.[45] Protein tertiary structures can also be monitored using the CD signals in the near UV region from 250 nm to 300 nm.[46] At these wavelengths, CD signals are attributed to the side chains of aromatic residues and disulfide bonds, and are sensitive to the changes in the environment of these moieties.[47,48] At global level, DSC is widely used to provide insights into the stability of protein folded structures by measuring the heat capacity changes associated with the transition of

protein unfolding at elevated temperatures.[49] During the development of biopharmaceuticals, this technique can be used to screen the candidate molecules with optimal stability profiles and identify proper solution conditions for long-term storage.[46,50]

Although the aforementioned analytical and biophysical assays have been successfully employed in the discovery and development of biopharmaceuticals, many challenges persist in their HOS characterization including: sample homogeneity requirements, low analysis throughput, and the low information content of the data typically collected. Recently, mass spectrometry has emerged to produce a family of methods aimed at addressing the structural complexity of biopharmaceuticals, providing such information on multiple levels. MS detectors coupled to LC approaches have been extensively used in the pharmaceutical industry for a variety of purposes, ranging from intact mass measurements to peptide mapping and impurity identification. Moreover, structural MS-based techniques have strengthened the capability of MS in terms of biophysical characterization of protein. When coupled to techniques such as ion mobility (IM) separation,[51] hydrogen-deuterium exchange (HDX),[52,53] chemical cross-linking (CXL),[54] and fast photochemical oxidation (FPOP),[55,56] MS can characterize protein global structures and local conformations. In this dissertation, IM-MS and HDX-MS strategies have been developed for therapeutic antibody structural characterization. The instrumentation and current application of structural MS in biopharmaceutical characterization will be discussed in the later part of this chapter.

1.2 Ion Mobility-Mass Spectrometry Instrumentation

IM was previously developed as an analytical tool for the detection of trace quantities of organic molecules.[57,58] With significant improvements over the past two decades, ion mobility-mass

spectrometry (IM-MS) coupled with soft ionization sources has evolved into a powerful platform for biological molecular analysis.[51,59] Very recently, the applications of IM-MS have expanded into the field of biopharmaceutical development.[60] In order to fully take advantage of modern IM-MS technology for biopharmaceutical structural characterization, it is essential to understand the fundamental of the instrumentation. Though many types of IM-MS instruments have been developed, the work discussed in this dissertation is exclusively performed on a Water Synapt G2 HDMS instrument which contains a traveling wave IM separator (TWIMS). A schematic of this instrumentation is shown in Figure 1-2 and each major component will be introduced in this section.

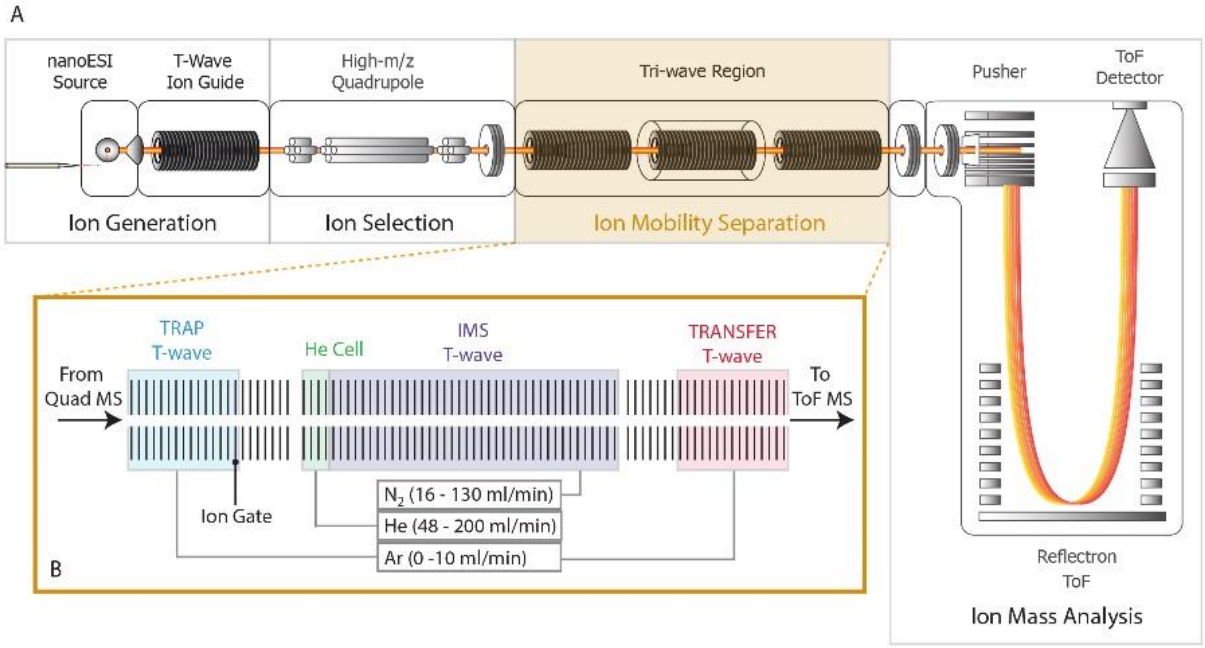

Figure 1-2. Schematic of Waters Synapt G2 HDMS. A) Overall diagram of the instrumentation composing of four main regions: nanoESI source for ion generation; a modified quadrupole for ion transmission and selection up to 32000 m/z; a traveling wave ion mobility separator; a reflector ToF device for mass analysis. B) A detailed schematic depicting the tri-wave region, including four components: two T-wave ion guides (trap and transfer region) pressurized with argon gas; T-wave IM separator pressurized with nitrogen gas; the helium cell acting as a buffer between the low-pressure trap and high-pressure IMS, minimizing ion activation.

1.2.1 Ion Generation and Preservation of Native Protein Structures

All mass spectrometric experiments start with converting analytes into ions in the gas phase. The introduction of soft ionization sources, such as matrix-assisted laser desorption ionization (MALDI)[61] and electrospray ionization (ESI)[62], over thirty years ago enabled the transfer of large biomolecules to the gas phase in their intact form, and has significantly strengthened various MS methods used to study biological molecules.[63,64] Commonly, MALDI generates singly charged ions by irradiating a pulsed laser to the sample mixed with an absorbing matrix. In contrast, ESI generates multiply charged ions directly from solution, allowing the detection of large biological molecules at lower mass-to-charge (m/z) range. Moreover, the ability to preserve noncovalent interactions has distinguished ESI for the study of protein complexes.

As shown in Figure 1-3, during ESI, a sample solution is infused into a metal or metal-coated capillary held at high voltage. For protein analysis, positive ion mode is commonly used, where a positive voltage is applied, accumulating cations at the tip of the capillary. The high electric field will polarize the solution at the capillary tip and cause a distortion of the solution surface to form a Taylor cone that emits a spray of droplets.[65] Often assisted by heating and nebulizing gas, the solvent evaporates rapidly form the droplets, resulting in decreased droplet radii. The charge density on the shrinking droplets increases until reaching the Rayleigh limit,[66] at which point Columbic repulsion is strong enough to overcome the surface tension and cause a jet fission to

produce smaller droplets. Recurrent evaporation/fission cycles eventually generate desolvated multiply charged analyte ions.

The vast majority of protein sequencing experiments are performed on ions produced under denaturing conditions in order to improve sequence coverage, in which acidified aqueous/organic mixture is used to promote protonation. In contrast, native MS experiments seek to make mass measurements of proteins while preserving their structure under native conditions, where pH and ionic strength are controlled to preserve protein structure and function.[67].[68] To enhance the intensities of mAb signals in native MS experiments, Nano-ESI (nESI), utilizing a miniaturized ESI emitter and nL/min flow rates, is often used in order to reduce ESI droplet sizes, increase overall ionization efficiency, and increase the overall tolerance of the ion source for salts and other common biotherapeutic excipients.[69,70] Ammonium acetate salts are often used to establish the ionic strength for samples to be analyzed by native MS due to their general volatility. Owing to their folded conformations, fewer total charges are deposited on the protein, resulting in a narrower charge envelope shifted towards greater mass-to-charge (m/z) values when compared to MS data often acquired under denaturing conditions.

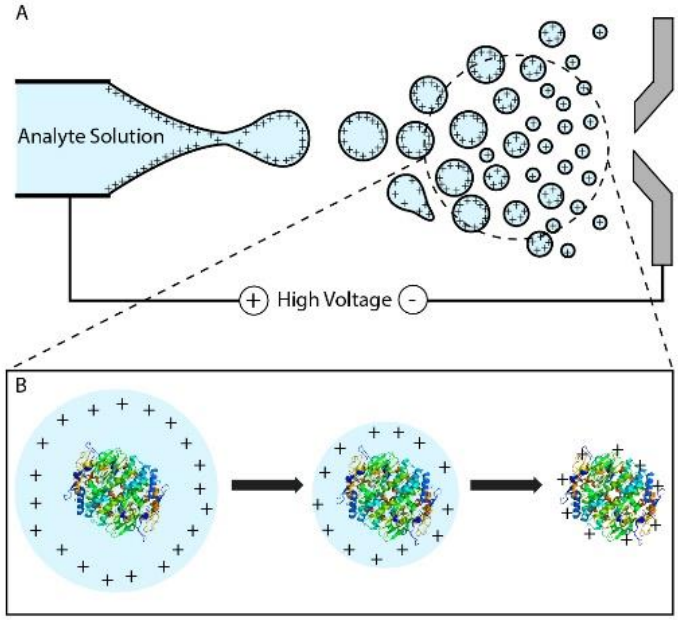

Figure 1-3. Electrospray ionization. A) Diagram of ESI source, including the emitter on the left and the source cone on the right. B) Schematic depiction of droplet evaporation during ESI, best described as Dole's charge residue model.

Though the mechanistic study of ESI process has proven to be challenging and remains debatable, several models have been proposed to explain how ions are formed in the final stages of ESI. Ion evaporation model (IEM) and charged residue model (CRM) are two most successful theories. IEM, first proposed by Iribarne and Thomson[71,72], suggest that the repulsion between analyte ion and excess droplet charges becomes large enough to eject ion directly into the gas phase, before solvation evaporation completes. This theory is well-supported by experiments for small molecules, however, does not apply for large analyte ions such as proteins and protein complexes. For large macromolecules, CRM proposed by Dole et al is widely accepted.[73] In this model, the analyte containing droplet undergoes continuous solvent evaporation/fission events governed by Rayleigh limit. The complete evaporation of solvation ultimately yields a macromolecule as a charge residue, holding the charge same as the last droplet approximating 90% of the Rayleigh limit. For the CRM, protein species remains folded during this slow and gentle process, allowing the retention of aspects of their native solution structure.

1.2.2 High Mass Transmission, Selection, and Detection

The majority of structural MS experiments are performed on hybrid mass spectrometers, combining a quadrupole mass analyzer with an orthogonal time-of-flight (ToF) mass analyzer. The ToF mass analyzer determines the mass-to-charge ratio of an ion by measuring the flight time of pulsed ions in a field-free drift tube given a fixed amount of kinetic energy.[74] The invention of reflectron ToF has largely improved the resolving power of this type mass analyzer in two ways: the correction of initial kinetic energy difference and the introduction of an elongated flight path.[75] A major breakthrough in the design of ToF mass analyzers coupled with ESI arose from the introduction of orthogonal ToFs, where the pulsed ions are extracted in the direction orthogonally from a continuous ion beam.[76] The advantages of high mass range and largely enhanced mass

resolution have made modern ToF mass analyzers extremely useful for protein and protein complex analysis.[77]

Another mass analyzer commonly used in structural MS is the quadrupole, comprising four conductive rods mounted in pairs arranged on two orthogonal planes, for which paired rods are held at the same potential comprised of both direct current (DC) potential and alternating current (AC) produced at an oscillating radiofrequency (RF).[78,79] The trajectory of ions is affected by the voltage applied on the rods, thus, only ions with certain m/z values can traverse the quadrupole for a given combination of DC and RF voltages. Though quadrupoles can operate as a stand-alone mass analyzer, in native MS experiments such devices are often combined with ToF mass analyzers, serving as a primary mass filter for tandem MS experiments. In this mode, ions with specific m/z can be selected by tuning the quadrupole to a specific set of DC and RF voltages. In other cases, the quadrupole can function as broad-band RF-only lens.

Despite the theoretically unlimited m/z range of the ToF instruments, the transmission of large protein ions in a Q-ToF device has proven to be challenging.[80] Several strategies have been utilized to improve the transmission efficiencies for such ions, including the manipulation of pressure gradients within the mass spectrometer can help improve large ion transmission. This can be achieved by either adding collision gas late in the ion path to damp ion kinetic energies just before ToF sampling, or by increasing the pressure in the initial lensing elements encountered by ions following their initial generation.[81,82] In both cases, the radial motions of large ions can be better thermalized at elevated pressures through collisions with gas molecules, resulting in significant improvements in ion transmission through the small apertures that define differential vacuum stages within the typical Q-ToF platform.[81]

1.2.3 IM Separation

IM can rapidly separate ions based on their charges and shapes in gas phase under the influence of a weak electric field.[83,84] In a typical IM experiment, packets of ions are introduced into an ion guide pressurized with inert neutral gas under the influence of a relatively weak electric field. (Figure 1-4) The larger, more-elongated ions collide more frequently with these gas molecules, and thus take a longer time to traverse the IM separator when compared to smaller and more-compact ions. The output of IM separations is the orientationally-averaged ion-neutral collision cross sections (CCS) for the ions analyzed, and this information can be readily extracted either directly from ion arrival times, or through careful calibration with ions of known CCS.[85] Furthermore, theoretical CCSs can be computed from protein structure models, as well as used as constraints for molecular dynamics simulations, enabling the detailed assessment of protein structural states in the gas phase.[86–88] IM separation can be performed on a wide range of platforms combined with MS detection. This introduction will focus on two types of IM devices operating at weak electric field: drift tubes (DTs) [89,90] and travelling wave ion mobility (TWIM) separators [91–93].

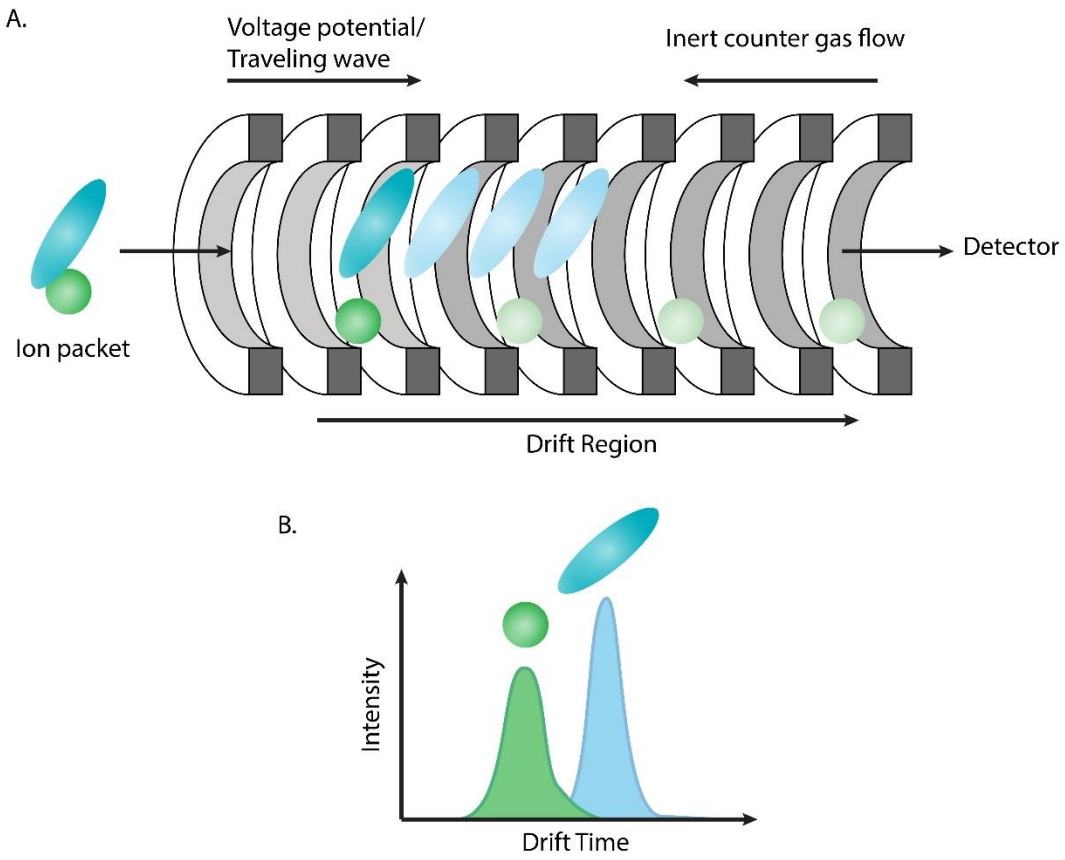

Figure 1-4. (A) The ion-mobility technique can separate different ions based on their shape and charge. Ions travel through an inert gas-filled drift tube by the influence of an electric field. Larger and more-elongated ions collide more frequently with the background gas molecules, thus take longer time to traverse the drift tube, compared with smaller and more-compact ions. (B) These ion profiles are recorded as arrival time distributions.

Drift tubes (DTs) are the conceptually simplest IM analyzer. Generally, DT devices are comprised of a series of stacked ring electrodes, where a static uniform electric field is established, and ions are propelled in the direction of the applied field. The length of the drift tube can range from centimeters to meters and the drift gas filled in the tube can be helium or nitrogen. Because the physical principles that dictate ion transport in DTs are well-understood, the CCS values of the analyte ions can be directly calculated from the drift times acquired under given conditions.[83] While the DT device has the advantage of high resolution over other types of IM instruments, early designs suffered from poor sensitivity and low duty cycles for large biomolecule analysis. To

overcome these limitations, the contemporary versions of these devices are often equipped with ion-trapping regions prior to the DT, and focusing elements after.[89]

Despite the simplicity of DT devices, the majority of IM-MS analyses carried out on large biological molecules has utilized travelling wave IMS (TWIMS) separators, the first IM device commercialized as an integrated element within an MS platoform.[91,94,95] TWIMS devices are constructed similar to DTs, but operate differently. Instead of a linear electric field gradient, TWIMS uses a dynamic, non-uniform field that pushes ions through the separator. Opposite phases of RF voltages are applied to adjacent electrodes to radially confine the ions, while the application of a transient DC pulse to the electrodes consecutively generates potential waves propagating through the tube. Thus, the applied DC pulses can create a "traveling wave" on which the ions "surf". Optimal mobility separation of ions can be achieved by tuning the TWIMS wave amplitude and wave velocity. Although TWIMS is a versatile platform that allows medium resolution IM separation within short device lengths with 100% transmission efficiency, due to the complexity of non-uniform filed applied, direct CCS calculation from measured drift time is currently challenging. Therefore, determination of CCS on this type of instrument is often achieved by calibrating ion drift times based on drift tube datasets.[96]

1.2.4 Collision Induced Unfolding (CIU)

As the size and complexity of biomolecules increase, IM measurement alone may not be sufficient to define detailed protein structures. Collision induced unfolding (CIU) can greatly enrich the information content of IM experiments via collisional activating ions in the gas phase. In a typical CIU experiment, target analyte ions filtered by quadrupole are activated through collisions with background gas molecules in the trap region. Collision voltages are increased in order to increase

the internal energy of the protein ions and cause them to unfold in the gas-phase.[97] The activated protein ions are then subject to the IM separation, in which the amount of conformational changes can be captured. CIU can be viewed as the gas-phase analogue to the differential scanning calorimetry (DSC) where the thermal denaturation is induced in the solution phase. The data generated from CIU experiment is often presented as a contour plot, or CIU "fingerprint", where the drift time is plotted against the collision voltage, and a color scale is used to denote the signal intensities.

Early CIU experiments have been focused on probing the differences in the gas-phase conformations and stabilities of small proteins at different charge states.[97,98] The application of CIU was then extended to detect the gas-phase stability changes of protein complexes upon ligand binding.[99] Modern implementation of CIU technology has been expanded to a wide range of applications, including studying the stability influence of anion and cation bindings,[100,101] distinguishing the structures of kinase-inhibitor complexes,[102] measuring the cooperativity effects of protein-ligand binding,[103] probing the lipid binding in membrane proteins,[104] and studying the protein domain structures.[105,106] The development of data processing software offers the quantitative analysis of CIU data with increased throughput and furthers the potential of this technique regarding protein structure and stability characterization.[104,107]

1.3 Structural Mass Spectrometry for Discovery and Development of Therapeutic Antibodies

With concomitant advances in sensitivity, resolution, accuracy, and speed, MS has been widely deployed for the characterization of therapeutic mAbs. In addition to elucidating mAb primary structures, MS methods are capable of probing the higher order structures and dynamics of

therapeutic mAbs. Recent works illustrate the versatility of MS in context of mAb structural characterization and the great potential of structural MS in the context of rapidly evolving biopharmaceutical analysis workflows.

1.3.1 Measuring the Stoichiometries of Antibody-associated Complexes

In the context of mAb analysis, native MS provides accurate intact masses as well as information on glycoform heterogeneity, antibody-antigen binding, and any oligomeric states present.[97–100] For example, native MS data acquired using a modified Orbitrap platform has been used to assign and quantify the heterogeneous glycoforms within a mAb sample.[98] In these spectra, a mass resolving power of up to 12000 at an m/z of 6000 could be achieved, allowing for the confident assignment of antibody glycoforms. In addition to the identification of PTM states, high-resolving power native MS has also been demonstrated to both qualitatively and quantitatively characterize antibody mixutres.[101,102] For example, Q-ToF based native MS has been used to resolve and quantify nine out of ten antibodies present within a mixture, whereas such a mixture could not be similarly unraveled by cation exchange chromatography.[101] Furthermore, using high-resolving power native MS, a mixture containing fifteen different antibodies, with mass differences ranging from 20.94 to 1149.41 Da were baseline resolved.[102] Triplicate native MS measurements showed excellent quantitative reproducibility, exhibiting less than 1.2% relative error in the ion intensity values recorded for the resolved mAbs.

The ability to preserve noncovalent protein-protein interactions during the ESI process in native MS workflows enables the direct measurement of antibody-antigen binding stoichiometries and stabilities. Pioneering work in this area[100] demonstrated that complexes formed between the recombinant V antigen (rV), a 37-kDa protein secreted by *Y. pestis*, and its complimentary mAb

could be readily detected and characterized. These native MS measurements revealed that the rV antigen forms a tightly associated dimer at micromolar concentrations, that a 1:2 binding stoichiometry is prevalent for the antibody:antigen complex, and quantified the resulting antibody-antigen binding specificity. Later work used native MS to investigate the immune complex formed between the recombinant JAM-A protein, as well as an antigenic protein (Ag) overexpressed in tumor cells, with both murine and humanized mAbs.[103] These data were used to determine both the mAb:antigen binding stoichiometry and selectivity, revealing similar values for both humanized and murine mAbs. As above, the advent of higher resolving power native MS platforms has also been leveraged for the analysis of antibody-antigen complexes.[98] Native MS is also a useful tool for characterizing antibody aggregates, which are common degradation products for therapeutic proteins, causing activity loss, decreased solubility, and enhanced unwanted immunogenicity. Because aggregation can occur during production, formulation and storage, it is critical to monitor aggregate formation through multiple stages of biopharmaceutical development. To this end, the chromatographic separation of protein oligomers was integrated with native MS in order to successfully detect soluble mAb oligomers induced by pH-stress.[97] In addition, native MS has been used to analyze the antigen binding stoichiometry of a functional IgG hexamer.[104] The resulting large multi-protein complex was further characterized by tandem MS, which provided critical information on the spatial arrangement and stoichiometry of the subunits within the assembly.

Antibody related drug products, such as bsAbs and ADCs, have also recently been characterized by native MS workflows. For instance, native MS was used to monitor Fab-arm exchange, a physiological process in which portions of two IgG4 mAbs recombine to form a bispecific antibody. [105] Fab-arm exchange was mimicked *in vitro* through the addition of a mild reducing

agent, and the dissociation kinetics of IgG4 were monitored by native MS. The results highlighted the importance of the C_H3 domain in the process that gives rise to the ultimate bsAbs. Native MS was also used to characterize cysteine-linked ADCs, yielding average drug-to-antibody ratio (DAR) values comparable to more time consuming hydrophobic interaction chromatography (HIC) analyses.[106,107] Recent work has also demonstrated the benefits of native MS for characterizing highly heterogeneous lysine-linked ADCs.[108,109] Average DAR values can be accurately deduced from native MS spectra collected for deglycoslyated lysine-linked ADC samples using high resolving power native MS. Furthermore, charge reduction approaches coupled to native MS analysis of ADCs has been used to reduce spectral complexity and decrease mass overlaps for the broadband measurement of highly accurate DAR values.[108]

1.3.2 HDX-MS Probing the Conformation and Dynamics of mAbs

HDX-MS has been used for over twenty-five years to study the dynamics of proteins in solution,[52,110,111] and is now increasingly applied to mAb analysis. Modern HDX-MS experiments can quantify the flexibility and stability of mAbs at the intact protein, peptide, and amino acid-level (Figure. 1-5). HDX-MS workflows are typically initiated through the exchange of labile backbone amide hydrogens by diluting protein samples into a D_2O-containing buffer, which is quenched by lowering the pH after a fixed amount of exchange time. The amount of deuterium uptake can be assessed by both top-down and bottom-up workflows, utilizing rapid activation tools in MS/MS mode experiments to assess exchange levels for individual residues within the protein, while the latter approach is currently more commonly deployed. As the HDX rate is related to protein folding structure and dynamics, differences in deuterium uptake level can be mapped on to protein structures to identify epitopes in antigen-antibody interactions, as well as examine local conformational changes of mAbs provoked by modifications.[112,113]

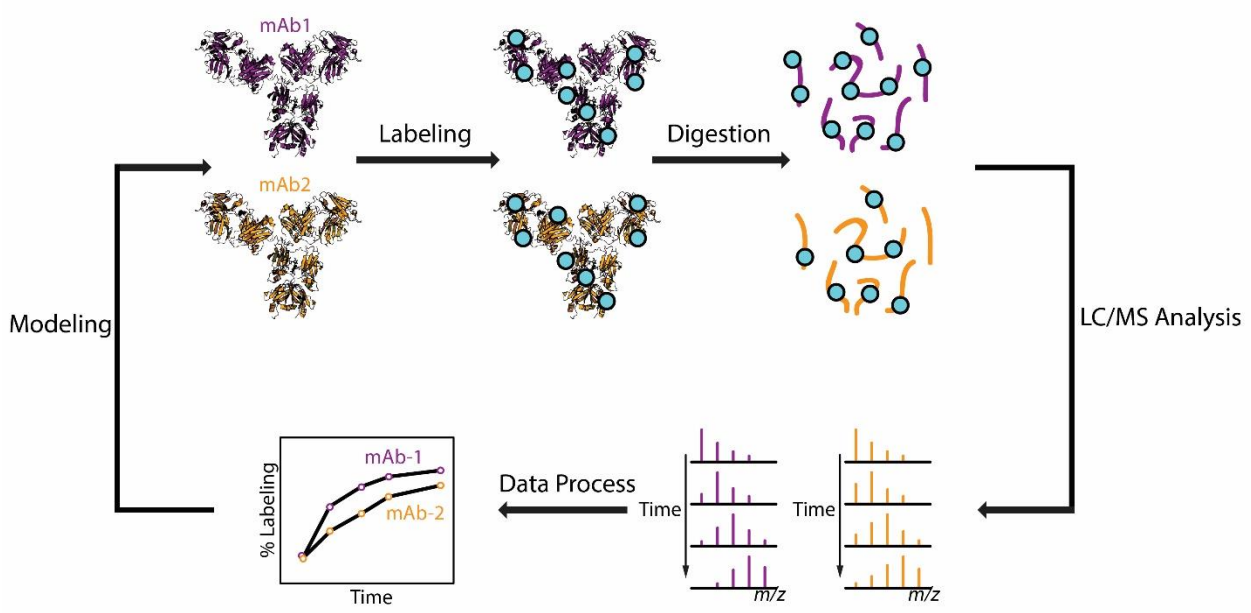

Figure 1-5. A generalized workflow for HDX-MS experiments. In the workflow shown, two antibodies are diluted in a deuterated buffer before quenching the labeling reactions. The labeled antibody is then subjected to proteolytic digestion, followed by MS analysis. The mass of each peptide is tracked at each time point and presented as kinetic plot. The data are processed to compare different mAb samples and search of variations in mAb structure and flexibility. If the mAb structure is known or if a structural model is available, molecular modeling can be performed in order to map conformational differences.

HDX-MS can be employed to assess mAb conformations and dynamics upon chemical modification, offering benefits to both therapeutic design and quality control protocols. For example, HDX-MS has been used to assess both the global and local conformational dynamics of an IgG1 antibody.[114] Changes in mAb conformation related to deglycosylation were examined using differential HDX-MS analysis, revealing two regions within IgG1 that possess altered protection and were rationalized as critical to FcγRIII receptor binding. The conformational effects of other PTMs, such as galactosylation, fucosylation, methionine oxidation, aspartic acid isomerization, and asparagine deamidation have also been investigated by HDX-MS.[115,116] In particular, HDX-MS has revealed that the complete galactosylation in IgG1, where all mAb glycoforms contain a terminal galactose, results in an increase in structural rigidity within the CH2 domains in a manner correlated with Fc receptor binding affinity. In contrast, this same study

demonstrated that the removal of fucose from the native population of antibody glycoforms did not lead to detectable changes in mAb conformation.

ADCs have also been broadly characterized by HDX-MS, where comparative data can uncover alterations in mAb dynamics perpetrated by both inter-chain disulfide reduction and the presence of conjugated drug molecules.[117] HDX-MS has also been used to assess antibody aggregates, aimed at understanding operative mechanism of mAb self-association.[50,118,119] For example, by HDX-MS, the Bevacizumab aggregates induced from multiple freeze/thaw cycles were observed to possess exchange profiles indistinguishable from native mAbs, whereas a similar analysis of thermally-induced aggregates revealed large changes in exchange behavior within mAb CDR regions.[118] Distinct mechanisms for the above stress-induced aggregation events can be extracted directly from the collected data, further highlighting the capabilities of comparative HDX-MS analysis. More recently, the combination of HDX-MS and a spatial aggregation propensity (SAP) algorithm allows identification of self-association hotspots in a mAb CDR region, underlining the potential of HDX-MS analysis to direct engineering of therapeutic antibodies in discovery and early development stage.[119] Furthermore, newly developed HDX-MS strategies along with the traditional methods have been shown to provide useful insights into the formulation development of mAbs.[120–122]

1.3.3 IM-MS Simultaneously Assessing the Size, Shape and Stability of Intact Antibodies

While IM is just beginning to be used to analyze mAb structure and stability, a number of reports showcased the ability of IM-MS to separate structural isoforms of antibody-based therapeutics. For example, early results in this area illustrated that IM can rapidly differentiate IgG2 disulfide-bonding structure based isoforms.[123] IM-MS data has also shown that intact mAbs are more

conformationally diverse than proteins or protein complexes of comparable sizes, as represented by the peak widths achieved during IM separation.[124] This work, as well as a later report combining CCS data from both DT, TWIM devices with molecular dynamics simulations strongly indicates that mAb ions undergo significant compaction in the gas phase, centering on the hinge region of the mAb structure.[125] In recent work, a combination of IM-MS and HDX-MS was used to probe the global and local dynamics of a series of IgG1 Fc variants.[126] While IM data were nearly identical for lower charge states of three IgG1 Fc variants, significant differences were observed in the IM data acquired for higher charge states. Overall, the IM-MS data indicated that the IgG1 Fc mutants were more susceptible to gas-phase unfolding when compared to wild type mAbs, consistent with their stabilities in solution. IM-MS data for intact therapeutic antibodies have also been used to rapidly assess the similarity of innovator mAbs and their biosimilars.[127]

In general, antibody isoforms that exhibit CCS differences of greater than 3% can be routinely resolved by IM separation.[85,93,128,129] In many cases, however, local conformational changes caused by PTMs or mutations can be too subtle to be captured by IM separation alone. In such cases, CIU can be used to rapidly resolve such conformational states through differences in their unfolding patterns and stabilities in the gas phase. CIU data is frequently displayed as a 'fingerprint', where the IM drift times or CCS values are plotted against the collision voltages used to heat ions and generate protein unfolding. (Figure. 1-6) Such experiments have been used for a broad array of applications, and the general utility of CIU in the context of small molecule drug discovery and development has been previously reviewed.[130–135] Relatively recently, CIU data has been shown to quantitatively discriminate between IgG subtypes that differ only in terms of their disulfide

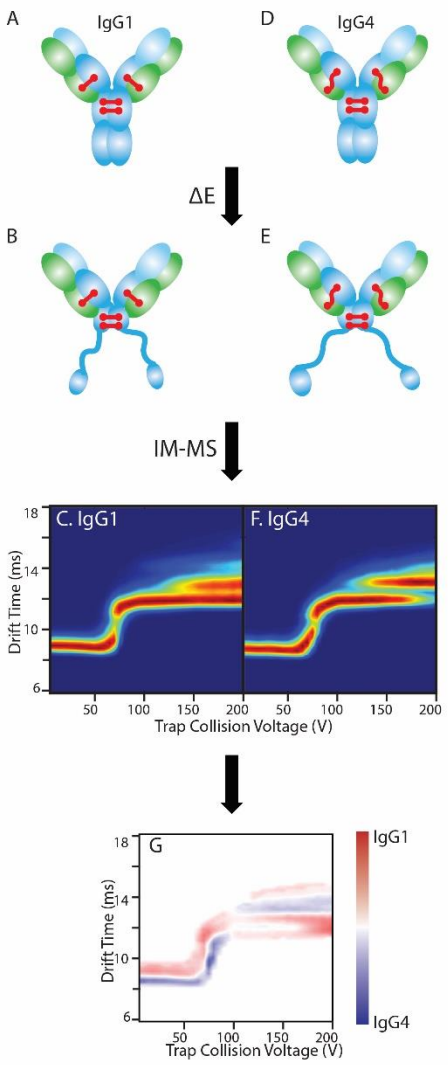

Figure 1-6. An example of collision-induced unfolding (CIU) analysis for IgG isoforms. Intact IgG1 (A) and IgG4 (D) are collisionally heated and undergo unfolding (B, E) in the gas phase prior to IM measurement. The IM data are then extracted in order to generate a plot of IM drift time against collision voltage projected as a contour plot (C, F). Once complied, this CIU fingerprint data are compared using custom software in order to detect differences in mAb (G). Figure C and F are adapted with permission. (DOI: 10.1021/acs.analchem.5b03291. Copyright @2015 American Chemical Society).

bonding.[136] For example, IgG1 and IgG4 possess the same number of inter-chain disulfide bonds, and only differ in the disulfide connectivity pattern between their heavy and light chains. In both cases, three main features were observed during CIU. However, detailed comparisons enabled by custom software[137] revealed clear differences within the CIU datasets. Continuing work in this area has seen CIU used to differentiate innovator and biosimilar preparations of infliximab, in which minor differences in mAb glycosylation and glycation across multiple sample lots produced

measurable shifts in mAb unfolding.[138] More recently, the combination of native IM-MS and CIU distinguished complexes formed between a single antigen and various antibodies binding to different epitopes.[139]

In addition to coupling with native MS for intact protein analysis, IM-MS has also been used extensively to separate and analyze complex peptide carbohydrate mixtures. The potential of IM-MS to distinguish lot-to-lot variability within mAb N-glycosylation profiles was recently reported.[140] Although such techniques have not been applied to therapeutic proteins yet, the utility of IM-MS for in-depth structural analysis of carbohydrate and glycoconjugate has been illustrated generally, illuminating the promising future for the characterization of therapeutic antibodies provided by such workflows.[141–143]

1.4 Dissertation Overview

This dissertation represents my work focused on the development of IM-MS and collision induced unfolding approaches for the characterization of intact antibodies and antibody related therapeutics. In Chapter 2, a CIU protocol is developed to rapidly differentiate antibody isoforms containing different disulfide bonding patterns and general levels of glycosylation. The CIU method is validated by control experiments and systematic statistical evaluations of reproducibility. This work has been published as **Yuwei Tian, Linjie Han, Adam C. Buckner and Brandon T. Ruotolo, *Analytical Chemistry,* 2015, 87(22), 11509–11515**. Chapter 3 discusses the use of such gas-phase unfolding approaches to differentiate subtly-different glycoforms within both intact antibody monomers and antibody Fc fragments, using minimal sample preparation and purification. This work has been published as **Yuwei Tian and Brandon T. Ruotolo, *International Journal of Mass Spectrometry,* 2018, 425, 1–9.** Following the method development, I further applied the

IM-MS and CIU techniques for characterization of therapeutic mAbs through collaborative projects. In Chapter 4, I discuss the application of native IM-MS and CIU analysis to analyze antibody drug conjugates. This work is done in collaboration with researchers at Amgen and is intended for submission as a peer-reviewed publication. In Chapter 5, I highlight my contribution to the comparability studies of the innovator and biosimilar infliximab, in which an integrated MS workflow is developed in collaboration with the Anna Schwendeman Group. This Chapter includes data from two peer-reviewed papers: **1) Karthik Pisupati, Yuwei Tian, Solomon Okbazghi, Alexander Benet, Rose Ackermann, Michael Ford, Sergei Saveliev, Christopher M. Hosfield, Marjeta Urh, Eric Carlson, Christopher Becker, Thomas J. Tolbert, Steven P. Schwendeman, Brandon T. Ruotolo and Anna Schwendeman, *Anal. Chem.*, 2017, 89, 4838–4846, 2) Karthik Pisupati, Alexander Benet, Yuwei Tian, Solomon Okbazghi, Jukyung Kang, Michael Ford, Sergei Saveliev, K. Ilker Sen, Eric Carlson, Thomas J. Tolbert, Brandon T. Ruotolo, Steven P. Schwendeman and Anna Schwendeman, *MAbs*, 2017, 9, 1197–1209.** Chapter 6 represents the work I performed in collaboration with Eli Lilly and Company during a 6-month internship. A novel HDX-MS strategy has been developed for conformational analysis of mAb in high concentration formulations. This chapter is intended for submission as a peer-reviewed publication. In Chapter 7, I conclude by summarizing my research results and discussing the future direction for this dissertation work.

1.5 References

(1) Walsh, G. *Nat. Biotechnol.* **2014**, *32* (10), 992–1000.
(2) Reichert, J. M. *MAbs* **2012**, *4* (3), 413–415.
(3) Ecker, D. M.; Jones, S. D.; Levine, H. L. *MAbs* **2015**, *7* (1), 9–14.
(4) Scott, A. M.; Wolchok, J. D.; Old, L. J. *Nat. Rev.* **2012**, *12* (4), 278–287.
(5) Chari, R. V. J.; Miller, M. L.; Widdison, W. C. *Angew. Chem. Int. Ed. Engl.* **2014**, *53* (15), 3796–3827.
(6) Reichert, J. M. *MAbs* **2017**, *9* (2), 167–181.
(7) Schroeder, H. W.; Cavacini, L.; Cavacini, L. *J. Allergy Clin. Immunol.* **2010**, *125* (2 Suppl

2), S41-52.
(8) Brekke, O. H.; Sandlie, I. *Nat. Rev. Drug Discov.* **2003**, *2* (1), 52–62.
(9) Wang, W.; Singh, S.; Zeng, D. L.; King, K.; Nema, S. *J. Pharm. Sci.* **2007**, *96* (1), 1–26.
(10) Jefferis, R. *Biotechnol. Prog.* **2005**, *21*, 11–16.
(11) Jefferis, R. *Nat. Rev. Drug Discov.* **2009**, *8* (3), 226–234.
(12) Hoogenboom, H. R. *Nat. Biotechnol.* **2005**, *23* (9), 1105–1116.
(13) Roque, a C. a; Lowe, C. R.; Taipa, M. A. *Biotechnol. Prog.* **2004**, *20* (3), 639–654.
(14) Walsh, G.; Jefferis, R. *Nat. Biotechnol.* **2006**, *24* (10), 1241–1252.
(15) Hansel, T. T.; Kropshofer, H.; Singer, T.; Mitchell, J. a; George, A. J. T. *Nat Rev Drug Discov* **2010**, *9* (4), 325–338.
(16) Carter, P. J.; Senter, P. D. *Cancer J.* **2013**, *14* (3), 154–169.
(17) Beck, A.; Goetsch, L.; Dumontet, C.; Corvaïa, N. *Nat. Rev. Drug Discov.* **2017**, *10* (5), 345–352.
(18) Beck, A.; Wurch, T.; Bailly, C.; Corvaia, N. *Nat. Rev. Immunol.* **2010**, *10* (5), 345–352.
(19) Kontermann, R. E.; Brinkmann, U. *Drug Discov. Today* **2015**, *20* (7), 838–847.
(20) Rup, B.; Krinos-Fiorotti, C.; Gorovits, B.; Neubert, H. *Biophys. Methods Biother. Discov. Dev. Appl.* **2014**, 207–242.
(21) Fekete, S.; Guillarme, D.; Sandra, P.; Sandra, K. *Anal. Chem.* **2015**, acs.analchem.5b04561.
(22) Sandra, K.; Vandenheede, I.; Sandra, P. *J. Chromatogr. A* **2014**, *1335*, 81–103.
(23) Shukla, A. a; Yigzaw, Y. *Modes of Preparative Chromatography*; 2007.
(24) Harris, R. J.; Kabakoff, B.; Macchi, F. D.; Shen, F. J.; Kwong, M.; Andya, J. D.; Shire, S. J.; Bjork, N.; Totpal, K.; Chen, A. B. *J. Chromatogr. B Biomed. Sci. Appl.* **2001**, *752* (2), 233–245.
(25) Khawli, L. A.; Goswami, S.; Hutchinson, R.; Kwong, Z. W.; Yang, J.; Wang, X.; Yao, Z.; Sreedhara, A.; Cano, T.; Tesar, D.; Nijem, I.; Allison, D. E.; Wong, P. Y.; Kao, Y. H.; Quan, C.; Joshi, A.; Harris, R. J.; Motchnik, P. *MAbs* **2010**, *2* (6), 613–624.
(26) Wen, J.; Arakawa, T.; Philo, J. S. *Anal. Biochem.* **1996**, *240*, 155–166.
(27) Lazar, A. C.; Wang, L.; Blättler, W. a; Amphlett, G.; Lambert, J. M.; Zhang, W. *Rapid Commun. Mass Spectrom.* **2005**, *19* (13), 1806–1814.
(28) Berkowitz, S. A.; Houde, D. J. *Size-Exclusion Chromatograph (SEC) in Biopharmaceutical Process Development*; 2014.
(29) Dorsey, J. G.; Dill, K. A. *Chem. Rev.* **1989**, *89* (2), 331–346.
(30) Queiroz, J. A.; Tomaz, C. T.; Cabral, J. M. S. *J. Biotechnol.* **2001**, *87* (2), 143–159.
(31) Wakankar, A.; Chen, Y.; Gokarn, Y.; Jacobson, F. S. *MAbs* **2011**, *3* (2), 161–172.
(32) Hull, A. W. *J. Am. Chem. Soc.* **1919**, *41* (8), 1168–1175.
(33) Rabi, I. I.; Zacharias, J. R.; Millman, S.; Kusch, P. *Phys. Rev.* **1938**, *53* (4), 318–318.
(34) Ramsland, P. A.; Farrugia, W. *J. Mol. Recognit.* **2002**, *15* (5), 248–259.
(35) Harris, L. J.; Skaletsky, E.; McPherson, A. *J. Mol. Biol.* **1998**, *275* (5), 861–872.
(36) Lisa J. Harris, §; Steven B. Larson, §; Karl W. Hasel, ‖ and; Alexander McPherson*, §. **1997**.
(37) Saphire, E. O.; Parren, P. W.; Pantophlet, R.; Zwick, M. B.; Morris, G. M.; Rudd, P. M.; Dwek, R. A.; Stanfield, R. L.; Burton, D. R.; Wilson, I. A. *Science* **2001**, *293* (5532), 1155–1159.
(38) Scapin, G.; Yang, X.; Prosise, W. W.; McCoy, M.; Reichert, P.; Johnston, J. M.; Kashi, R. S.; Strickland, C. *Nat. Struct. Mol. Biol.* **2015**, *22* (12), 953–958.

(39) Cavalli, A.; Salvatella, X.; Dobson, C. M.; Vendruscolo, M. *Proc. Natl. Acad. Sci. U. S. A.* **2007**, *104* (23), 9615–9620.
(40) CAVANAGH, J.; FAIRBROTHER, W. J.; PALMER, A. G.; RANCE, M.; SKELTON, N. J. In *Protein NMR Spectroscopy*; Elsevier, 2007; pp 781–817.
(41) Gokarn, Y.; Agarwal, S.; Arthur, K.; Bepperling, A.; Day, E. S.; Filoti, D.; Greene, D. G.; Hayes, D.; Kroe-Barrett, R.; Laue, T.; Lin, J.; McGarry, B.; Razinkov, V.; Singh, S.; Taing, R.; Venkataramani, S.; Weiss, W.; Yang, D.; Zarraga, I. E. In *State-of-the-Art and Emerging Technologies for Therapeutic Monoclonal Antibody Characterization Volume 2. Biopharmaceutical Characterization: The NISTmAb Case Study*; ACS Symposium Series; American Chemical Society, 2015; Vol. 1201, pp 285-327 SE – 6.
(42) Razinkov, V. I.; Treuheit, M. J.; Becker, G. W. *Curr. Drug Discov. Technol.* **2013**, *10* (1), 59–70.
(43) Pawlowski, J. W.; Bajardi-Taccioli, A.; Houde, D.; Feschenko, M.; Carlage, T.; Kaltashov, I. A. *J. Pharm. Biomed. Anal.* **2018**, *151*, 133–144.
(44) Schellman, J. A. *Chem. Rev.* **1975**, *75* (3), 323–331.
(45) Provencher, S. W.; Gloeckner, J. *Biochemistry* **1981**, *20* (1), 33–37.
(46) Liu, D.; Ren, D.; Huang, H.; Dankberg, J.; Rosenfeld, R.; Cocco, M. J.; Li, L.; Brems, D. N.; Remmele, R. L. *Biochemistry* **2008**, *47* (18), 5088–5100.
(47) Kelly, S. M.; Jess, T. J.; Price, N. C. **2005**.
(48) Kelly, S. M.; Price, N. C. *Curr. Protein Pept. Sci.* **2000**, *1*, 349–384.
(49) Johnson, C. M. *Arch. Biochem. Biophys.* **2013**, *531* (1–2), 100–109.
(50) Iacob, R. E.; Bou-Assaf, G. M.; Makowski, L.; Engen, J. R.; Berkowitz, S. A.; Houde, D. *J. Pharm. Sci.* **2013**, *102* (12), 4315–4329.
(51) Ben-Nissan, G.; Sharon, M. *Curr. Opin. Chem. Biol.* **2018**, *42*, 25–33.
(52) Engen, J. R.; Wales, T. E. *Annu. Rev. Anal. Chem.* **2015**, *8* (1), 127–148.
(53) Konermann, L.; Pan, J.; Liu, Y.-H. *Chem. Soc. Rev.* **2011**, *40* (3), 1224–1234.
(54) Sinz, A. *Mass Spectrom. Rev.* **2006**, *25* (4), 663–682.
(55) Hambly, D. M.; Gross, M. L. *J. Am. Soc. Mass Spectrom.* **2005**, *16* (12), 2057–2063.
(56) Konermann, L.; Stocks, B. B.; Pan, Y.; Tong, X. *Mass Spectrom. Rev.* **2010**, *29* (4), 651–667.
(57) Hill, H. H.; Siems, W. F.; St. Louis, R. H. *Anal. Chem.* **1990**, *62* (23), 1201A–1209A.
(58) St. Louis, R. H.; Hill, H. H.; Eiceman, G. A. *Crit. Rev. Anal. Chem.* **1990**, *21* (5), 321–355.
(59) Lanucara, F.; Holman, S. W.; Gray, C. J.; Eyers, C. E. *Nat. Chem.* **2014**, *6* (4), 281–294.
(60) Terral, G.; Beck, A.; Cianf??rani, S. *J. Chromatogr. B Anal. Technol. Biomed. Life Sci.* **2016**, *1032*, 79–90.
(61) Karas, M.; Bachmann, D.; Bahr, U.; Hillenkamp, F. *Int. J. Mass Spectrom. Ion Process.* **1987**, *78*, 53–68.
(62) Fenn, J. B.; Mann, M.; Meng, C. K.; Wong, S. F.; Whitehouse, C. M. *Science* **1989**, *246* (4926), 64–71.
(63) Loo, J. a. *Mass Spectrom. Rev.* **1997**, *16* (1), 1–23.
(64) Loo, J. a. *Int. J. Mass Spectrom.* **2000**, *200* (1–3), 175–186.
(65) Taylor, G. *Proc. R. Soc. A Math. Phys. Eng. Sci.* **1964**, *280* (1382), 383–397.
(66) Rayleigh, Lord. *London, Edinburgh, Dublin Philos. Mag. J. Sci.* **1882**, *14* (87), 184–186.
(67) Heck, A. J. R. *Nat. Methods* **2008**, *5* (11), 927–933.
(68) Kebarle, P.; Verkerk, U. H. *Mass Spectrom. Rev.* **2009**, *28* (6), 898–917.

(69) Wilm, M.; Mann, M. *Anal. Chem.* **1996**, *68* (1), 1–8.
(70) El-Faramawy, A.; Siu, K. W. M.; Thomson, B. a. *J. Am. Soc. Mass Spectrom.* **2005**, *16* (10), 1702–1707.
(71) Iribarne, J. V.; Thomson, B. A. *J. Chem. Phys.* **1976**, *64* (6), 2287.
(72) Thomson, B. A.; Iribarne, J. V. *J. Chem. Phys.* **1979**, *71* (11), 4451.
(73) Dole, M.; Mack, L. L.; Hines, R. L.; Mobley, R. C.; Ferguson, L. D.; Alice, M. B. *J. Chem. Phys.* **1968**, *49* (5), 2240–2249.
(74) Chernushevich, I. V.; Loboda, A. V.; Thomson, B. A. *J. Mass Spectrom.* **2001**, *36* (8), 849–865.
(75) Mamyrin, B. A.; Karataev, V. I.; Shmikk, D. V; Zagulin, V. A. .
(76) Dawson, J. H. J.; Guilhaus, M. *Rapid Commun. Mass Spectrom.* **1989**, *3* (5), 155–159.
(77) Radionova, A.; Filippov, I.; Derrick, P. J. *Mass Spectrom. Rev.* **2016**, *35* (6), 738–757.
(78) March, R. E. **2009**.
(79) Douglas, D. J. **2009**.
(80) Tahallah, N.; Pinkse, M.; Maier, C. S.; Heck, A. J. R. *Rapid Commun. Mass Spectrom.* **2001**, *15* (8), 596–601.
(81) Van Den Heuvel, R. H. H.; Van Duijn, E.; Mazon, H.; Synowsky, S. A.; Lorenzen, K.; Versluis, C.; Brouns, S. J. J.; Langridge, D.; Van Der Oost, J.; Hoyes, J.; Heck, A. J. R. *Anal. Chem.* **2006**, *78* (21), 7473–7483.
(82) Chernushevich, I. V; Thomson, B. a. **2004**, *76* (February), 1754–1760.
(83) Mason, E. A.; McDaniel, E. W. *Transport Properties of Ions in Gases*; Wiley-VCH Verlag GmbH & Co. KGaA: Weinheim, FRG, 1988.
(84) Kanu, A. B.; Dwivedi, P.; Tam, M.; Matz, L.; Hill, H. H. Ion mobility-mass spectrometry. *Journal of Mass Spectrometry*, 2008, *43*, 1–22.
(85) Bush, M. F.; Hall, Z.; Giles, K.; Hoyes, J.; Robinson, C. V.; Ruotolo, B. T. *Anal. Chem.* **2010**, *82* (22), 9557–9565.
(86) Shvartsburg, A. A.; Jarrold, M. F. *Chem. Phys. Lett.* **1996**, *261* (October), 86–91.
(87) Mesleh, M. F.; Hunter, J. M.; Shvartsburg, A. A.; Schatz, G. C.; Jarrold, M. F. *J. Phys. Chem.* **1996**, *100* (40), 16082–16086.
(88) Benesch, J. L. P.; Ruotolo, B. T. *Curr. Opin. Struct. Biol.* **2011**, *21* (5), 641–649.
(89) Wyttenbach, T.; Bowers, M. *Int J Mass Spectrom* **2001**, *212* (1–3), 13–23.
(90) Harvey, S. R.; MacPhee, C. E.; Barran, P. E. *Methods* **2011**, *54* (4), 454–461.
(91) Pringle, S. D.; Giles, K.; Wildgoose, J. L.; Williams, J. P.; Slade, S. E.; Thalassinos, K.; Bateman, R. H.; Bowers, M. T.; Scrivens, J. H. *Int. J. Mass Spectrom.* **2007**, *261* (1), 1–12.
(92) Giles, K.; Williams, J. P.; Campuzano, I. *Rapid Commun. Mass Spectrom.* **2011**, *25* (11), 1559–1566.
(93) Zhong, Y.; Hyung, S.-J.; Ruotolo, B. T. *Analyst* **2011**, *136* (17), 3534–3541.
(94) Giles, K.; Pringle, S. D.; Worthington, K. R.; Little, D.; Wildgoose, J. L.; Bateman, R. H. *RAPID Commun. MASS Spectrom. Rapid Commun. Mass Spectrom* **2004**, *18*, 2401–2414.
(95) Shvartsburg, a a; Smith, R. D. *Anal. Chem.* **2008**, *80* (24), 9689–9699.
(96) Bush, M. F.; Hall, Z.; Giles, K.; Hoyes, J. 1–9.
(97) Shelimov, K. B.; Clemmer, D. E.; Hudgins, R. R.; Jarrold, M. F. *J. Am. Chem. Soc.* **1997**, *119* (9), 2240–2248.
(98) Shelimov, K. B.; Jarrold, M. F. *J. Am. Chem. Soc.* **1997**, *119* (13), 2987–2994.
(99) Hyung, S.-J.; Robinson, C. V; Ruotolo, B. T. *Chem. Biol.* **2009**, *16* (4), 382–390.

(100) Han, L.; Hyung, S. J.; Mayers, J. J. S.; Ruotolo, B. T. *J. Am. Chem. Soc.* **2011**, *133* (29), 11358–11367.
(101) Han, L.; Hyung, S.-J.; Ruotolo, B. T. *Angew. Chemie Int. Ed.* **2012**, *51* (23), 5692–5695.
(102) Rabuck, J. N.; Hyung, S.-J.; Ko, K. S.; Fox, C. C.; Soellner, M. B.; Ruotolo, B. T. *Anal. Chem.* **2013**, *85* (15), 6995–7002.
(103) Niu, S.; Ruotolo, B. T. **2015**.
(104) Laganowsky, A.; Reading, E.; Allison, T. M.; Ulmschneider, M. B.; Degiacomi, M. T.; Baldwin, A. J.; Robinson, C. V. *Nature* **2014**, *510* (7503), 172–175.
(105) Zhong, Y.; Han, L.; Ruotolo, B. T. *Angew. Chemie* **2014**.
(106) Eschweiler, J. D.; Martini, R. M.; Ruotolo, B. T. *J. Am. Chem. Soc.* **2016**, jacs.6b11678.
(107) Eschweiler, J. D.; Rabuck-Gibbons, J. N.; Tian, Y.; Ruotolo, B. T. *Anal. Chem.* **2015**, *87* (22), 11516–11522.
(108) Kükrer, B.; Filipe, V.; Van Duijn, E.; Kasper, P. T.; Vreeken, R. J.; Heck, A. J. R.; Jiskoot, W. *Pharm. Res.* **2010**, *27* (10), 2197–2204.
(109) Rosati, S.; Rose, R. J.; Thompson, N. J.; Van Duijn, E.; Damoc, E.; Denisov, E.; Makarov, A.; Heck, A. J. R. *Angew. Chemie - Int. Ed.* **2012**, *51* (52), 12992–12996.
(110) Thompson, N. J.; Rosati, S.; Heck, A. J. R. *Methods* **2014**, *65* (1), 11–17.
(111) Tito, M. a; Miller, J.; Walker, N.; Griffin, K. F.; Williamson, E. D.; Despeyroux-Hill, D.; Titball, R. W.; Robinson, C. V. *Biophys. J.* **2001**, *81* (6), 3503–3509.
(112) Rosati, S.; Thompson, N. J.; Barendregt, A.; Hendriks, L. J. A.; Bakker, A. B. H.; De Kruif, J.; Throsby, M.; Van Duijn, E.; Heck, A. J. R. *Anal. Chem.* **2012**, *84* (16), 7227–7232.
(113) Thompson, N. J.; Hendriks, L. J. a; De Kruif, J.; Throsby, M.; Heck, A. J. R. *MAbs* **2014**, *6* (1), 197–203.
(114) Atmanene, C.; Wagner-Rousset, E.; Malissard, M.; Chol, B.; Robert, A.; Corvaïa, N.; Dorsselaer, A. Van; Beck, A.; Sanglier-Cianférani, S.-. *Anal. Chem.* **2009**, *81* (15), 6364–6373.
(115) Dyachenko, A.; Wang, G.; Belov, M.; Makarov, A.; de Jong, R. N.; van den Bremer, E. T. J.; Parren, P. W. H. I.; Heck, A. J. R. *Anal. Chem.* **2015**, *87* (12), 6095–6102.
(116) Rose, R. J.; Labrijn, A. F.; Van Den Bremer, E. T. J.; Loverix, S.; Lasters, I.; Van Berkel, P. H. C.; Van De Winkel, J. G. J.; Schuurman, J.; Parren, P. W. H. I.; Heck, A. J. R. *Structure* **2011**, *19* (9), 1274–1282.
(117) Chen, J.; Yin, S.; Wu, Y.; Ouyang, J. *Anal. Chem.* **2013**, *85* (3), 1699–1704.
(118) Debaene, F.; Bœuf, A.; Wagner-Rousset, E.; Colas, O.; Ayoub, D.; Corvaïa, N.; Van Dorsselaer, A.; Beck, A.; Cianférani, S. *Anal. Chem.* **2014**, *86* (21), 10674–10683.
(119) Marcoux, J.; Champion, T.; Colas, O.; Wagner-Rousset, E.; Corvaïa, N.; Van Dorsselaer, A.; Beck, A.; Cianférani, S. *Protein Sci.* **2015**, *24* (8), 1210–1223.
(120) Campuzano, I. D. G.; Netirojjanakul, C.; Nshanian, M.; Lippens, J. L.; Kilgour, D. P. A.; Van Orden, S.; Loo, J. A. *Anal. Chem.* **2018**, *90* (1), 745–751.
(121) Katta, V.; Chait, B. T.; Carr, S. *Rapid Commun. Mass Spectrom.* **1991**, *5* (4), 214–217.
(122) Pirrone, G. F.; Iacob, R. E.; Engen, J. R. *Anal. Chem.* **2015**, *87* (1), 99–118.
(123) Wei, H.; Mo, J.; Tao, L.; Russell, R. J.; Tymiak, A. A.; Chen, G.; Iacob, R. E.; Engen, J. R. *Drug Discov. Today* **2014**, *19* (1), 95–102.
(124) Weis, D. D. *Hydrogen Exchange Mass Spectrometry of Proteins*; Weis, D. D., Ed.; John Wiley & Sons, Ltd: Chichester, UK, 2016.
(125) Houde, D.; Arndt, J.; Domeier, W.; Berkowitz, S.; Engen, J. R. *Anal. Chem.* **2009**, *81* (7),

2644–2651.
(126) Houde, D.; Peng, Y.; Berkowitz, S. a; Engen, J. R. *Mol. Cell. Proteomics* **2010**, *9* (8), 1716–1728.
(127) Zhang, A.; Hu, P.; MacGregor, P.; Xue, Y.; Fan, H.; Suchecki, P.; Olszewski, L.; Liu, A. *Anal. Chem.* **2014**, *86* (7), 3468–3475.
(128) Pan, L. Y.; Salas-Solano, O.; Valliere-Douglass, J. F. *Anal. Chem.* **2014**, *86* (5), 2657–2664.
(129) Zhang, A.; Singh, S. K.; Shirts, M. R.; Kumar, S.; Fernandez, E. J. *Pharm. Res.* **2012**, *29* (1), 236–250.
(130) Dobson, C. L.; Devine, P. W. A.; Phillips, J. J.; Higazi, D. R.; Lloyd, C.; Popovic, B.; Arnold, J.; Buchanan, A.; Lewis, A.; Goodman, J.; van der Walle, C. F.; Thornton, P.; Vinall, L.; Lowne, D.; Aagaard, A.; Olsson, L.-L.; Ridderstad Wollberg, A.; Welsh, F.; Karamanos, T. K.; Pashley, C. L.; Iadanza, M. G.; Ranson, N. A.; Ashcroft, A. E.; Kippen, A. D.; Vaughan, T. J.; Radford, S. E.; Lowe, D. C. *Sci. Rep.* **2016**, *6* (June), 38644.
(131) Arora, J.; Hickey, J. M.; Majumdar, R.; Esfandiary, R.; Bishop, S. M.; Samra, H. S.; Middaugh, C. R.; Weis, D. D.; Volkin, D. B. *MAbs* **2015**, *7* (3), 525–539.
(132) Houde, D.; Nazari, Z. E.; Bou-Assaf, G. M.; Weiskopf, A. S.; Rand, K. D. *J. Am. Soc. Mass Spectrom.* **2016**, *27* (4), 669–676.
(133) Arora, J.; Joshi, S. B.; Middaugh, C. R.; Weis, D. D.; Volkin, D. B. *J. Pharm. Sci.* **2017**, *106* (6), 1508–1518.
(134) Bagal, D.; Valliere-Douglass, J. F.; Balland, A.; Schnier, P. D. *Anal. Chem.* **2010**, *82* (16), 6751–6755.
(135) Pacholarz, K. J.; Porrini, M.; Garlish, R. a; Burnley, R. J.; Taylor, R. J.; Henry, A. J.; Barran, P. E. *Angew. Chem. Int. Ed. Engl.* **2014**, *53* (30), 7765–7769.
(136) Campuzano, I. D. G.; Larriba, C.; Bagal, D.; Schnier, P. D. In *ACS Symposium Series*; 2015; Vol. 1202, pp 75–112.
(137) Edgeworth, M. J.; Phillips, J. J.; Lowe, D. C.; Kippen, A. D.; Higazi, D. R.; Scrivens, J. H. *Angew. Chemie Int. Ed.* **2015**, *54* (50), 15156–15159.
(138) Beck, A.; Debaene, F.; Diemer, H.; Wagner-Rousset, E.; Colas, O.; Dorsselaer, A. Van; Cianférani, S. *J. Mass Spectrom.* **2015**, *50* (2), 285–297.
(139) Bush, M. F.; Campuzano, I. D. G.; Robinson, C. V. *Anal. Chem.* **2012**, *84* (16), 7124–7130.
(140) Salbo, R.; Bush, M. F.; Naver, H.; Campuzano, I.; Robinson, C. V.; Pettersson, I.; Jørgensen, T. J. D.; Haselmann, K. F. *Rapid Commun. Mass Spectrom.* **2012**, *26* (February), 1181–1193.
(141) Zhong, Y.; Han, L.; Ruotolo, B. T. *Angew. Chem. Int. Ed. Engl.* **2014**, *53* (35), 9209–9212.
(142) Niu, S.; Rabuck, J. N.; Ruotolo, B. T. *Curr. Opin. Chem. Biol.* **2013**, *17* (5), 809–817.
(143) Tian, Y.; Han, L.; Buckner, A. C.; Ruotolo, B. T. *Anal. Chem.* **2015**, *87* (22), 11509–11515.
(144) Pisupati, K.; Tian, Y.; Okbazghi, S.; Benet, A.; Ackermann, R.; Ford, M.; Saveliev, S.; Hosfield, C. M.; Urh, M.; Carlson, E.; Becker, C.; Tolbert, T. J.; Schwendeman, S. P.; Ruotolo, B. T.; Schwendeman, A. *Anal. Chem.* **2017**, *89* (9), 4838–4846.
(145) Huang, Y.; Salinas, N. D.; Chen, E.; Tolia, N. H.; Gross, M. L. *J. Am. Soc. Mass Spectrom.* **2017**, 24–27.

(146) Damen, C. W. N.; Chen, W.; Chakraborty, A. B.; van Oosterhout, M.; Mazzeo, J. R.; Gebler, J. C.; Schellens, J. H. M.; Rosing, H.; Beijnen, J. H. *J. Am. Soc. Mass Spectrom.* **2009**, *20* (11), 2021–2033.
(147) Huang, Y.; Gelb, A.; Dodds, E. *Curr. Metabolomics* **2014**, *1*, 291–305.
(148) Both, P.; Green, A. P.; Gray, C. J.; Šardzík, R.; Voglmeir, J.; Fontana, C.; Austeri, M.; Rejzek, M.; Richardson, D.; Field, R. A.; Widmalm, G.; Flitsch, S. L.; Eyers, C. E. *Nat Chem* **2014**, *6* (1), 65–74.
(149) Hofmann, J.; Hahm, H. S.; Seeberger, P. H.; Pagel, K. *Nature* **2015**, *526* (7572), 241–244.

Chapter 2. Collision Induced Unfolding of Intact Antibodies: Rapid Characterization of Disulfide Bonding Patterns, Glycosylation, and Structures

Yuwei Tian, Linjie Han, Adam C. Buckner and Brandon T. Ruotolo, *Analytical Chemistry*, 2015, 87(22), 11509–11515. (DOI: 10.1021/acs.analchem.5b03291)

Abstract

Monoclonal antibodies (mAbs) are among the fastest growing class of therapeutics due to their high specificity and low incidence of side effects. Unlike most drugs, mAbs are complex macromolecules (~150 kDa), leading to a host of quality control and characterization challenges inherent in their development. Recently, we introduced a new approach for the analysis of the intact proteins based on ion mobility-mass spectrometry (IM-MS). Our protocol involves the collision induced unfolding (CIU) of intact antibodies, where collisional heating in the gas-phase is used to generate unfolded anti-body forms, which are subsequently separated by IM, and then analyzed by MS. Collisional energy is added to the anti-body ions in a step-wise fashion, and 'fingerprint plots' are created that track the amount of unfolding undergone as a function of the energy imparted to the ions prior to IM separation. In this report, we have used these fingerprints to rapidly distinguish between antibody isoforms, possessing different numbers and/or patterns of disulfide bonding and general levels of glycosylation. In addition, we validate our CIU protocols through control experiments and systematic statistical evaluations of CIU reproducibility. We conclude by projecting the impact of our approach for antibody-related drug development and discovery applications.

2.1 Introduction

Biotherapeutics are macromolecular therapies manufactured or extracted from biological sources, typical based on proteins or nucleic acids having diverse compositions and mechanisms of action.[1] Therapeutic monoclonal antibodies (mAbs) comprise the largest class of such biotherapeutics, and carry significant pharmaceutical benefits.[2] For example, antibody-based biotherapeutics typically exhibit higher efficiency, specificity, fewer side effects when compared with similarly-targeted small molecules. These advantages have driven biotherapeutics to the forefront of the pharmaceutical industry, and made them the fastest growing class of current therapeutics.[2] The structural and compositional complexity of antibody-based therapeutics, while driving their pharmaceutical benefits, also provides new challenges for their discovery and development. Most large therapeutic proteins are not a single species, but are best characterized as a heterogeneous population of variants, produced through variable post-translational modifications and degradation products.[3] Specifically, these forms can include variations in disulfide linkages,[4,5] glycosylation,[6] oxidation,[7] and aggregation state.[8] If not controlled, this heterogeneity can alter protein function, decrease drug efficacy and potentially give rise to safety issues.[9] Thus, fully assessing the structural properties of therapeutic proteins is a critical, emergent analytical task in the development of new biotherapeutics.

To meet the analytical challenges described above, a battery of analytical methods have been developed for the detailed and rapid characterization of therapeutic antibodies,[10] including complementary chromatographic, spectroscopic, and spectrometric probes. Specifically, mass spectrometry (MS)-based workflows have been constructed for the detailed sequencing and characterization of chemical modifications of intact antibodies. A variety of tandem MS methods, utilizing electron-initiated fragmentation methods, combined with liquid chromatography (LC) are

capable of assessing the detailed composition and sequence of antibody variants and biosimilars using "bottom-up",[11] "middle-down",[12] and "top-down"[13] frameworks. In addition to questions of protein composition, MS can also characterize intact antibody structure, where chemical labeling approaches coupled to MS have been shown to be useful in the rapid assessment of intact antibody structure.[14] Ion mobility (IM) separations, which use weak electric fields to separate gas-phase protein ions according to their orientationally averaged collision cross section (CCS) and charge in an ion guide pressurized with inert neutrals,[15,16] has also been used to characterize intact antibodies and antibody–drug conjugates (ADCs), revealing drug-to-antibody ratios (DARs),[17] evidence of gas-phase compaction,[18] and CCS variations across isoforms[19] for intact antibodies. Although there are many reports of MS and IM-MS methods, many of these approaches fail to report on the details of antibody tertiary structure and modification level on the rapid (1000s of samples-per-day) time scale required by typical pharmaceutical development pipelines.[20,21]

In this report, we describe the development of collision induced unfolding (CIU) for the rapid analysis of antibody structure and chemical modifications. CIU technology uses collisional activation of selected protein ions in an ion trap prior to IM separation to elicit unfolding transitions in gas-phase proteins.[22,23] The resultant unfolded states produced by the CIU process have previously been linked to protein stability shifts upon anion or cation binding,[24,25] tertiary structure differences in kinase–inhibitor complexes,[26] membrane protein stabilization upon lipid binding,[27] and native-state protein domain structure.[28] Here, we provide the first evidence demonstrating that CIU can also be used to differentiate antibody isoforms that differ in terms of their disulfide bonding and glycosylation states. Furthermore, we thoroughly evaluate the reproducibility of the CIU method, and we find the technology to have a precision sufficient to detect even subtle changes in protein tertiary structure. Through the application of custom software

that quickly identifies highly differentiated regions within CIU data acquired for antibody isoforms,[29] the analysis of biotherapeutics can be done on a time scale sufficiently rapid for pharmaceutical screening. Finally, we use the data presented to discuss the future of CIU for biotherapeutic analysis in general.

2.2 Materials and Methods

Sample Preparation

IgG1κ, IgG2κ, IgG3κ, and IgG4κ from human myeloma were purchased from Sigma-Aldrich (St. Louis, MO). Antibody samples with a concentration of 1 mg/mL (~6.7 μM) were buffer exchanged into 100 mM ammonium acetate buffer using Micro Bio-Spin 30 columns (Bio-Rad, Hercules, CA) without further purification.

Antibody Deglycosylation

Intact mAb Mass Check Standard (product number: 186006552) was purchased from Waters (Milford, MA). The powdered sample was reconstituted into 100 mM ammonium acetate buffer to a stock concentration of 1 mg/500 μL (~13 μM). Glycerol-free PNGase F (500 000 units/mL) was purchased from New England Biolabs (Ipswich, MA). Deglycosylation was performed under non-denaturing conditions. Ten microliters of mAb stock solution was mixed with 2 μL of 10× Glycobuffer 2 (New England Biolabs, Ipswich, MA) and further diluted by adding 8 μL of H_2O. One microliter of PNGase F was then added to this buffered antibody solution, and the final mixture was then incubated at 37 °C for 30 min. After incubation, the mAb sample was desalted and exchanged into a 500 mM ammonium acetate buffer using a Micro Bio-Spin 30 column (Bio-Rad, Hercules, CA). Antibodies analyzed in Figures 2-1, 2-2, and 2-3 did not undergo this treatment.

Ion Mobility-Mass Spectrometry

Sample aliquots (~7 μL) were analyzed by IM-MS on a quadrupole-ion mobility-time-of-flight mass spectrometer (Q-IM-ToF MS) instrument (Synapt G2 HDMS, Waters, Milford, MA).[30,31] Antibody ions were generated using a nESI source in the positive mode. Capillary voltages of 1.5–1.7 kV were applied, and the sampling cone was operated at 60 V. The trap traveling-wave ion guide was pressurized to 3.4×10^{-2} mbar of argon gas. The traveling-wave ion mobility separator was operated at a pressure of ~2.5 mbar and employed a series of DC voltage waves (40 V wave height traveling at 600 m/s) to generate ion mobility separation. The ToF-MS was operated over the *m*/*z* range of 1000–10 000 at a pressure of 1.7×10^{-6} mbar.

Collision Induced Unfolding

Collision energy was added to the ions in the traveling-wave-based ion trap situated prior to the IM separator to perform antibody CIU. Tandem-MS (quadrupole selection) mode was used, in which antibody ions at *m*/*z* values corresponding to the 23^+ charge state were selected. The collision voltage was ramped from 5 to 200 V in 5 V increments to construct the fingerprint data shown in this report. IM data were recorded for MS-isolated ions at each collision voltage (Figure 2-1a), and the IM data for only those ions corresponding to the intact *m*/*z* originally isolated were compiled to created the CIU data shown.

Data Analysis

Mass spectra were calibrated externally using a solution of cesium iodide (100 mg/mL) and processed with Masslynx V4.1 software (Waters, Milford, MA). Exact molecular masses of intact mAb mass check standard and deglycosylated mAb samples were calculated by assigning the charge states based on the set that gives lowest standard deviation for a given average mass

assignment.[32,33]

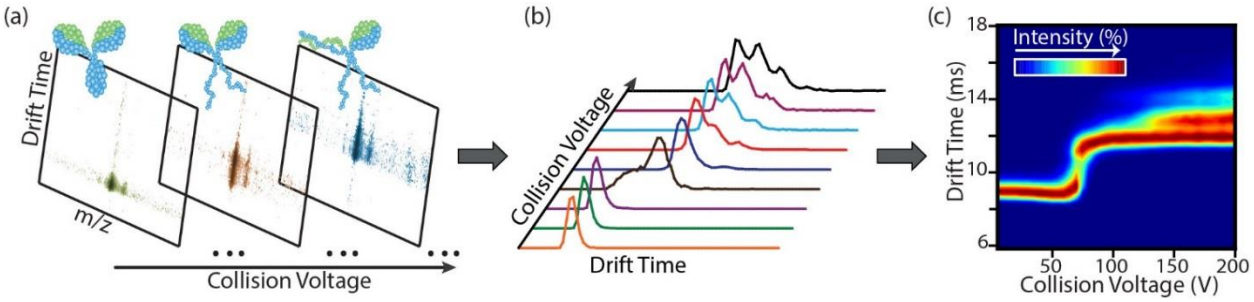

Figure 2-1. An illustration of the collision induced unfolding analysis workflow for intact antibodies. (a) Selected antibody ions are unfolded through collisional heating, resulting in increased drift times; (b) Drift time data for a single protein charge state is tracked at each collision energy; (c) A collision induced unfolding 'fingerprint' is projected as a contour plot, where intensities for the features observed are denoted by a color-coded axis. Once complied, fingerprint data are compared using custom software in order to detect differences.

Drift time data was extracted at each collision voltage in Drift Scope (Waters, Milford, MA) (Figure 2-1b). Extracted CIU data were analyzed using a home-built software package termed CIUSuite.[29] CIU "fingerprint" data were plotted as a 2D contour plot using CIUSuite_plot module (Figure 2-1c), in which ion intensities were normalized to a maximum value of 1 at each collision voltage and smoothed using a Savitzky−Golay filter. Statistical analysis of CIU data sets was conducted using the CIUSuite_stats function. Average CIU fingerprints and standard deviation plots were generated for multiple replicates. Comparison of two CIU fingerprints were accomplished using the CIUSuite_compare module, which allows matrix subtraction and visualization of the difference matrix. A root-mean-square deviation (RMSD) parameter was also generated using the CIUSuite_compare module, as defined in eq 2-1:

$$RMSD = \sqrt{\frac{\sum(A^x - A^y)^2}{m \times n}} \times 100\% \qquad \text{(eq 2-1)}$$

where A^x and A^y are both $m \times n$ CIU matrices.

2.3 Results and Discussion

Figure 2-1 illustrates our general CIU workflow, using data for IgG1κ as an example. IgG ions are generated by nESI under conditions that promote the preservation of native-like, compact ions.[34] As such, the proteins adopt a relatively narrow range of charge states ($19–27^+$) when compared with nESI data for denatured proteins.[35,36] IM-MS parameters were tuned to allow the transmission and separation of compact antibody ions. As observed previously, charge-state selection for CIU experiments dramatically influences the information content of the experiment.[22,26,28,37] For example, high-charge-state protein ions may undergo Coulombic unfolding transitions prior to collisional activation, whereas insufficient acceleration potential may be available to elicit CIU for lower-charge-state ions. For the CIU data presented here, charge states were selected on the basis of considerations of ion intensity, compact structure, and the resulting number of CIU transitions observed over the available voltage range. Using these criteria, we screened a range of charge states ($22^+–24^+$) and chose the 23^+ because of its superior intensity and CIU information content. Following quadrupole selection, these ions are activated in the ion trap region of our Q-IM-ToF instrument by increasing the acceleration potential experienced by ions upon entering the trap in a stepwise fashion. As this accelerating voltage is increased, antibody ions undergo CIU and populate unfolded states that exhibit extended IM drift times when compared to low-energy conditions (Figure 2-1a). The IM drift time data for intact 23^+ antibody ions is then extracted for each voltage step (Figure 2-1b) and then combined into a CIU fingerprint, where ion intensities are denoted by a color axis and the voltage required to collisionally heat protein ions and initiate unfolding can be readily tracked for each conformer family detected (Figure 2-1c). Using larger voltage intervals to construct CIU fingerprints results in lower resolution data that may miss important CIU transitions and states. As such, we optimized the

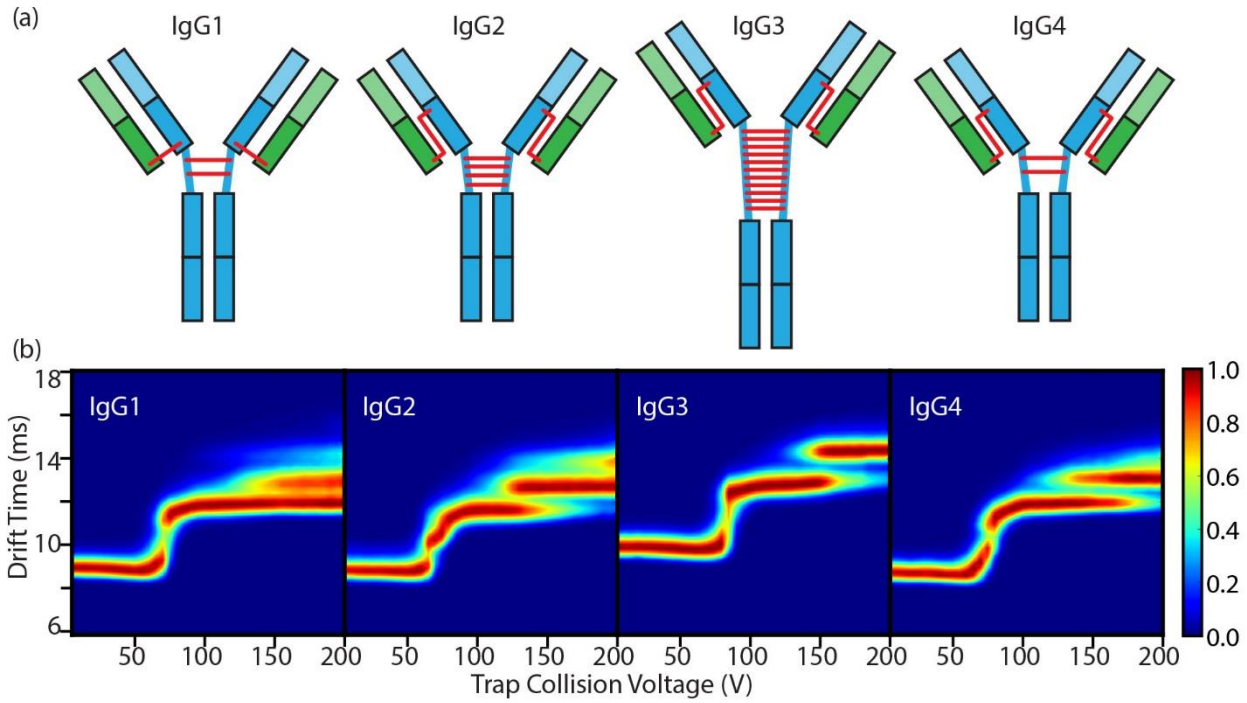

Figure 2-2. (a) Illustrations of IgG subtype structures. The key factors that differentiated these four subtypes related to the number and pattern of the disulfide bonds present within the structures (illustrated as red lines); (b) CIU fingerprints for IgG1κ, IgG2κ, IgG3κ and IgG4κ from human myeloma. Different unfodling patterns for these four antibody subtypes are observed, with the greatest differences correlated to the number of disulfide bonds present within each antibody analyzed, but minor differences can also be detected between IgG1κ and IgG4κ, which differ only with respect to the the pattern of disulfide bonds within their respective structures.

voltage interval used to construct the CIU data shown in this report (5 V increments) to yield plots of sufficiently high resolution and minimized acquisition times.

In order to characterize our CIU approach in the context of intact antibody analysis, we analyzed samples containing four human IgG subtypes purified from human myeloma—IgG1κ, IgG2κ, IgG3κ, and IgG4κ as model systems. Human IgG1κ, IgG2κ, and IgG4κ share more than 90% sequence identity and possess identical domain structures,[38] all having molecular masses of ~149 kDa. The main differences in human IgG subtypes are the numbers of interchain disulfide bonds and/or their patterns, with 4 interchain disulfide bonds in IgG1κ and IgG4κ, 6 in IgG2κ, and 13 in IgG3κ, as shown in Figure 2-2a. Because of their highly similar primary structures, it is challenging to distinguish these three IgG subtypes based on MS data for the intact antibodies alone. Equally, IgG1κ, IgG2κ, and IgG4κ are nominally iso-cross sectional under the IM

conditions used here, with only IgG3κ producing ground-state IM arrival time significantly different from the other three.[18] As such, it is difficult to detect the subtle variations in IgG subtypes through the analysis of intact mAb ions using MS or IM-MS techniques.

In the first instance, we analyzed CIU data acquired for IgG subtypes for evidence of differentiating fingerprints in the context of the total number of interchain disulfide bonds present in the antibody ions selected. As shown in Figure 2-2b, the 23^+ intact antibody ions for human IgG1κ, containing four interchain disulfide bonds, and IgG2κ, containing six interchain disulfide bonds, exhibit identical low energy IM migration times of ~8.9 ms, but possess significantly different CIU fingerprints. Three main CIU features are observed for IgG1κ, including the initial compact state and two additional unfolded states that are observed over the acceleration voltage range shown, ranging from 8.9 to 13 ms. An additional low-intensity fourth feature, having an IM drift time of ~14 ms, also appears at higher energies. In contrast, IgG2κ occupies five total states, four main conformational families which have centroid IM times and collision voltages different from those of IgG1κ. IgG3κ, on the other hand, exhibits a longer initial IM migration time (~9.8 ms) than the other intact mAb ions studied here, likely due to its more-constrained hinge region, possessed 13 disulfide bonds (more than a factor of 2 greater than IgG1κ and IgG2κ). In addition, IgG3κ possesses a CIU fingerprint that is dramatically different than the other antibodies in our data set, with only three principle IM features detected over the activation voltage range probed here. Taken together, and noting the high structure and sequence identity between the mAbs studied, the data presented in Figure 2-2 strongly supports the hypothesis that CIU is highly sensitive to the number of disulfide bonds present within a protein ion.

Having assessed the influence of the total number of interchain disulfide bonds on mAb CIU fingerprints, we moved to study IgG subtypes that differ only in terms of their disulfide bonding

patterns. Both IgG1κ and IgG4κ contain four interchain disulfide bonds; however, these bonds act to link different regions of the light and heavy chains within the intact mAbs (Figure 2-2a). A cursory comparison of the CIU data acquired for these two IgG subtypes reveals many similarities, in that both subtypes possess three main CIU features. However, a detailed analysis reveals clear CIU differences at both low (65–85 V) and high (180–200 V) collision voltages, with both the centroid IM drift times and collision voltages of the CIU features observed between IgG1 and IgG4 differing within these collision energy ranges. In addition, the transition between the lowest energy compact state and the first unfolded state possesses a markedly different shape for the two IgG subtypes. On the basis of the results in Figure 2-2, we can further conclude that the CIU approach is sensitive not only to the number of disulfide bonds within intact mAbs but also to the patterns that those bonds take within the protein ion.

In order to further validate the ability of our CIU approach to differentiate mAb samples, we acquired large numbers (n = 7 or higher) of replicate fingerprints and both assessed their reproducibility and quantified their discrimination power for the mAb subtypes discussed above. For example, Figure 2-3a shows a pixel-by-pixel standard deviation analysis of such an averaged CIU data set for IgG1κ, where individual data sets were collected on different days, using various nESI emitter tips, operated at capillary

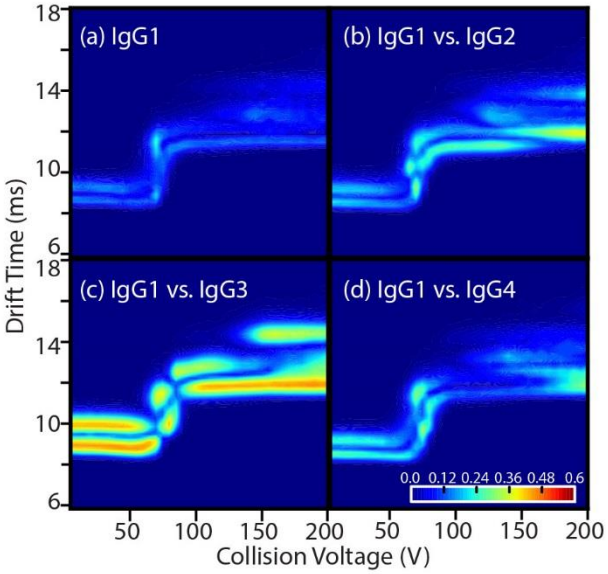

Figure 2-3. Quantifying the reproducibility and differentiating power for the CIU of mAbs. (a) Standard deviation plot for 7 IgG1κ replicates. In general, standard deviations are below 0.05 (or 5% relative signal intensity) above 100V. (b-d) Comparing IgG1κ with IgG2κ, IgG3κ, and IgG4κ. Clear differences in standard deviation are observed in both the low and high voltage regions, indicated by standard deviations of greater than 0.4 to .05, or 40-50% of the total signal intensity

voltages ranging from 1.5 kV to 1.8 kV. Small relative standard deviation values are observed in this analysis, peaking at ~25% for CIU data recorded at 70 V, but with most other relative standard deviation values well below 7%, especially at voltages larger than 100 V. Using eq 2-1, we computed fingerprint-level RMSD values of 5% for the IgG1κ shown in Figure 2-3a, further demonstrating the excellent reproducibility of CIU data. We then used the data shown in Figure 3a as a baseline to quantify our ability to differentiate IgG subtypes (Figure 2-3b–d). Although CIU data lower than 65 V exhibits appreciable noise, and therefore less discriminating power, CIU data recorded above 100 V reveals relative standard deviations between IgG subtypes that are between 4 and 5 times that recorded for the data shown in Figure 2-3a. Simple statistical analyses using this data (e.g., Kolmogorov–Smirnov) further reveal that all antibody subtypes can be differentiated at a confidence level greater than 99.95%, if the regions of greatest dissimilarity within the CIU fingerprints shown (e.g., trap collision voltage of 200 V) are used (see Figure I-4). As expected, the largest deviations are recorded upon comparing IgG3κ data with the IgG1κ baseline, whereas the smallest differences are observed for similar IgG4κ comparisons. Fingerprint-wide RMSD values that compare IgG1κ with IgG2κ, IgG3κ and IgG4κ are 12%, 28%, and 10% respectively, results that are between 2 and 5.6 times baseline values. Therefore, the data shown in Figure 2-3, and the analysis discussed above, strongly supports the ability of CIU to quantifiably and reproducibly differentiate mAbs based on both the number and pattern of interchain disulfide bonds present.

All of the analyses discussed above were carried out on fully glycosylated mAb samples, and in order to evaluate the sensitivity of CIU to differences in the levels of mAb glycosylation, we undertook a series of experiments aimed at performing CIU analysis for a range of deglycosylated mAbs. Glycosylation is among the most important post-translational modifications within

therapeutic antibodies, as it impacts antibody effector function, immunogenicity, plasmatic clearance, and resistance toward proteases.[39] The N-linked gycosylations are usually complex biantennary oligosaccharides containing 0–2 nonreducing galactoses (Gal) with or without fucose (Fuc) attached to the reducing end of N-acetylglucosamine (GlcNAc). The N-glycan is typically attached to the residue Asn297 in the Fc region of the antibody structure, with some instances of glycosylation events that occur in the Fab region.[6] Recently, high-resolution MS analysis of intact antibodies has been demonstrated as a means differentiating and quantifying antibody glycoforms; however, higher-order structural changes caused by antibody glycosylation and deglycosylation have not been intensively investigated.

We began these experiments by using a well-defined recombinant IgG1 standard, possessing a completely defined amino acid sequence, and having a known disulfide bonding pattern (7 total) and one N-linked glycosylation of known structure on each heavy chain. Averaged sequence molecular mass of this IgG1 standard is 145 329.7 Da, and increases to 148 382.5 Da for the completely glycosylated form. IM-MS for these IgG1 standards, prepared both under control conditions (500 mM ammonium acetate buffer) and following PNGase F deglycosylation, are shown in Figure 2-4a,b. A single measured intact average mass of 148,635 ± 29 Da is recorded for control samples, which is close to the expected value for the fully glycoslyated form. We attribute the relatively small amount of excess mass recorded relative to the expected mass of the fully glycosylated form of the antibody standard to the incomplete desolvation of the antibody ions in our experiments, commonly observed in native MS data.[33] Following PNGase F treatment, two additional signals are observed having molecular masses of 147 140 ± 26 Da and 145 555 ± 24 Da, and representing mass differences of ~1.5 kDa and ~3.1 kDa respectively relative to control data. Because antibodies have symmetric structures, we attribute these two new signals to stepwise

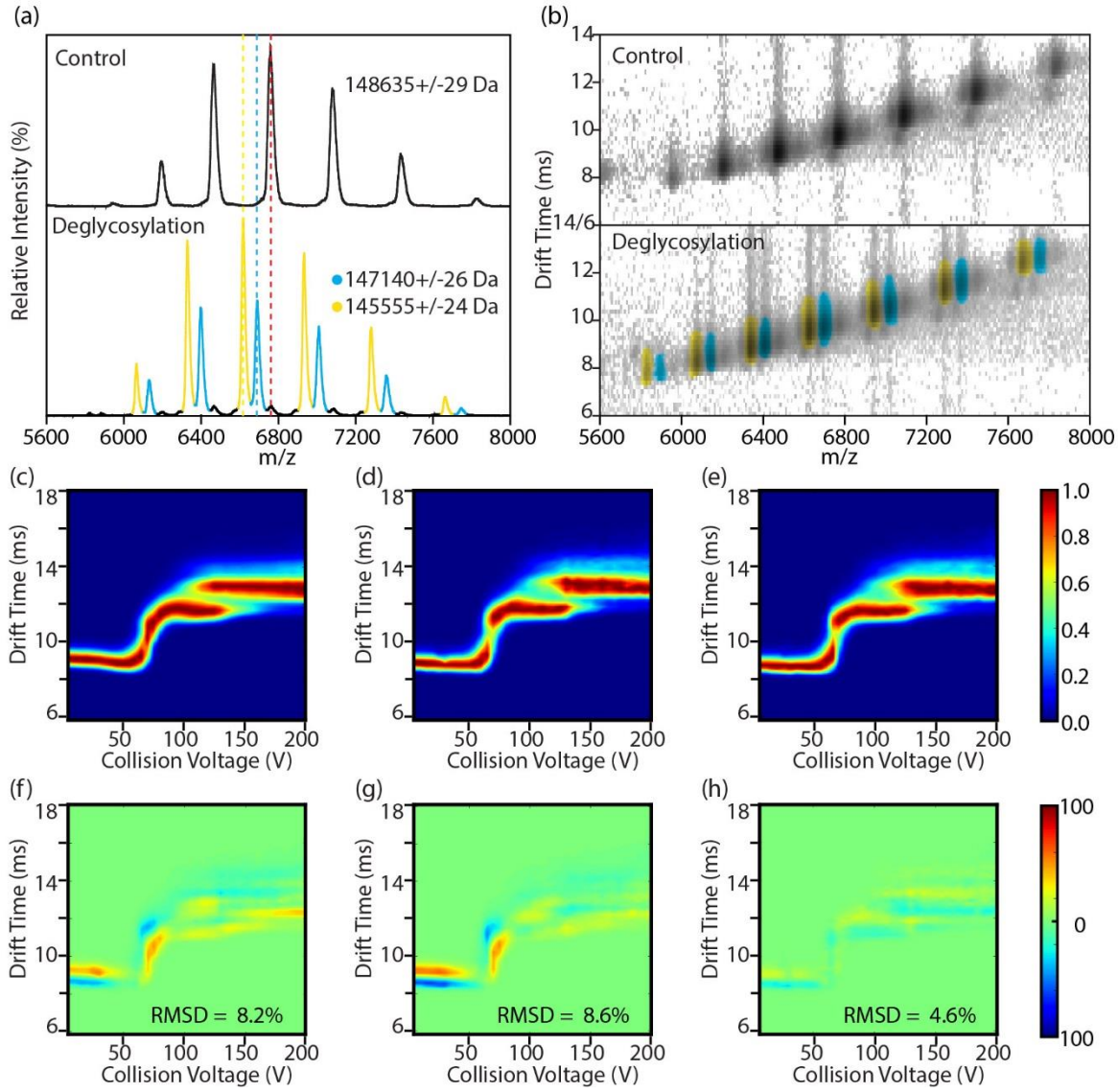

Figure 2-4. (a) MS spectra and (b) plots of drift time versus m/z for intact mAb standards under control and deglycosylating conditions, as labeled. Three ion species are observed after PNGase F incubation, corresponding to the intact mAb and two deglycosylated mAb species with mass differences of ~1500 Da and ~3000 Da, with 22^+ ions the base peak in all datasets. CIU fingerprints are generated for (c) intact mAb, (d) partially deglycosylated mAb, and (e) completely deglycosylated mAb. Difference plots are shown for (f) comparing intact mAb (red) with partially deglycosylated mAb (blue), (g) comparing intact mAb (red) with completely deglycosylated mAb (blue), and (h) comparison between two deglycosylation mAbs (partially deglycosylated mAb indicated in red color and fully deglycosylated mAb in blue). Drift times shift along collision voltage axis upon removal of N-linked glycosylations, whereas no differences are observed in unfolding patterns

deglycosylation of the antibody standard. In addition, shorter IM drift times are recorded for deglycosylated mAbs, as shown in Figure 2-4b, indicative of their decreased mass.

CIU data were then collected for quad selected 23^+ ions corresponding to fully modified, partially

modified, and fully deglycosylated mAbs (Figure 2-4c–e). Despite different IM drift times for the compact structures observed for these ions at low activation energies, the same number of CIU states are observed for all three mAb ion populations. These differences in drift times are carried forward during the CIU process, resulting in unfolded states for glycosylated samples with longer IM drift times relative to their deglycosylated analogues. To further quantify the variations in CIU caused by the level of glycosylation present within intact mAbs, fingerprint data were analyzed to create difference plots, through the subtraction of two CIU fingerprints and the plotting of the resulting data as a contour plot (Figure 2-4f–h). In addition, as described above, we also computed total fingerprint RMSD values in order to quantify the differences observed between different glycoforms. Large difference plot signals and relatively high RMSD values (>8%) are observed when comparing CIU data acquired for either glycoform observed with similar data for the fully deglycosylated form, with negligible differences observed between glycoforms. While some of these differentiating signals can be attributed to the IM drift time differentials discussed above, we also observe clear shifts in CIU stability, with glycoslyated forms requiring ~14% more activation voltage to undergo CIU than the deglycosylated analogue. Thus, these data support the sensitivity of the CIU response to the level of glycosylation present on intact mAbs, although apparently at a lower level than described above for differences associated with disulfide bonding.

2.4 Conclusions

Here, for the first time, we demonstrate the capabilities of CIU in the context of intact mAb analysis. IM-MS techniques have, by definition, direct access to antibody structure information through the measurement of IM drift times and ion CCSs and associated molecular modeling. However, as many disparate protein tertiary structures can exhibit the same intact CCS, they often comigrate during IM separations. CIU allows for the resolution of these iso-cross-sectional species

through their unfolding pathways. In the context of mAbs, we demonstrate a reproducible and quantitative ability of the CIU approach to differentiate intact antibodies based on their disulfide bonding numbers and patterns. This capability is likely driven by the differences in the interdomain connectivities found within the antibody constructs studied here, which differentially constrain the unfolded intermediates formed during CIU. In addition, we present data indicating that CIU response factors can be used to determine the general level of glycosylation within iso-cross-sectional ions, given a suitable reference data set.

We envision that the capabilities of CIU techniques demonstrated here will be highly enabling for the development of new therapeutic antibodies, as well as the differentiation of biosimilars. Solution-phase protein stability assays, while available in array formats, are typically too slow to be used at throughputs needed by current biotherapeutic development operations, largely due to the time required to raise the temperature of both the solvent and analytes during such measurements.[40] Since CIU acts on isolated mAbs in the gas-phase, such data can be acquired more rapidly. We conservatively estimate that such data can be acquired at a rate of 1000s of samples per day, using appropriate analysis software and sample introduction tools that maximize throughput.[41] Future CIU work in our laboratory will continue build complete mAb analysis workflows that add value to growing multiple attribute monitoring (MAM) analysis streams already in place. Ultimately, we envision CIU protocols capable of differentiating biosimlars from innovator biotherapeutics, removing mAb degradation pathways, optimizing conjugation in ADCs, and quickly assessing protein stabilities.

2.5 Supporting information

Supporting information can be found in Appendix I.

2.6 Acknowledgement

CIU method development in the Ruotolo group is supported by the National Science Foundation (CAREER, 1253384) and the University of Michigan department of chemistry.

2.7 References

(1) Rader, R. a. *Nat. Biotechnol.* **2008**, *26* (7), 743–751.
(2) Beck, A.; Wurch, T.; Bailly, C.; Corvaia, N. *Nat Rev Immunol* **2010**, *10* (5), 345–352.
(3) Wang, W.; Singh, S.; Zeng, D. L.; King, K.; Nema, S. *J. Pharm. Sci.* **2007**, *96* (1), 1–26.
(4) Wypych, J.; Li, M.; Guo, A.; Zhang, Z.; Martinez, T.; Allen, M. J.; Fodor, S.; Kelner, D. N.; Flynn, G. C.; Liu, Y. D.; Bondarenko, P. V; Ricci, M. S.; Dillon, T. M.; Balland, A. *J. Biol. Chem.* **2008**, *283* (23), 16194–16205.
(5) Dillon, T. M.; Ricci, M. S.; Vezina, C.; Flynn, G. C.; Liu, Y. D.; Rehder, D. S.; Plant, M.; Henkle, B.; Li, Y.; Deechongkit, S.; Varnum, B.; Wypych, J.; Balland, A.; Bondarenko, P. V. *J. Biol. Chem.* **2008**, *283* (23), 16206–16215.
(6) Jefferis, R. *Biotechnol. Prog.* **2005**, *21*, 11–16.
(7) Bertolotti-Ciarlet, A.; Wang, W.; Lownes, R.; Pristatsky, P.; Fang, Y.; McKelvey, T.; Li, Y.; Li, Y.; Drummond, J.; Prueksaritanont, T.; Vlasak, J. *Mol. Immunol.* **2009**, *46* (8-9), 1878–1882.
(8) Vázquez-Rey, M.; Lang, D. A. *Biotechnol. Bioeng.* **2011**, *108* (7), 1494–1508.
(9) De Groot, A. S.; Scott, D. W. *Trends Immunol.* **2007**, 28(11), 482–490.
(10) Narhi, L. O. *Biophysics for Therapeutic Protein Development*; Narhi, L. O., Ed.; Springer New York: New York, NY, 2013.
(11) Wang, L.; Amphlett, G.; Lambert, J. M.; Blättler, W.; Zhang, W. *Pharm. Res.* **2005**, *22* (8), 1338–1349.
(12) Fornelli, L.; Ayoub, D.; Aizikov, K.; Beck, A.; Tsybin, Y. O. *Anal. Chem.* **2014**, *86* (6), 3005–3012.
(13) Fornelli, L.; Damoc, E.; Thomas, P. M.; Kelleher, N. L.; Aizikov, K.; Denisov, E.; Makarov, A.; Tsybin, Y. O. *Mol. Cell. Proteomics* **2012**, *11* (12), 1758–1767.
(14) Majumdar, R; Middaugh, C. R.; Weis, D. D.; Volkin, D. B. *J. Pharm. Sci.* **2015**, 104 (2), 327-345.
(15) Mason, E. A.; McDaniel, E. W. *Transport Properties of Ions in Gases*; Wiley-VCH Verlag GmbH & Co. KGaA: Weinheim, FRG, 1988.
(16) Kanu, A. B.; Dwivedi, P.; Tam, M.; Matz, L.; Hill, H. H. *J. Mass Spectrom.* **2008**, 43(1), 1–22.
(17) Debaene, F.; Boeuf, A.; Wagner-Rousset, E.; Colas, O.; Ayoub, D.; Corvaïa, N.; Van Dorsselaer, A.; Beck, A.; Cianférani, S. *Anal. Chem.* **2014**, *86* (21), 10674–10683.
(18) Pacholarz, K. J.; Porrini, M.; Garlish, R. a; Burnley, R. J.; Taylor, R. J.; Henry, A. J.; Barran, P. E. *Angew. Chem. Int. Ed. Engl.* **2014**, *53* (30), 7765–7769.
(19) Bagal, D.; Valliere-Douglass, J. F.; Balland, A.; Schnier, P. D. *Anal. Chem.* **2010**, *82* (16), 6751–6755.
(20) Bhambure, R.; Kumar, K.; Rathore, A. S. *Trends Biotechnol.* **2011**, 29(3), 127–135.
(21) Razinkov, V. I.; Treuheit, M. J.; Becker, G. W. *Curr. Drug Discov. Technol.* **2013**, *10* (1), 59–70.

(22) Shelimov, K. B.; Jarrold, M. F. *J. Am. Chem. Soc.* **1997**, *119* (13), 2987–2994.
(23) Hyung, S.-J.; Robinson, C. V; Ruotolo, B. T. *Chem. Biol.* **2009**, *16* (4), 382–390.
(24) Han, L.; Hyung, S. J.; Mayers, J. J. S.; Ruotolo, B. T. *J. Am. Chem. Soc.* **2011**, *133* (29), 11358–11367.
(25) Han, L.; Hyung, S. J.; Ruotolo, B. T. *Angew. Chemie - Int. Ed.* **2012**, *51* (23), 5692–5695.
(26) Rabuck, J. N.; Hyung, S.-J.; Ko, K. S.; Fox, C. C.; Soellner, M. B.; Ruotolo, B. T. *Anal. Chem.* **2013**, *85* (15), 6995–7002.
(27) Laganowsky, A.; Reading, E.; Allison, T. M.; Ulmschneider, M. B.; Degiacomi, M. T.; Baldwin, A. J.; Robinson, C. V. *Nature* **2014**, *510* (7503), 172–175.
(28) Zhong, Y.; Han, L.; Ruotolo, B. T. *Angew. Chem. Int. Ed. Engl.* **2014**, *53* (35), 9209–9212.
(29) Eschweiler, J. E.; Rabuck-Gibbons, J.; Tian, Y.; Ruotolo, B. T. **2015**, submitted.
(30) Zhong, Y.; Hyung, S.-J.; Ruotolo, B. T. *Analyst* **2011**, *136* (17), 3534–3541.
(31) Giles, K.; Williams, J. P.; Campuzano, I. *Rapid Commun. Mass Spectrom.* **2011**, *25* (11), 1559–1566.
(32) Tito, M. A.; Tars, K.; Valegard, K.; Hajdu, J.; Robinson, C. V. *J. Am. Chem. Soc.* **2000**, *122* (14), 3550–3551.
(33) McKay, A. R.; Ruotolo, B. T.; Ilag, L. L.; Robinson, C. V. *J. Am. Chem. Soc.* **2006**, *128* (35), 11433–11442.
(34) Hernández, H.; Robinson, C. V. *Nat. Protoc.* **2007**, *2* (3), 715–726.
(35) Chowdhury, S. K.; Katta, V.; Chait, B. T. *J. Am. Chem. Soc.* **1990**, *112* (24), 9012–9013.
(36) Loo, J. A.; Loo, R. R.; Udseth, H. R.; Edmonds, C. G.; Smith, R. D. *Rapid Commun. Mass Spectrom.* **1991**, *5* (3), 101–105.
(37) Clemmer, D. E.; Jarrold, M. F. *J. Mass Spectrom.* **1997**, *32* (6), 577–592.
(38) UniProt Consortium, *Nucleic Acids Res.* **2015**, *43* (D1), D204–D212.
(39) Dalziel, M.; Crispin, M.; Scanlan, C. N.; Zitzmann, N.; Dwek, R. a. *Science* **2014**, *343* (January), 1235681.
(40) Torres, F. E.; Recht, M. I.; Coyle, J. E.; Bruce, R. H.; Williams, G. *Curr. Opin. Struct. Biol.* **2010**, 20(5), 598–605.
(41) Niu, S.; Rabuck, J. N.; Ruotolo, B. T. *Curr. Opin. Chem. Biol.* **2013**, *17* (5), 809–817.

Chapter 3. Collision Induced Unfolding Detects Subtle Differences in Intact Antibody Glycoforms and Associated Fragments

Yuwei Tian and Brandon T. Ruotolo, *International Journal of Mass Spectrometry*, 2018, **425**, 1–9. (DOI:10.1016/j.ijms.2017.12.005)

Abstract

Glycosylation has a significant impact on the effector function, immunogenicity, plasmatic clearance, and resistance towards proteases for monoclonal antibodies. Antibody glycoforms directly result in a form of structural heterogeneity due to the variety of sugar moieties and the available range of assembly states for the sugar linkages involved. Thus, the rapid characterization of antibody glycosylation is a critical yet challenging objective in the development of antibody-based therapeutics. Recently, we introduced an ion mobility-mass spectrometry approach for intact antibody analysis, which involves the collision induced unfolding of intact antibody ions. In this report, we demonstrate the use of such gas-phase unfolding analyses to differentiate subtly-different glycoforms within both intact antibody monomers and antibody Fc fragments, using minimal sample preparation and purification. We find evidence for a strong correlation between the gas-phase stabilities of antibody ions and the number of sugars attached to their sequences. We conclude by projecting the utility of our gas-phase unfolding assay in the context of antibody characterization workflows aimed at differentiating antibody glycoforms that cannot be readily resolved by MS alone.

3.1 Introduction

Biotherapeutics have gained an increasing share of the pharmaceutical market.[1,2] Among biotherapeutics, those based upon monoclonal antibodies (mAbs) are undoubtedly the fastest growing and most promising class due to their substantial pharmaceutical benefits.[3,4] One of these benefits is the relatively high specificity of mAbs for their target binding partner within cells, potentially leading to increased efficacy and lower incidence of side effects.[5,6] However, in comparison to small molecule drugs, antibody-based therapeutics are more compositionally and structurally heterogeneous, generating new challenges in their discovery and development. This situation frames the current need for technologies capable of rapidly capturing small differences in mAb structure and stability, especially in the context of the increasing availability of biosimilar mAb products.

Therapeutic mAbs are best described as a mixture of variants generated from post-translational modification and sequence degradation processes.[7] These variant forms include differential amounts of disulfide bond formation, glycosylation, C-terminal lysine, deamidation, oxidation, and aggregation.[8-12] This heterogeneity can lead to decreased drug efficacy and safety issues caused by immunogenicity.[13] Antibody glycosylation, typically N-linked through Asn 297, is a key mAb modification that can influence the affinity of antibodies to target receptors affect the efficacy through antibody-dependent cell-mediated cytotoxicity (ADCC), regulate protein plasmatic clearance, and alter resistance towards proteases.[10,14,15] As such, it is clear that a detailed characterization of antibody glycoforms is an important component of the development of any therapeutic mAb.

A wide range of chromatographic, spectroscopic, and mass spectrometric methods can be deployed for the qualitative and quantitative analysis of antibody glycosylation.[16] Beginning with the

introduction of soft ionization methods[17-19], MS-based methods have become an indispensable part of glycan analysis workflows[20,21]. Glycans may be released through enzymatic or chemical reactions and then be analyzed by MS in either their native form or derivatized forms, generating datasets that inform on glycan composition and sequence[22,23]. Bottom-up peptide mapping workflows, which involve enzymatic digestion of glycoproteins followed by LC–MS/MS analysis, are now routinely used to locate and quantify glycosylation within proteins at the peptide level[24,25]. In addition, the determination of specific glycosylation sites and glycan structures can be achieved via LC–MS/MS, typically in combination with electron-mediated activation methods[24-26].

Although bottom-up workflows are well-established both in terms of the chemical separations and MS techniques typically utilized, such analyses can be limited by incomplete peptide sampling, artifacts introduced from enzymatic digestion, and complex data processing. A more direct method involves the MS analysis of intact or partially digested mAbs in an effort to characterize the glycoforms present[20]. Several reports have demonstrated the power of high-resolution MS instruments in differentiating and quantifying antibody glycoforms directly through the analysis of intact protein ions[27-29]. Middle-down mAb analysis, which involves IdeS digestion to reduce the intact antibody to large (~50–100 kDa) fragments, has emerged as an alternative method that combines many of the strengths of both bottom-up and top-town methods[30]. In addition, ion mobility-mass spectrometry (IM-MS)[31,32], which separates analyte ions both by their orientationally-averaged size and mass, has enabled the identification of carbohydrate connectivity and configurational isomers and the differentiation of N-acetylneuraminic acid linkage isomers within glycopeptides[33-36]. Moreover, IM-MS has proven to be a useful and rapid probe of mAb higher-order structure under native conditions[37-39].

Despite the range of techniques and technologies arrayed in the analysis of mAb glycoforms, there

remain few approaches capable of capturing both glycoform structure information in conjunction with protein structure and stability. In this report, we investigate the capability of collision induced unfolding (CIU) for antibody glycoanalysis for both intact mAbs and Fc fragments. CIU technology involves the collisional activation of selected analyte ions in an ion trap prior to IM separation and in general acts to enrich the information content of IM-MS experiments conducted on intact proteins and protein complexes[40,41]. Modern CIU analyses have been used to investigate protein stability shifts upon anion or cation binding, differentiate protein tertiary structures in kinase–inhibitor complexes, explore membrane protein stabilization upon lipid binding, and probe native-state protein domain structure[42-46]. Previous work from our group has demonstrated the sensitivity of CIU to general levels of glycosylation within intact mAbs[47]. Here, for the first time, we demonstrate that CIU can also be used to distinguish subtle structural differences in antibody glycoforms. In addition, we are able to assign the gas-phase stability changes according to the detailed glycan structures through CIU comparisons of a control mAb and assorted antibody glycoforms. Finally, we discuss the utility of such CIU data for rapid glycoprotein characterization.

3.2 Experimental methods

Sample preparation

SILu™Lite SigmaMAb Universal Antibody Standard human (product number: MSQC4) was purchased from Sigma-Aldrich (St. Louise, MO). Glycerol-free PNGase F, Remove-iT Endo S, β 1–4 Galactosidase S, β-*N*-Acetylglucosaminidase S, α 1–6 Mannosidase, and α 1–2,3 Mannosidase were purchased from New England Biolabs (Ipswich, MA). Reaction Glycobuffers were provided along with the glycosidase enzymes. IdeS protease was obtained from Promega (Madison, WI). The powdered antibody standard sample was reconstituted into deionized water to a stock concentration of 2 mg/mL (~13 μM) and then aliquoted and stored at −80 °C until analysis. Sugar

residues were removed from N-linked glycans stepwise through enzymatic reactions under non-denaturing conditions.

To remove terminal galactose residues, 10 μL of mAb stock solution was mixed with 3 μL of 10× Glycobuffer 1 and further diluted by adding 7 μL of H_2O. Ten microliters of β 1–4 Galactosidase S was then added to this solution and the final mixture was then incubated at 37 °C for 24hr. To further cleave bisecting β-*N*-Acetylglucosamine residues, 10 μL of mAb stock solution was mixed with 3 μL of 10× Glycobuffer 1 and further diluted by adding 7 μL of H_2O. Ten microliters of β 1–4 Galactosidase S and 5 μL of β-*N*-Acetylglucosaminidase S were added to this mAb solution and incubated at 37 °C for 24 hr. Mannose residues were removed from the N-linked glycans by mixing 10 μL of mAb stock solution with 3.5 μL of 10× Glycobuffer 1, 10 μL β 1–4 Galactosidase S, 5 μL of β-*N*-Acetylglucosaminidase S, 2.5 μL of α 1–6 Mannosidase, 2.5 μL α 1–2,3 Mannosidase, and 0.34 μL of 100× BSA (New England Biolabs, Ipswich, MA), and incubating the final mixture at 37 °C for 24hr. Endo S was used to remove N-linked glycans from the chitobiose core of the heavy chain of native mAb, leaving the first *N*-Acetylglucosamine residue and fucose intact. All N-linked glycans were removed from the mAb using PNGase F. Ten microliters of mAb was diluted by adding 8 μL of water and mixed with 2 μL of 10× Glycobuffer 2 and 2 μL of PNGase F, and the final mAb solution was incubated at 37 °C for 24 hr. Fc fragments with various glycoforms were obtained by adding 0.4 μL of IdeS protease to the reactions described above. After incubation, the digested mAb samples were desalted and exchanged into a 500 mM ammonium acetate buffer using a Micro Bio-Spin P-6 column (Bio-Rad, Hercules, CA).

IM-MS data collection

Sample aliquots (~7 μL) were analyzed by IM-MS on a quadrupole-ion mobility-time-of-flight

mass spectrometer (Q-IM-ToF MS) instrument (Synapt G2 HDMS, Waters, Milford, MA)[48.49]. Antibody ions were generated using a nESI source in the positive mode. Voltages of 1.3 kV-1.6 kV were applied to the gold-coated capillary, and sampling cone was set at 60 V. The trap traveling-wave ion guide was pressurized to 3.4×10^{-2} mbar of argon gas. The traveling-wave ion mobility separator was operated at a pressure of ~2.5 mbar with wave height and wave velocity set at 40 V and 600 m/s, respectively. The ToF-MS was operated over the *m*/*z* range of 1000–10 000 at a pressure of 1.7×10^{-6} mbar. CIU experiments were performed in the trap region prior to IM separation as previously described.[47] For antibody monomer analysis, ions at *m*/*z* values corresponding to the 23+ charge state were selected in tandem-MS mode. The collisional voltages were ramped from 5 V to 200 V in 5 V intervals. For antibody Fc fragment measurements, ions at *m*/*z*values corresponding to the 12^{+} charge state were selected in tandem-MS mode. The collisional voltages were ramped from 5 V to 140 V in 5 V increments.

Data analysis

Mass spectra were calibrated externally using a solution of cesium iodide (100 mg/mL) and processed with Masslynx V4.1 software (Waters, Milford, MA). Drift time data was extracted at each collision voltage using TWIM Extract[50], and then analyzed using CIUSuite to plot CIU fingerprints, perform CIU comparisons, generate RMSD calculations, and produce feature analyses[51].

3.3 Results and discussion

Previous work from our group has shown that CIU is sensitive to the overall level of glycosylation within intact mAbs[47]. To further investigate the quantitive relationship between gas-phase mAb unfolding and the discrete levels of mAb glycosylation, we designed a series of experiments to test

CIU responses for a range of antibody glycoforms. The SILu™Lite SigmaMAb antibody standard was selected as a model system, which possesses a completely defined amino acid sequence and one N-linked glycan located within the Fc region of each heavy chain having known structure (Fig. 3-1A). This standard antibody is a human IgG1 consisting of a mixture of G0F, G1F, and G2F glycoforms. In order to create controlled series of antibody glycoforms, we carried out a series of enzymatic reactions on this IgG1 standard. For example, by incubating intact mAbs with galactosidase, the terminal galactose residues were removed, resulting in a homogeneous $(G0F)_2$ glycoform. The $(M3N2F)_2$ glycofrom was obtained by adding N-acetylglucosaminidase to further cleave β-*N*-acetylglucosamine residues from the glycan, yielding a theoretical mass difference of 812.78 Da compared to $(G0F)_2$glycoform. The $(M1N2F)_2$ glycoform was achieved through additional enzymatic reactions with α 1–6 mannosidase and α 1–2,3 mannosidase, leading to a 648.56 Da theoretical reduction in mAb molecular weight that corresponds to the loss of mannose residues. Deglycosylation of the mAb through a single enzymatic digestion with Endo S resulted in $(N1F)_2$ glycoform. And the glycosylation can be fully removed by incubating the mAb with PNGase F.

We recorded IM-MS spectra for all six mAb samples containing different levels of glycosylation under native conditions that preserve compact protein conformational states in the gas phase (Fig. 3-1B–G). Hence, we observe a narrow range of charge states (20^+–26^+) for all the antibody ions studied here. We recorded experimental masses by assigning mAb charge states based on those average mass values that produce the lowest standard deviation for all signals recorded in the MS spectrum (Table II-1). Due to the limited mass resolving power available in native MS experiments, the intact masses of the mAbs with native, G0F, and M3N2F glycans are nearly

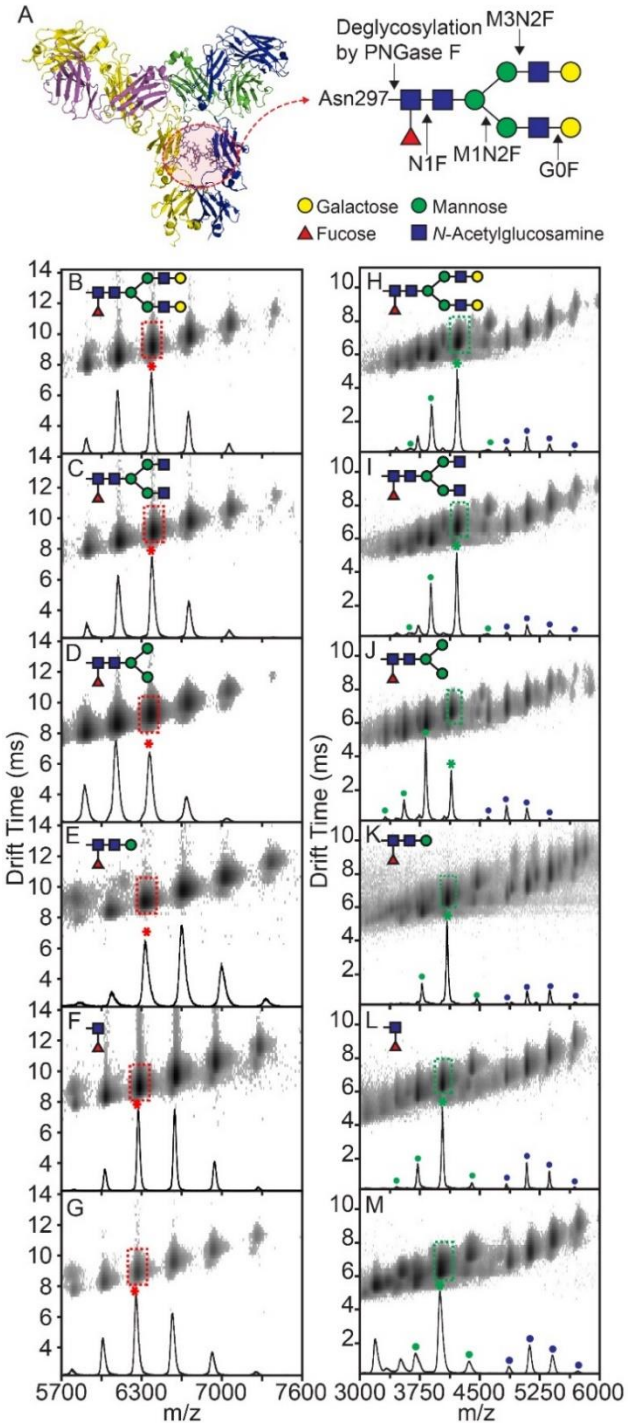

Figure 3-1. (A) Representation of IgG1 based on PDB ID 1HZH in combination with cartoon representations of the various N-linked glycan structures studied in this report. IM-MS data are shown, overlaid with native MS data, for antibody monomers containing native glycosylation patterns (B), G0F (C), M3N2F (D), M1N2F (E), N1F (F), and no glycosylation (G). The 23^+ charge state peaks were selected for downstream CIU analysis, and are highlighted using red dashed boxes and asterisks. IM-MS data for IdeS digested antibody samples having native or modified glycosylation patterns are shown in right panel (H–M) where the Fc fragment signals are labeled with green dots and $F(ab')_2$ peaks with blue. The 12^+ charge state Fc fragment ions were selected for CIU measurements, highlighted here using green dashed boxes and asterisks.

indistinguishable in our MS data. In order to confirm that N-linked glycans were properly altered through the enzymatic reactions described above, we performed an IdeS digest in order to cleave the mAb below the hinge region, yielding Fc and $F(ab')_2$ fragments. By measuring the intact mass of these fragments, we can confirm the expected modifications of N-linked glycan compositions described above (Table II-2).

We then collected CIU data for selected 23^+ ions of each antibody glycoform in triplicate, and the averaged CIU fingerprints are shown in Fig. 3-2A–F. Although the ground state IM drift times for some of the mAb glycoforms exhibit minor differences, all exhibit the same number of CIU features. This includes an initial compact feature (feature 1) observed at ~9 ms, and two additional unfolded conformers that appear at ~11.6 ms (feature 2) and ~13 ms (feature 3) respectively. In order to detect subtle differences in the mAb CIU fingerprints, we further analyzed the CIU data using the feature extraction function of CIUSuite (Table S3). Our results indicate that the drift times for feature 1 observed for $(G0F)_2$ glycoform and $(M3N2F)_2$ glycoform remain identical to that of the native mAb glycoform, whereas minor decreases in drift time are observed for this feature when further sugar units are stripped from the mAb. Such trends in centroid IM drift time are not observed for feature 2, but are again observed, although to a lesser extent, in feature 3.

In order to globally quantify the differences in CIU data discussed above, we generated CIU difference plots, where two CIU fingerprints are subtracted and color coded to reveal regions where each individual fingerprint possesses greater ion intensity (Figs. 3-2 and 3-3). In our analysis, we chose to compare each fingerprint of the modified mAb glycoforms with the CIU fingerprint of the native mAb (Fig. 3-2G–K). A root-mean-square-deviation (RMSD) value is computed as part of the analysis and reports on the absolute difference between two fingerprints compared. Similarly to the feature-centric discussion above, difference plot analysis reveals that

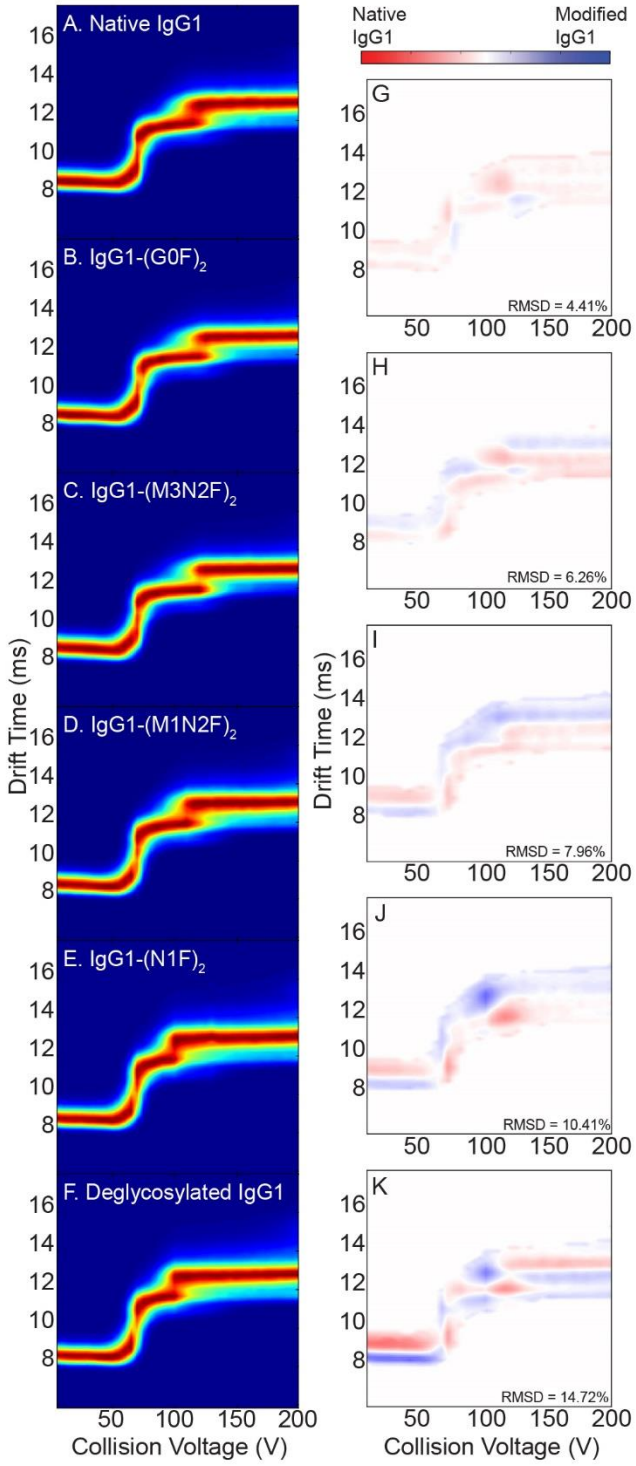

Figure 3-2. CIU analyses of 23^{+} antibody monomer ions. The left panel shows averaged CIU fingerprints recorded for IgG1 monomers having native glycosylation (A), modified glycosylation as indicated (B-E), and no glycosylation (F). CIU difference plots comparing native IgG1 (red) with IgG1 $(G0F)_2$ glycoforms (G, blue), $(M3N2F)_2$ glycoforms (H, blue), $(M1N2F)_2$ glycoforms (I, blue), $(N1F)_2$ glycoforms (J, blue), and deglycosylated IgG1 (K, blue). RMSD values are calculated to quantify the differences and shown on the corresponding plots.

the $(G0F)_2$ glycoform and native mAb have nearly identical CIU fingerprints overall, as evidenced by a low RMSD value of 4.41% (near the value recorded for similar comparisons where identical samples are used for comparison, 5.70%). As more sugar moieties are removed from the N-linked glycans, RMSD values computed from the CIU increase gradually until reaching a value of ~15%. This apparent trend leads us to conclude that the changes observed in the CIU fingerprints of these mAb glycoforms, though small, are linked to alterations in their glycan structures.

In order to quantify the strength of this trend, we plotted 1–RMSD values captured from our CIU difference analysis against the molecular weights of the N-linked glycosylation remaining on the analyzed mAbs (Fig. II-1 and Fig. 3-4). Greater similarities between fingerprints are denoted by higher 1–RMSD values. We attempted multiple fits for this data (Fig. II-1), ultimately observing that a quadratic function provides a superior fit to the other functional forms screened (R^2 value of 0.9945). The data clearly shows that the mAb glycoforms attached to the most complete glycan possesses the strongest similarity to the native mAb. As terminal sugars are removed from the mAb, the CIU fingerprint similarities decrease, most likely due to a combination of the altered mass, and concomitantly altered degrees of freedom, of the modified glycoforms, along with local conformational changes that influence the stability of the mAb ions overall. Fingerprint similarities decrease rapidly when additional sugar moieties, or all elements of glycosylation, are removed from the mAb. To illustrate the relative errors associated with our CIU comparisons, we also compared each CIU replicate to the averaged CIU fingerprint for the IgG monomer bearing native glycosylation and plotted the averaged 1–RMSD values (with standard deviations shown as error bars) against the molecular weights of the glycans attached (Fig. 3-4B). Here, the errors should be interpreted with caveat that they do not reflect the ultimate error limit for CIU technique, especially if narrow voltage ranges are utilized to minimize the impact of chemical noise on the ultimate

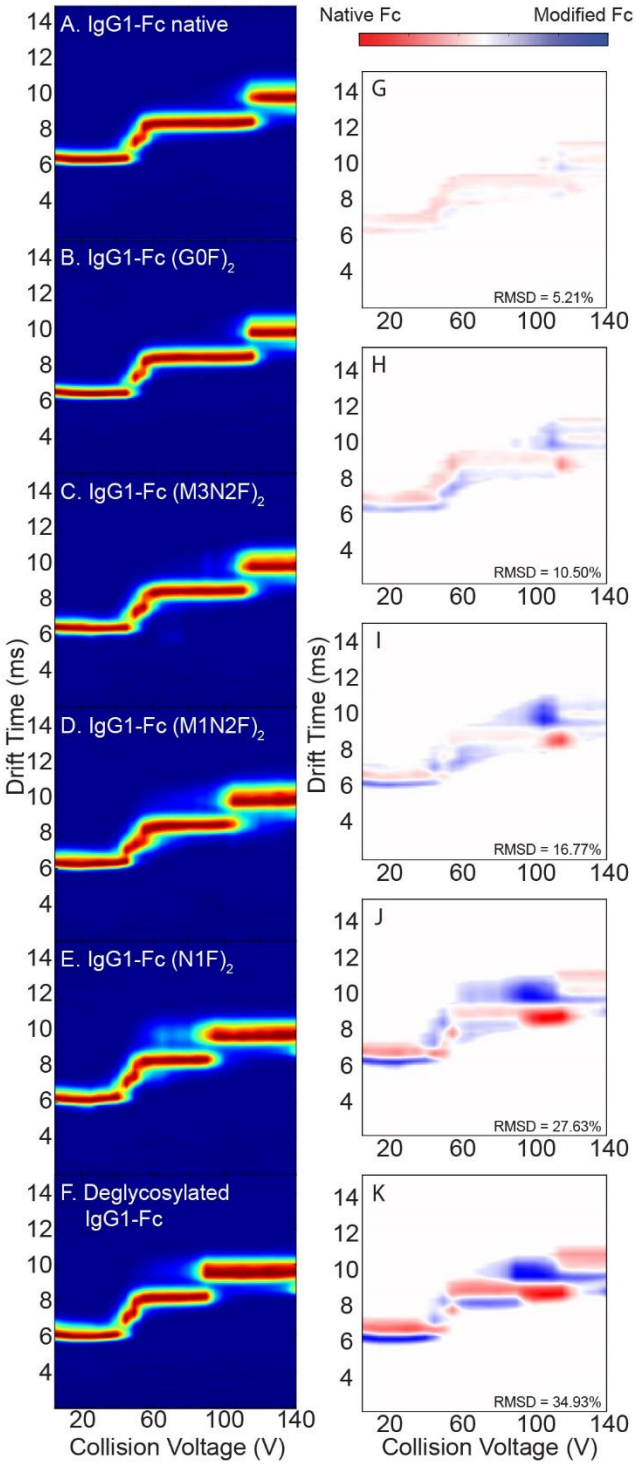

Figure 3-3. CIU analyses of 12^{+} antibody Fc fragments ions. Left panel shows averaged CIU fingerprints recorded for IgG1 monomers having native glycosylation (A), modified glycosylation patterns as indicated (B-E), and no glycosylation (F). CIU difference plots compare Fc fragment ions that bear native glycosylation (red) with Fc $(G0F)_2$ glycoforms (G, blue), $(M3N2F)_2$ glycoforms (H, blue), $(M1N2F)_2$ glycoforms (I, blue), $(N1F)_2$ glycoforms (J, blue), and deglycosylated IgG1 (K, blue). RMSD values are calculated to quantify the differences and shown on the corresponding plots.

analysis.

In addition to CIU analyses that consider broad collision voltage and drift time ranges, we explored our CIU data by focusing on specific voltage ranges (Fig. II-2). Our CIU feature analyses show that the removal of sugars moieties from the native mAb glyco-structure mainly results in shifts in the centroid of feature 1, as well altered voltage values for the transitions between all features observed during CIU. This analysis supports the observation that higher RMSD values are obtained for comparisons of data acquired below 100 V when compared with those values for entire CIU fingerprints. Furthermore, such an analysis suggests that the removal of glycosylation drives the starting gas-phase structure of the mAb toward more compact states and negatively impacts the stabilities of the resultant ions.

While the data shown in Figs. 3-2 and 3-4 reveals evidence of a clear correlation between CIU and the number of sugars bound to intact mAbs, the slope of the resulting correlation is shallow, indicating that the sensitivity of a CIU assay applied against intact mAb glycoforms may be relatively low. This result aligns with the fact that the mAbs in question owe just 2% of their intact mass to bound glycans. In order to extend the potential sensitivity of the CIU experiment to the mAb glycoforms discussed above, we initiated an IdeS protease digestion to generate similarly glycosylated Fc fragments. This procedure acts to roughly double the percent of the molecular weight associated with the glycans in our target analytes. IM-MS spectra for mAb Fc fragments attached to various glycans are shown in Fig. 3-1H–M. The resolving powers achieved in both the IM and MS domains are sufficient in these data to resolve all Fc and $F(ab')_2$ fragments, as well as separate all mAb fragment signals from other chemical interferants resulting from our enzymatic reaction conditions. The 12^+ charge state of the mAb Fc was selected to collect CIU data due to its large signal intensity (Fig. 3-1, green asterisks and dashed boxes). As observed for intact mAbs,

triplicate averaged CIU fingerprints for all Fc variants show the same numbers of CIU conformer families but exhibit different stabilities (Fig. 3-3A–F).

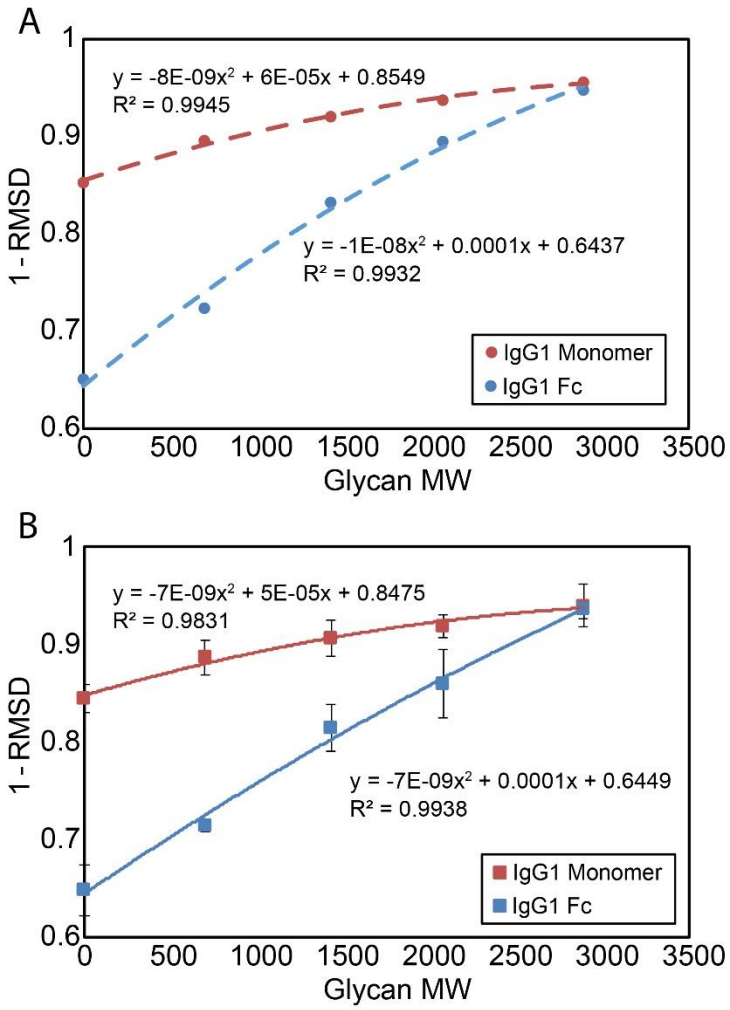

Figure 3-4. Plots of 1 - RMSD values against the molecular weights of N-linked glycans attached to antibody or Fc fragment ions accordingly. The RMSD values are either computed by comparing averaged CIU fingerprints (A) or averaged from CIU replicate comparisons with standard deviations shown as error bars (B). Similar trends are observed for these two plots. The fewer sugar moieties attached to the protein, the greater the difference detected by CIU, as reported by lower 1-RMSD values. Data is fitted into a quadratic function for both intact antibody ions (red) and Fc fragment ions (blue), both showing strong correlations. R^2 and equation values for each fit are displayed.

The feature extraction and detailed characterization of the conformer families accessed by Fc fragments through CIU reveal that G0F glycans bound fragments produce nearly identical CIU fingerprints to those generated by native Fc fragments (Table II-4). Similarly to intact mAb ions, the CIU data acquired for Fc fragments having undergone further glycan modifications exhibit progressive dissimilarities when compared to native Fc fragment CIU data, both in terms of the stabilities and the centroid IM times of the features detected. As above, we attribute the observed stability changes in Fc fragments to both the alterations in the overall degrees of freedom and the likely changes in conformation in the Fc region upon glycan modification.[52-54] Broad comparisons of Fc fragment fingerprints using

difference plots (Fig. 3-3G–K) result in RMSD values that report highest similarities between native and G0F glycan-containing Fc fragments (RMSD of 5.21%), and decreasing similarities as sugars are removed from the native glycoform. In contrast to our intact mAb data, we observe a greater range of RMSD values for our difference plot analysis for Fc fragments, producing values from ~5 to ~35%. These results confirm that alterations in glycan structure result in a larger relative impact on Fc fragment ion structure, stability and CIU behavior.

As above, we quantitatively examined the correlation between CIU and the level of Fc fragment glycosylation by plotting the molecular weights of the glycoforms attached to the ions analyzed against the 1 − RMSD values computed from the CIU difference plots (Figs. 3-4 and II-1). Similarly to intact mAbs, a strong quadratic (R^2 of 0.9932) correlation was observed, with lesser similarities detected between native Fc fragments and variant forms as the masses associated with the attached glycans are decreased. In contrast to our intact mAb analysis, the effective slope (or sensitivity) of the Fc fragment correlation is approximately a factor of three greater (Fig. II-1), revealing an improved ability to detect subtle differences in mAb glyco-structures over the intact mAb analysis discussed above. We rationalize this greater sensitivity as a direct result of the larger portion of the Fc composition that can be assigned to glycosylation, as well as the likely greater role that glycans play in Fc ion structure and stability. A detailed analysis of our Fc fragment CIU data reveals a larger degree of comprehensive differences than observed for intact mAbs, giving rise to the enhanced RMSD values observed in our difference plots. For example, comparing CIU data acquired for native Fc fragment to its fully deglycosylated analogue, produces RMSD values that are ~10% higher for the region above 75 V than for below (Fig. II-3). This trend is reversed if a similar analysis is performed on comparisons between CIU datasets acquired for more minor alterations to the native glycoforms. Taken together, these results reveal that Fc fragment

glycoforms are more comprehensively altered in terms of stability, including all CIU intermediate families to an extent not observed for intact mAb ions.

3.4 Conclusions

In summary, for the first time, we present evidence showing the ability of CIU to differentiate subtly-different antibody glycoforms. We are able to obtain an assortment of antibody glycoforms through a series of enzymatic reactions conducted under native conditions. Quantitative comparisons of CIU fingerprints acquired for these antibody glycoforms reveal changes in the gas-phase stabilities which increase upon removal of successive sugar residues from the native N-linked glycan. We interpret these observations as evidence of altered mAb structures and stabilities in the gas-phase, likely driven by local conformational changes in the Fc regions proximal to the altered N-linked glycans. Surprisingly, a strong quadratic correlation is observed between the molecular weights of N-linked glycans that remain attached to the mAbs and the RMSD values calculated through CIU fingerprint difference analyses. Overall, our data suggests that a rapid CIU assay can be used to quantitatively determine the amount of mAb N-linked glycosylation in Fc region, given a proper reference dataset and calibration, without the need for high mass resolving power.

While many reports exist that describe mAb glycosylation analysis[20-29,33,34], there is no dominant workflow currently embedded in the biotherapeutic development pipeline. As such, it is challenging to compare the available analytical methods for antibody glycoform analysis, as each adopts a distinct protocol and sample preparation strategy. One advantage of the native IM-MS and CIU approach described here is its potential speed and simplicity, since sample preparation is minimized in our workflow and only a small range of diagnostic voltages need to be recorded in order to quantify mAb glycosylation. Therefore, we envision that the CIU assay described in this

report would likely best be deployed as a quick, quantitative probe of glycosylation in the development phase of new therapeutic glycoproteins, as well as for the analysis of biosimilars[55], providing complementary structural and gas-phase stability information to the detailed glycan characterization by high resolution and denaturing MS. Future work in our lab will continue to build CIU into a validated analytical technique capable of merging information regarding mAb composition with data on protein structure and stability into a single, high-throughput assay.

3.5 Supporting Information

Supporting information can be found in Appendix II.

3.6 Acknowledgements

The authors would like to thank the National Science Foundation (CAREER 1253384) for support.

3.7 References

(1) Walsh, G. *Nat. Biotechnol.* 2014, *32* (10), 992–1000.
(2) Aggarwal, S. R. *Nat. Biotechnol.* 2014, *32* (1), 32–39.
(3) Reichert, J. M. *MAbs* 2012, *4* (3), 413–415.
(4) Ecker, D. M.; Jones, S. D.; Levine, H. L. *MAbs* 2015, *7* (1), 9–14.
(5) Scott, A. M.; Wolchok, J. D.; Old, L. J. *Nat. Rev.* 2012, *12* (4), 278–287.
(6) Chari, R. V. J.; Miller, M. L.; Widdison, W. C. *Angew. Chem. Int. Ed. Engl.* 2014, *53* (15), 3796–3827.
(7) Wang, W.; Singh, S.; Zeng, D. L.; King, K.; Nema, S. *J. Pharm. Sci.* 2007, *96* (1), 1–26.
(8) Walsh, G.; Jefferis, R. *Nat. Biotechnol.* 2006, *24* (10), 1241–1252.
(9) Wypych, J.; Li, M.; Guo, A.; Zhang, Z.; Martinez, T.; Allen, M. J.; Fodor, S.; Kelner, D. N.; Flynn, G. C.; Liu, Y. D.; Bondarenko, P. V; Ricci, M. S.; Dillon, T. M.; Balland, A. *J. Biol. Chem.* 2008, *283* (23), 16194–16205.
(10) Jefferis, R. *Biotechnol. Prog.* 2005, *21*, 11–16.
(11) Bertolotti-Ciarlet, A.; Wang, W.; Lownes, R.; Pristatsky, P.; Fang, Y.; McKelvey, T.; Li, Y.; Li, Y.; Drummond, J.; Prueksaritanont, T.; Vlasak, J. *Mol. Immunol.* 2009, *46* (8–9), 1878–1882.
(12) Vázquez-Rey, M.; Lang, D. A. *Biotechnol. Bioeng.* 2011, *108* (7), 1494–1508.
(13) De Groot, A. S.; Scott, D. W. *Trends Immunol.* 2007, *28* (11), 482–490.
(14) Dalziel, M.; Crispin, M.; Scanlan, C. N.; Zitzmann, N.; Dwek, R. a. *Science* 2014, *343* (January), 1235681.
(15) Jefferis, R. In *State-of-the-Art and Emerging Technologies for Therapeutic Monoclonal Antibody Characterization Volume 1. Monoclonal Antibody Therapeutics: Structure, Function,*

and Regulatory Space; ACS Symposium Series; American Chemical Society, 2014; Vol. 1176, pp 2–35.
(16) Lingg, N.; Zhang, P.; Song, Z.; Bardor, M. *Biotechnol. J.* 2012, *7* (12), 1462–1472.
(17) Fenn, J. B.; Mann, M.; Meng, C. K.; Wong, S. F.; Whitehouse, C. M. *Science* 1989, *246* (4926), 64–71.
(18) Tanaka, K.; Waki, H.; Ido, Y.; Akita, S.; Yoshida, Y.; Yoshida, T.; Matsuo, T. *Rapid Commun. Mass Spectrom.* 1988, *2* (8), 151–153.
(19) Karas, M.; Hillenkamp, F. *Anal. Chem.* 1988, *60* (20), 2299–2301.
(20) Wagner-Rousset, E.; Bednarczyk, A.; Bussat, M. C.; Colas, O.; Corvaïa, N.; Schaeffer, C.; Van Dorsselaer, A.; Beck, A. *J. Chromatogr. B Anal. Technol. Biomed. Life Sci.* 2008, *872* (1–2), 23–37.
(21) Dotz, V.; Haselberg, R.; Shubhakar, A.; Kozak, R. P.; Falck, D.; Rombouts, Y.; Reusch, D.; Somsen, G. W.; Fernandes, D. L.; Wuhrer, M. *TrAC - Trends Anal. Chem.* 2015, *73*, 1–9.
(22) Mauko, L.; Nordborg, A.; Hutchinson, J. P.; Lacher, N. a.; Hilder, E. F.; Haddad, P. R. *Anal. Biochem.* 2011, *408* (2), 235–241.
(23) Wada, Y.; Azadi, P.; Costello, C. E.; Dell, A.; Dwek, R. A.; Geyer, H.; Geyer, R.; Kakehi, K.; Karlsson, N. G.; Kato, K.; Kawasaki, N.; Khoo, K.-H.; Kim, S.; Kondo, A.; Lattova, E.; Mechref, Y.; Miyoshi, E.; Nakamura, K.; Narimatsu, H.; Novotny, M. V.; Packer, N. H.; Perreault, H.; Peter-Katalinic, J.; Pohlentz, G.; Reinhold, V. N.; Rudd, P. M.; Suzuki, A.; Taniguchi, N. *Glycobiology* 2007, *17* (4), 411–422.
(24) Kolarich, D.; Jensen, P. H.; Altmann, F.; Packer, N. H. *Nat Protoc* 2012, *7* (7), 1285–1298.
(25) Du, Y.; May, K.; Xu, W.; Liu, H. *J. Am. Soc. Mass Spectrom.* 2012, *23* (7), 1241–1249.
(26) Singh, C.; Zampronio, C. G.; Creese, A. J.; Cooper, H. J. *J. Proteome Res.* 2012, *11* (9), 4517–4525.
(27) Zhang, J.; Liu, H.; Katta, V. *J. Mass Spectrom.* 2010, *45* (1), 112–120.
(28) Rosati, S.; Rose, R. J.; Thompson, N. J.; Van Duijn, E.; Damoc, E.; Denisov, E.; Makarov, A.; Heck, A. J. R. *Angew. Chemie - Int. Ed.* 2012, *51* (52), 12992–12996.
(29) Rosati, S.; Van Den Bremer, E. T.; Schuurman, J.; Parren, P. W.; Kamerling, J. P.; Heck, A. J. *MAbs* 2013, *5* (6), 917–924.
(30) Woodard, J.; Lau, H.; Latypov, R. F. *Anal. Chem.* 2013, *85* (13), 6429–6436.
(31) Mason, E. A.; McDaniel, E. W. *Transport Properties of Ions in Gases*; Wiley-VCH Verlag GmbH & Co. KGaA: Weinheim, FRG, 1988.
(32) Kanu, A. B.; Dwivedi, P.; Tam, M.; Matz, L.; Hill, H. H. Ion mobility-mass spectrometry. *Journal of Mass Spectrometry*, 2008, *43*, 1–22.
(33) Damen, C. W. N.; Chen, W.; Chakraborty, A. B.; van Oosterhout, M.; Mazzeo, J. R.; Gebler, J. C.; Schellens, J. H. M.; Rosing, H.; Beijnen, J. H. *J. Am. Soc. Mass Spectrom.* 2009, *20* (11), 2021–2033.
(34) Olivova, P.; Chen, W.; Chakraborty, A. B.; Gebler, J. C. *Rapid Commun. Mass Spectrom.* 2008, *22* (1), 29–40.
(35) Both, P.; Green, A. P.; Gray, C. J.; Šardzík, R.; Voglmeir, J.; Fontana, C.; Austeri, M.; Rejzek, M.; Richardson, D.; Field, R. A.; Widmalm, G.; Flitsch, S. L.; Eyers, C. E. *Nat Chem* 2014, *6* (1), 65–74.
(36) Hinneburg, H.; Hofmann, J.; Struwe, W. B.; Thader, A.; Altmann, F.; Varón Silva, D.; Seeberger, P. H.; Pagel, K.; Kolarich, D. *Chem. Commun.* 2016, *52*, 4381–4384.
(37) Campuzano, I. D. G.; Larriba, C.; Bagal, D.; Schnier, P. D. In *ACS Symposium Series*; 2015; Vol. 1202, pp 75–112.

(38) Debaene, F.; Bœuf, A.; Wagner-Rousset, E.; Colas, O.; Ayoub, D.; Corvaïa, N.; Van Dorsselaer, A.; Beck, A.; Cianférani, S. *Anal. Chem.* 2014, *86* (21), 10674–10683.
(39) Pacholarz, K. J.; Porrini, M.; Garlish, R. a; Burnley, R. J.; Taylor, R. J.; Henry, A. J.; Barran, P. E. *Angew. Chem. Int. Ed. Engl.* 2014, *53* (30), 7765–7769.
(40) Shelimov, K. B.; Jarrold, M. F. *J. Am. Chem. Soc.* 1997, *119* (13), 2987–2994.
(41) Hyung, S.-J.; Robinson, C. V; Ruotolo, B. T. *Chem. Biol.* 2009, *16* (4), 382–390.
(42) Han, L.; Hyung, S. J.; Mayers, J. J. S.; Ruotolo, B. T. *J. Am. Chem. Soc.* 2011, *133* (29), 11358–11367.
(43) Han, L.; Hyung, S.-J.; Ruotolo, B. T. *Angew. Chemie Int. Ed.* 2012, *51* (23), 5692–5695.
(44) Rabuck, J. N.; Hyung, S.-J.; Ko, K. S.; Fox, C. C.; Soellner, M. B.; Ruotolo, B. T. *Anal. Chem.* 2013, *85* (15), 6995–7002.
(45) Laganowsky, A.; Reading, E.; Allison, T. M.; Ulmschneider, M. B.; Degiacomi, M. T.; Baldwin, A. J.; Robinson, C. V. *Nature* 2014, *510* (7503), 172–175.
(46) Zhong, Y.; Han, L.; Ruotolo, B. T. *Angew. Chem. Int. Ed. Engl.* 2014, *53* (35), 9209–9212.
(47) Tian, Y.; Han, L.; Buckner, A. C.; Ruotolo, B. T. *Anal. Chem.* 2015, *87* (22), 11509–11515.
(48) Zhong, Y.; Hyung, S.-J.; Ruotolo, B. T. *Analyst* 2011, *136* (17), 3534–3541.
(49) Giles, K.; Williams, J. P.; Campuzano, I. *Rapid Commun. Mass Spectrom.* 2011, *25* (11), 1559–1566.
(50) Haynes, S. E.; Polasky, D. A.; Dixit, S. M.; Majmudar, J. D.; Neeson, K.; Ruotolo, B. T.; Martin, B. R. *Anal. Chem.* 2017, acs.analchem.7b00112.
(51) Eschweiler, J. D.; Rabuck-Gibbons, J. N.; Tian, Y.; Ruotolo, B. T. *Anal. Chem.* 2015, *87* (22), 11516–11522.
(52) Matsumiya, S.; Yamaguchi, Y.; Saito, J. ichi; Nagano, M.; Sasakawa, H.; Otaki, S.; Satoh, M.; Shitara, K.; Kato, K. *J. Mol. Biol.* 2007, *368* (3), 767–779.
(53) Houde, D.; Arndt, J.; Domeier, W.; Berkowitz, S.; Engen, J. R. *Anal. Chem.* 2009, *81* (7), 2644–2651.
(54) Subedi, G. P.; Barb, A. W. *Structure* 2015, *23* (9), 1573–1583.
(55) Pisupati, K.; Tian, Y.; Okbazghi, S.; Benet, A.; Ackermann, R.; Ford, M.; Saveliev, S.; Hosfield, C. M.; Urh, M.; Carlson, E.; Becker, C.; Tolbert, T. J.; Schwendeman, S. P.; Ruotolo, B. T.; Schwendeman, A. *Anal. Chem.* 2017, *89* (9), 4838–4846.

Chapter 4. Quantitative Collision Induced Unfolding Differentiates Antibody-Drug Conjugates

Antibody-drug conjugates (ADCs) are antibody-based therapeutics that have proven to be highly effective cancer treatment platforms. They are comprised of monoclonal antibodies conjugated with highly potent drugs via chemical linkers. Various conjugation strategies can lead to a high degree of structural heterogeneity, and thus it is important to evaluate the impact of conjugation on antibody conformation. Here, we present a workflow involving native Ion Mobility (IM)-MS and gas-phase unfolding for the structural characterization of lysine-linked antibody-biotin conjugates. Following the determination of conjugation states via denaturing Liquid Chromatography-Mass Spectrometry (LC-MS) measurements, we performed both Size Exclusion Chromatography (SEC) and native IM-MS measurements in order to compare the structures of biotinylated and unmodified antibodies. Hydrodynamic viscosity radii (Rh) and collision cross section (CCS) values were insufficient to distinguish the conformational changes in these antibody-biotin conjugates owing to their flexible structures and limited instrument resolution. In contrast, collision induced unfolding (CIU) analyses were able to detect subtle structural and stability differences in the mAb upon biotin conjugation. Destabilization of biotinylated mAbs was detected by both CIU and differential scanning calorimetry (DSC) data, suggesting a previously unknown correlation between the two measurement tools. We conclude by discussing the impact of IM-MS and CIU technologies on the future of ADC development pipelines.

4.1 Introduction

Chapter 2 Antibody-drug conjugates (ADCs) have become a promising class of therapeutics for the treatment of cancer, underscored by the four ADCs currently approved by the US FDA, and the more than 60 ADCs in various clinical trial stages.[1–4] ADCs consist of monoclonal antibodies (mAbs) that are covalently attached to highly potent drugs through chemical linkers comprised of relatively labile bonds. Such conjugation allows for the high selectivity of mAbs to be combined with cytotoxic drugs, achieving discrimination between healthy and diseased tissue in contrast to traditional chemotherapies. While both cysteine and lysine-targeted chemistries are widely used in ADC generation,[5–7] the latter typically results in a more heterogeneous drug-to-antibody ratio (DAR) distribution, often creating therapeutics with increased structural complexity, owing to the large number of lysine residues in mAb sequences.[8–10]

Chapter 3 Conjugated species, which differ in terms of their levels and sites of drug incorporation, can potentially exhibit differential structures and pharmacokinetic properties.[6] As such, DAR values are considered critical quality attributes of ADCs, necessitating the development of a range of analytical methods for their quantitative evaluation. For example, many separation techniques have been utilized to accurately derive DAR values, such as hydrophobic interaction chromatography (HIC), ion exchange chromatography (IEC), reverse phase liquid chromatography (RPLC), capillary electrophoresis (CE), or capillary isoelectric focusing (cIEF).[8,10–12] As lysine-conjugated ADCs typically exhibit greater heterogeneity and poorer chromatographic peak shapes than equivalent cysteine-modified therapeutics, mass spectrometry (MS) is typically deployed for their DAR assessment.[8,13,14] Recently, native mass spectrometry has been increasingly applied for ADC analysis, providing highly accurate DAR values under native conditions, which are especially critical for capturing accurate values produced by cysteine-linked

modification chemistries.[7,15–17] Moreover, with advances in high-resolution instrumentation for native MS experiments, DAR values can often be readily extracted from ADCs prepared at physiologically-relevant pH.[18–22]

Chapter 4 In addition to DAR values, it is also of critical importance to assess the impact of conjugation chemistries on mAb higher order structures (HOS). Biophysical assays, such as Differential scanning calorimetry (DSC), have been broadly used in the biopharmaceutical industry for assessing such HOS effects in ADCs, but often only limited information is obtained from such data.[23,24] Recently, MS-based techniques have emerged as an important class of tools for protein HOS characterization. Among these, hydrogen-deuterium exchange (HDX)-MS has been used to compare the overall conformation and flexibility of ADCs to their parent mAbs.[7,25] Despite its ability to access localized structure information in large therapeutic proteins, HDX-MS experiments often take a long time to perform and analyze. Thus, there is a growing need for high-throughput structural probes of ADC structure as a function of conjugation state and formulation that can operate in both development and quality assessment roles.

Chapter 5 The combination of ion mobility (IM) and MS has proven to be a useful tool for the characterization of mAbs and ADCs, by separating such proteins according to their size and recording their ion-neutral collision cross sections (CCSs) as a means of HOS analysis.[15,26–28] In an effort to assess antibody structures in greater detail, collision induced unfolding (CIU) experiments can be performed.[29] This technology involves the collisional activation of protein ions prior to IM-MS separation in order to initiate protein unfolding events in the gas-phase. CIU is capable of differentiating IgG subclasses, detecting minor alterations in mAb glycoforms, assessing stability shifts associated with site-specific ADCs, and evaluating the comparability of biosimilars.[30–34]

Chapter 6 In this report, we present a CIU based workflow for the rapid characterization of a human IgG1 mAb conjugated with biotin via its native lysine residues, which we treat as an ADC model system. Despite the high degree of structural similarity revealed across conjugation states revealed by native IM-MS, our CIU results indicate the presence of subtle structural changes in the mAbs upon biotin conjugation, as revealed by shifts in their overall stabilities and ground state CCSs. Through comparative analysis, we are able to correlate the differences observed in our CIU data with the DAR values quantified using LC-MS, measured under denaturing conditions. We conclude by discussing the benefits of native IM-MS and CIU assays for ADC characterization.

4.2 Materials and Methods

Biotinylation of mAb

A human IgG1 mAb standard at 2 mg/mL in 50 mM sodium phosphate buffer, 2 mM ethylenediaminetetraacetic acid (EDTA), pH 7.5 was alkylated with 5, 10, 15, 20, and 30 equivalents of EZ-Link sulfo-NHS-LC-Biotin (Peirce) for 60 min at RT. Unreacted LC-biotin was removed through repeated buffer exchange with phosphate buffer saline (PBS) in Amicon ultra-0.5 mL 30 kDa. For deglycosylated samples, PNGaseF was added to the biotinylated products, and the reaction mixtures were incubated overnight at 37 °C. The final products for MS analysis were obtained from size exclusion purification.

Denaturing LC/MS

LC-MS measurements were performed on an Agilent 6230 TOF LC/MS system with a 1290 Infinity LC system. Intact protein samples were separated on a Zorbax SB300-C8 3.5 µm 2.1 x 50 mm column at a temperature of 75 ºC. Mobile phase A was 0.1% TFA in water and mobile phase B was 0.1% TFA in 90% n-propanol. About 5 µg of each sample was loaded and eluted with a

gradient of 20-70% B from 1.0 to 9.0 minutes at a flow rate of 0.2 mL/min, following the initial 20% B condition. Mobile phase B was then increased from 70% to 100% B from 9.0 to 10.0 minutes and remained at 100% for 1 further minute. MS data was acquired over the m/z range 1000 – 7000. Ions were generated at ESI capillary voltage of 5.9 kV and the gas temperature of 340 ºC. Drying gas was 13 L/min and nebulizer was 25 psig. The source fragmentor was set at 460 V, with skimmer set at 95 V and octapole 1 RF operating at 800 V (peak-to-peak). The oa-ToF was calibrated using the Agilent Tune Mix using the automated calibration procedure implemented through MassHunter Data Acquisition (Agilent).

Native ion mobility-mass spectrometry (IM-MS) and Collision Induced Unfolding (CIU)

Native IM-MS data were acquired either on a travelling wave ion mobility (TWIM) mass spectrometer, Synapt G2 HDMS instrument, or on a Synapt HDMS instrument modified with an RF-confining drift cell. For the CCS measurements on TWIMS instrument, samples were buffer exchanged into 100 mM ammonium acetate using Bio-rad microspin column with 6 kDa MWCO. The nESI voltage was set at 1.1 kV to 1.3 kV, and sampling cone was set at 60 V. The traveling-wave ion mobility separator was operated at a pressure of ~2.5 mbar with wave height and wave velocity set at 14 V and 300 m/s, respectively. IM wave velocity and wave height were optimized to achieve higher accuracy in CCS measurements with a bit trade off in the arrival time resolution. To derive the CCS(Ω) values, protein drift times measured in the TWIM device were calibrated using the protein standards concanavalin A (Con A), alcohol dehydrogenase (ADH), and pyruvate kinase (PK). The ToF-MS was operated over the m/z range of 1000–10 000 at a pressure of 1.5×10^{-6} mbar. CIU experiments were performed in the trap region prior to IM separation on a Synapt G2 HDMS instrument as previously described. The antibody ions at desired charge state were selected by the high m/z transmission quadrupole. The trap collision voltage was applied on the

selected protein ions incrementally ramping from 5 V to 200 V by 5 V. The ion mobility traveling wave height was set to 40 V and the wave velocity was set to 600 m/s.

MS Data Analysis

Denaturing LC/MS data was extracted and deconvoluted using MassHunter Qualitative Analysis Software (Agilent). Native mass spectra were calibrated externally using a solution of cesium iodide (100 mg/mL) and processed with Masslynx V4.1 software (Waters, Milford, MA). CIU data was extracted using TWIMExtract[35] and analyzed using the CIUSuite[36] to generate CIU plots and perform CIU comparisons. Root-mean-square deviation (RMSD) values were computed from a pixel-to-pixel comparison of two CIU fingerprints. In order to analyze the IM peak widths in CIU data, IM arrival time distributions observed at each collision voltage was modeled as a sum of Gaussian components. Components were added sequentially until the goodness of fit (r^2) exceeded 0.99, allowing optimized fitting without over-fitting. CIU features in the dataset are detected by grouping observed arrival time peaks that are present across multiple collision voltages. The tolerance (allowed deviation) from a median drift time was three drift bins, and the minimum number of collision voltages required for feature fitting was three (or 10 V range). Following feature detection, the transition region between features is fitted to a logistic (generalized sigmoid) function. The logistic function parameters describe the lower and upper asymptotes (centroid drift times of the features before and after the transition), the growth rate or steepness of the transition, and the midpoint voltage, which we term the "CIU-50" value.

Differential Scanning Calorimetry (DSC)

DSC experiments were performed on a Nano DSC instrument (TA Instrument, New Castle, DE). IgG1-biotin samples were buffer exchanged in to 100 mM ammonium acetate, pH 7.1 buffer and

diluted to ~ 0.5 mg/mL. Accurate concentration was determined from UV absorbance at 280 nm. 300 µL of the protein solution was loaded to the capillary sample cell with the reference cell with ammonium acetate buffer. The chamber was pressurized to 3 atm and the temperature ramped from 25 °C to 95 °C at 1 °C/min heating rate. The recorded DSC thermograms were baseline subtracted and subjected to a multi-component Gaussian fitting in the NanoAnalyze software (TA Instrument, New Castle, DE). The temperatures for three major transitions were extracted from the fitted Gaussian models, relating to the unfolding of C_H2, Fab, and C_H3 domains respectively. Replicates were not available for each sample. Thus, we used a conservative value of 1 °C as the cutoff limit for evaluating the significance of the differences observed in melt temperatures.

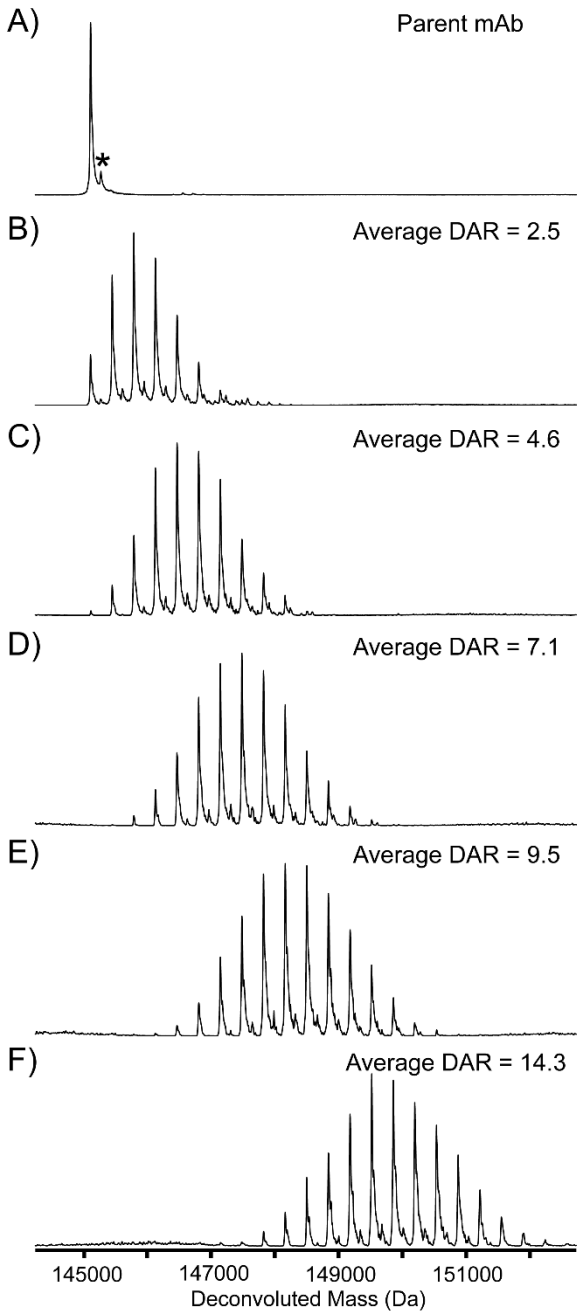

Figure 4-1. (A) Deconvoluted mass spectrum for deglycosylated parent mAb recorded from denaturing LC-MS analysis. One main species is observed with one low intensity species corresponding to glycated mAb (asterisk labeled). (B-F) Zero charge mass spectra for biotinylated mAbs under same experiment conditions. Average DAR for each IgG1-biotin sample is calculated based on the peak area.

4.3 Results and Discussion

Determining DAR values from denaturing LC-MS measurements

The conjugation of one biotin to the lysine residue yields a mass addition of 339.5 Da. After the conjugation reaction, the parent mAb and the resulting ADCs models were subjected to denaturing LC-MS analysis to assess both the distribution of attached biotins produced, as well as their DAR values (Figure III-1.). Under denaturing MS conditions, the resolution of different glycoforms (G0F, G1F, G2F) is achieved for the parent mAb. However, the charge state distributions for biotinylated mAbs overlap significantly as more conjugation events are achieved, producing ADC mimics of increasing heterogeneity. As expected, individual biotin conjugation states cannot readily be differentiated from antibody glycoforms in LC-MS data acquired under denaturing conditions. To obtain accurate biotin-to-antibody ratios, protein samples were treated with PNGase F under native conditions in order to remove all N-linked glycans and reduce the heterogeneity of our model ADCs. Denaturing LC-MS data acquired for the deglycosylated samples reveals primarily a single peak for the parent deglycosylated mAb (Figure 4-1). Experimental masses calculated for deglycosylated biotinylated antibodies range from 145.1kDa to 152.2kDa, comprising mAb species with 0 to 21 biotins attached. Average DAR values were calculated using the deconvoluted mass peak areas recorded in these experiments. Based on these results, reacting IgG 1 with 5 eqv., 10 eqv., 15 eqv., 20 eqv., and 30 eqv. of biotin under the conditions described yielded mAb-biotin conjugates with average DAR values of 2.5, 4.6, 7.1, 9.5, and 14.3 respectively.

Native IM-MS analysis reveals similar native gas-phase structures for antibody-biotin conjugates

Although LC-MS is a well-validated method to determine DAR values for lysine-linked ADCs, it is unable to assess native mAb structures upon conjugation. To obtain more structural information, we analyzed the biotinylated mAbs by IM-MS under native-like solution conditions. Figure 4-2A displays the mass spectra for glycosylated ADCs, occupying a much narrower charge state

envelope (from 21+ to 26+) when compared to typical denaturing MS data. As highlighted in the mass spectra, signals for the 23+ charge state shift to higher m/z values when more biotin equivalents are added for the conjugation reaction, indicating increased mAb molecular mass values. In order to preserve compact mAb structures in the gas phase we limited the amount of activation experienced by mAb ions in our experiments. These conditions result in broader features in the resulting mass spectra, produced through the nonspecific binding of buffer components to mAbs which are carried into the gas phase, and make resolution of either glycoforms or biotin conjugation states impossible. Thus, for the data shown in Figure 4-2, the intact masses of detected mAbs were computed based on the recorded centroid m/z values of the observed charge states. Our measurements indicate an average mass of 148.92 ± 0.06 kDa for the parent mAb, which increases linearly as a function of equivalents of biotin added for ADC model production, terminating in an intact mass of 154.02 ± 0.16 kDa, recorded for the sample containing 30 equivalents of biotin (Figure 4-2C, blue). Relative average mass differences between the biotinylated mAbs and the parent mAb were calculated to estimate the average DAR values for each IgG1-biotin sample, producing of 1.8, 4.8, 6.5, 8.2, and 15.0 respectively.

To better resolve these conjugates by native IM-MS, we analyzed deglycosylated ADC models as discussed above, and observed narrower peak MS widths as expected (Figure 4-2B). These data produced measured intact ADC masses ranging from 145.58 ± 0.05 kDa to 150.23 ± 0.17 kDa (Figure 4-2C, orange) and DAR values of 2.1, 4.5, 6.7, 9.6, and 13.7 for samples produced from reactions using increasing equivalents of biotin. We note that the DAR values extracted from native MS are systematically lower than those obtained by LC-MS, and importantly, if the peak widths or mass resolving power of our native MS data are taken into account (dashed line in Figure

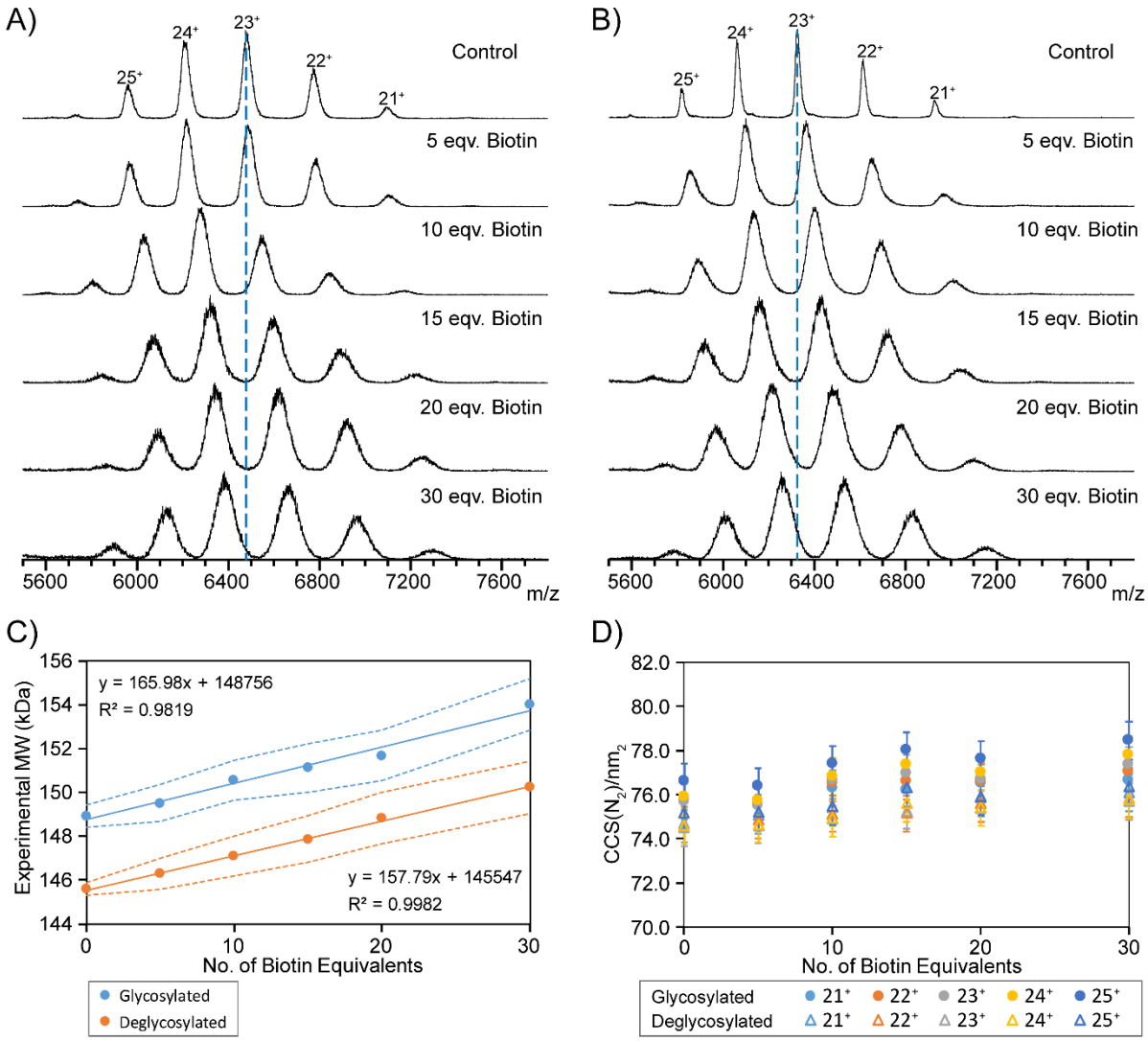

Figure 4-2. Overlay of the native MS spectra for (A) glycosylated and (B) deglycosylated IgG1-biotins. The 23^+ charge state of the parent mAb is highlighted by the blue dashed line. (C) The average masses are calculated and plotted against the number of biotin equivalents reacted with the mAb. The peak width or mass resolution is shown as dashed line. (D) CCS values in nitrogen derived from TWIMS measurements are shown for each charge state of each sample.

4-2C), the discrimination between some of the IgG1-biotins states is challenging to accomplish at high confidence.

In order to characterize the gas-phase structures of IgG1-biotin conjugates produced under native-like conditions and evaluate the ability of IM-MS alone to differentiate our group of ADC mimics, a comprehensive series of CCS measurements were carried out. The CCS values for each charge state of the ADC samples in nitrogen acquired by TWIM are shown in Figure 4-2D. CCS values

averaged over all observed charge states range from 76.2±0.8 nm^2 to 77.8±1.0 nm^2 for glycosylated mAbs, and from 75.0±0.7 nm^2 to 76.2±0.6 nm^2 for their deglycosylated analogues. IM analyses were also performed on an RF-confining drift tube device containing helium. (Table 4-1 and Table III-1) Overall, measured CCS values for ADC models produced from reaction conditions containing 30 biotin equivalents differ by ~2% when compared with unmodified IgG1 ions, indicating that only minor changes in global mAb structure take place upon biotin conjugation. The absolute sizes of the parent mAbs and the biotinylated mAbs in solution were measured by SEC-MALS/QELS (size-exclusion chromatography equipped with multi-angle light scattering and quasi-elastic light scattering detectors) and reported as hydrodynamic radius (R_h) values. (Table 4-1 and Table III-1) Similarly, all the ADC mimics have indistinguishable R_h values in solution. We note a structural compaction of ~22% for both parent mAb and mAb-biotin conjugates in the gas phase, when comparing experimental CCS values with the CCS values derived from R_h using the equation described by Hewitt et al.[37], consistent with previous reports.[26,27] Taken together, native IM-MS analysis results suggest the presence of similarly compact gas-phase structures for the IgG1-biotin conjugates compared to the unmodified mAb.

Table 4-1. Travelling wave ion mobility (TWIM) derived CCS values in nitrogen, RF-confining Drift Cell measured CCS values in helium, and SEC-MALS/QELS determined hydrodynamic radius.[a] (For full list, see Table III-1)

	Ω_{N2} (nm^2)	Ω_{He} (nm^2)	R_h (nm)
Glycosylated			
parent mAb	76.2 ± 0.8	70.32 ± 0.28	5.06 ± 0.1
mAb + 30 eqv. biotin	77.8 ± 1.0	71.66 ± 0.48	5.10 ± 0.1
Deglycosylated			
parent mAb	75.0 ± 0.7	69.34 ± 0.57	5.04 ± 0.1
mAb + 30 eqv. biotin	76.2 ± 0.6	71.17 ± 0.23	5.13 ± 0.1

a. CCS values are averaged from all charge states.

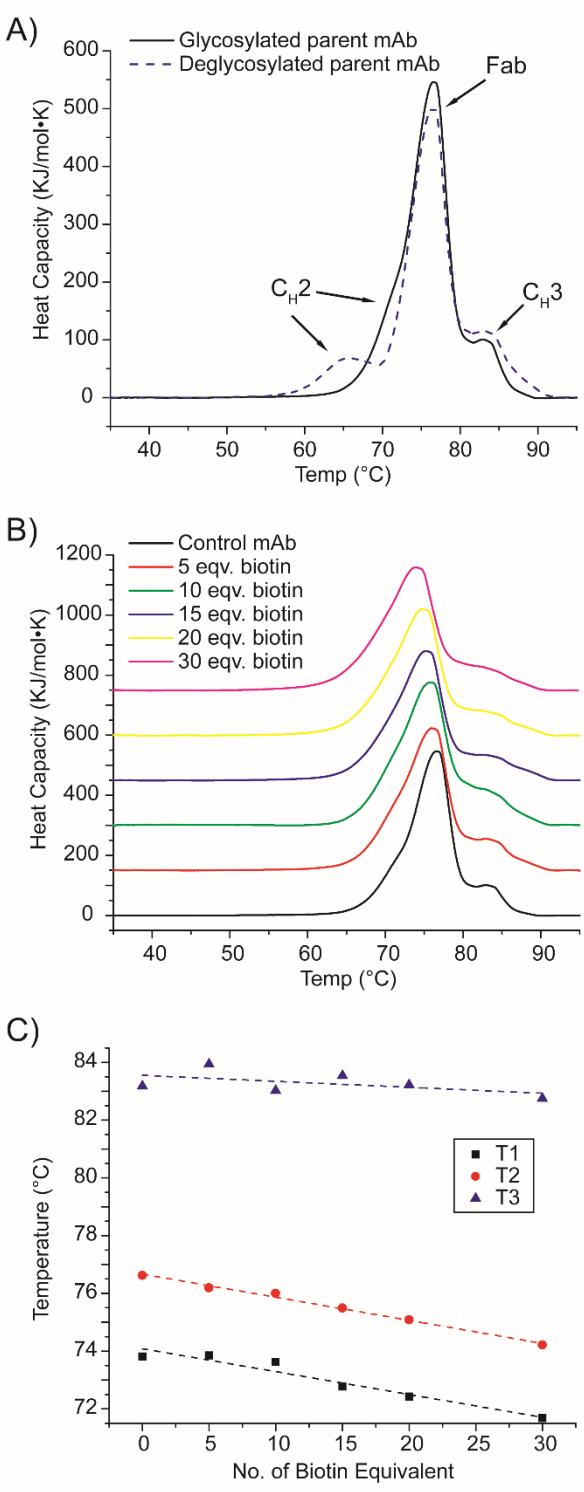

Figure 4-3. (A) Overlay of the baseline subtracted DSC thermograms recorded for the control mAbs with or without N-linked glycosylation. (B) Overlay of the baseline subtracted DSC thermograms for the biotinylated mAbs with N-linked glycosylation. (C) The transition temperatures extracted from the DSC thermograms plotted as a function of biotin equivalents reacted with the mAb.

Thermal stabilities of IgG1-biotin conjugates in solution

In order to evaluate the thermal stabilities of our ADC models in solution, we utilized DSC to record melt temperatures for glycosylated and deglycosylated mAbs in the absence of biotinylation. As shown in Figure 4-3A, we detect a shift in the first mAb transition temperature, with the other two transition temperatures remaining essentially unchanged. Specifically, the first melt temperature we observe is apparently decreased from 73.8 °C to 67.5 °C upon deglycosylation, indicating altered C_H2 domain structure upon glycan removal, in line with previous literature reports.[38,39]

Following these control experiments, we further compared DSC results acquired for ADC models prepared using a range of biotin equivalents with those acquired for the parent mAb.(Figure 4-3B) While

biotinylated mAbs also unfold to produce three distinct melting transitions, we observe differences in their absolute values that are correlated with expected levels of biotinylation for these samples. We observe a linear decrease in Fab melt temperature as a greater number of biotins are conjugated to the target mAb, shifting from 76.6 °C to 74.2 °C, whereas the unfolding temperature we observe for the C_H2 domain remains unchanged at ~73.8 °C until more than 15 equivalents of biotins are used for the conjugation reaction. For deglycosylated ADC models, the observed melt temperatures also shift as greater numbers of biotins are conjugated.(Figure III-2) In contrast to glycosylated mAbs, the higher-temperature transitions shift to lower temperatures as a function of biotinylation for our deglycosylated ADC models. Overall, it is interesting to note that biotinylated mAbs are destabilized upon biotin conjugation. Despite this, the level of destabilization we detect is minimal and only detectable by DSC with confidence when comparing mAbs conjugated with greater than 15 biotin equivalents.

CIU fingerprints reveal significant stability shifts upon biotin conjugation

As our native IM-MS and classical DSC exhibited poor sensitivities to biotin conjugation within IgG1 mAbs, we performed CIU analysis in an effort to capture structure and stability changes in our ADC mimics that remain too subtle to detect using other approaches. Figure 4-4A-F shows averaged CIU fingerprints for the 25+ mAb ions reacted with 0 to 30 equivalents of biotin. We observe three unfolded features for the parent IgG1 mAb in addition to its ground state conformer family, with centroid IM drift times ranging from ~7.7 ms to ~12.6 ms. These same intermediate states are observed throughout our 25+ ADC model CIU dataset. While CIU data recorded for each biotinylated mAb appears similar to control experiments, detailed quantitative analysis of the complete fingerprints recorded reveal shifts in mAb stability that are highly correlated with the extent of expected protein conjugation.

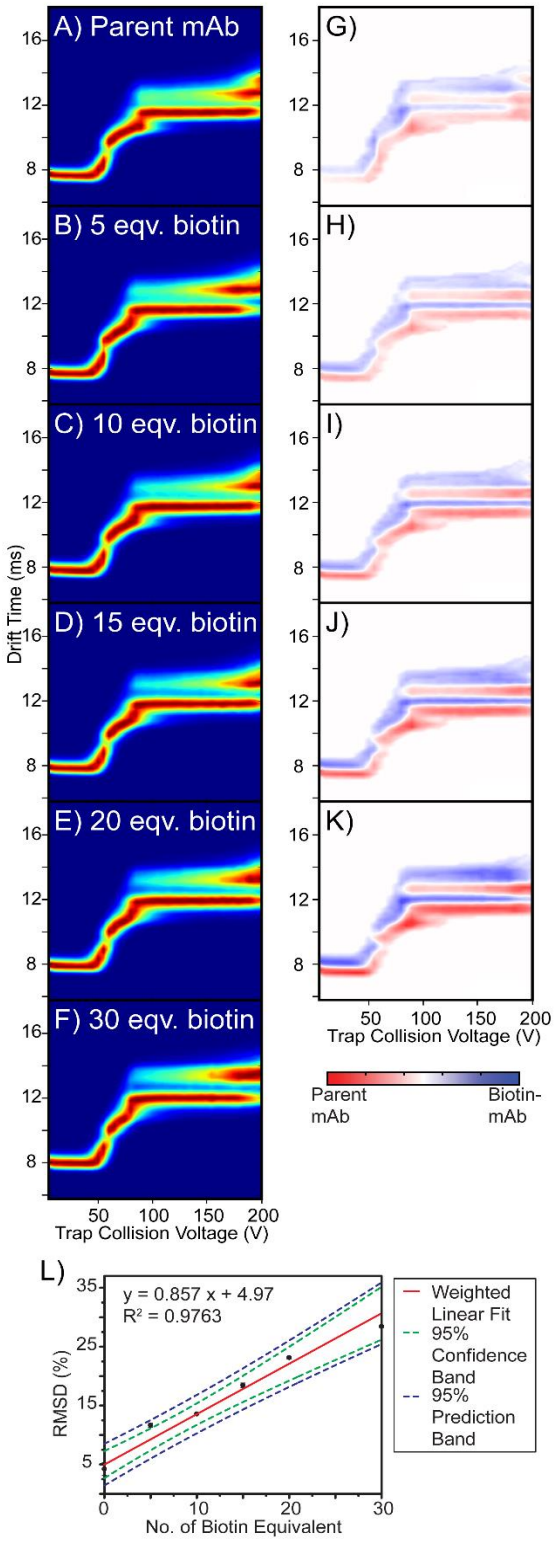

Figure 4-4. (A-F) Triplicate averaged CIU fingerprints for the parent mAb and the IgG1-biotin conjugates. (G-K) CIU difference plots generated by subtracting the fingerprint of the biotinylated mAb from that of the parent mAb. (L) RMSD values plot as a function of biotin equivalent used in the conjugation reactions. Each data point represents the average value from triplicate, with the standard deviation shown as the error bar. A weighted linear regression was performed for data fitting (red line).95% confidence interval (green dashed line) and 95% prediction interval (blue dashed line) were computed.

To perform the abovementioned quantitative analysis of our CIU data, we generated a series of difference plots by comparing averaged CIU fingerprints for ADC model state with that of the parent mAb. (Figure 4-4G-K) A color scale is used to denote the magnitude of the differences in signal intensities detected for each comparison, with deeper colors representing the greater signals detected for either the dominated parent mAb (red) or the selected ADC mimic (blue). As shown in Figure 4-4G-K, the minor differences observed in our ground state CCS values are carried forward across all voltages probed in our experiment. To quantify the sensitivity of our CIU analysis to small changes in mAb conjugation state, we plot total RMSD values, extracted from pixel-by-pixel comparisons between CIU fingerprints acquired for ADC models and control mAbs, where larger RMSD values suggest the higher degrees of dissimilarity between the two CIU fingerprints. We observe that the CIU RMSD and the number of biotin equivalents used for the conjugation reaction are strongly correlated to a linear function, with a sufficiently steep slope and narrow error bars so that quantification of stability shifts produced through eight biotin equivalents during mAb conjugation is possible with high confidence.(Figure 4-4L) Importantly, using CIU RMSD analysis, we are able to globally quantify the structural differences between the biotinylated mAbs versus their parent mAb, even in cases where only small numbers of biotin have been bound.

CIU width and stability analyses further differentiate conjugated mAbs

In an effort to further differentiate ADC samples using CIU, we chose to perform comprehensive analyses that track shifts in TWIM peak widths and stabilities observed in our CIU fingerprints. The width of the arrival time distribution (ATD) recorded in an IM separation is attributable to multiple factors including ion diffusion, the length of the initial ion pulse, space charge, reaction chemistry, and any conformational heterogeneity that manifests on a timescale faster than the IM separation.[40–43] Most IM experiments are designed to minimize peak width influencers other than

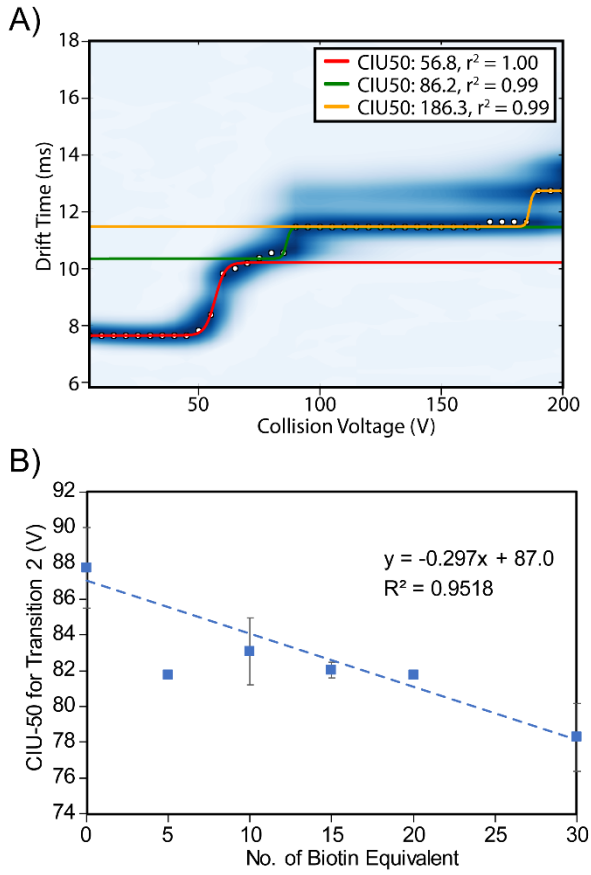

Figure 4-5. (A) A representative CIU fingerprint for the parent mAb with three gas-phase unfolding transitions fitted. Our analysis is focused on the first two transitions, highlighted as red and green lines respectively. (B) Collision voltage required for the second CIU transition plotted against the number of biotin equivalent. Each data point is the average value from triplicate data. An initial linear regression was performed and the studentized deleted residuals (r_i) were calculated to detect outliers. Data point for 5 eqv. biotin was identified as an outlier, as $|r| = 3.732 > t_{0.975\,(df=3)}$. The trendline shown in this figure was fitted based on the dataset omitting the outlier.

those associated with diffusional and conformational broadening. As such, if one assumes that diffusional broadening will be roughly equivalent for all mAb species studied here, dramatic changes in the full width at half-maximum (FWHM) of the TWIM ATDs result from differences in mAb flexibility and structural polydispersity.

To pursue a TWIM width analysis for our ADC CIU datasets, we utilized multi-modal Gaussian fitting to analyze IM datasets acquired for all mAb samples at each collision voltage recorded. Centroid drift time (DT) and FWHM values for each fitted Gaussian distribution were determined and plotted as a function of trap collision voltage (Figure III-3). As shown in Figure III-3A, and discussed above, all six mAbs exhibit nearly identical ground state drift time values, with the minor CCS differences observed likely attributable to the extra mass associated with biotinylation. For example, the centroid value for maximally conjugated mAb ATDs recorded prior to activation is at ~0.33 ms longer DT when compared with control mAb data, representing a 4% increase. Such relatively minor differences,

however, are amplified during CIU, producing differences in TWIM ATD centroids as large as 6% for extended mAb states populated at higher activation voltages.

Figure III-3B compares the TWIM widths recorded for ADC models with those observed for the parent mAb. Highly similar FWHM values are observed for the ground state arrival time distributions at collision voltages lower than 40V, suggesting that ADC mimics comprise structures with similar degrees native flexibility and heterogeneity. We detect significantly increased FWHM values at collision voltages between 50 and 70V, corresponding with the initial CIU transition observed. Furthermore, the TWIM width analysis at higher voltages indicate that different levels of structural heterogeneity appear in the unfolding intermediates populated during CIU of the biotinylated mAbs studied here. Taking the IM data collected at collision voltage of 180V as an example, two states are observed, with the state at longer drift time exhibiting FWHM and IM resolution trends that are highly correlated with the amount of biotin used during conjugation. Conversely, the IM width and resolution of the state that appears at shorter drift time exhibit opposite trends with biotinylation. (Figure III-3D, E) The correlation detected in the width analysis serves as a partial explanation for the discrimination observed through the RMSD analysis shown in Figure 4-4L, which is clearly governed by the accumulated differences in the CIU response across the whole activation range.

To further mine our ADC CIU data for quantitative differences associated with biotin conjugation, we performed a CIU-50 analysis to track the activation voltages at which half of the ion population transitions from one CIU conformer state to another. Two major CIU transitions were examined in our analysis: the initial transition that occurs at voltages around 57 V, and a higher-energy transition that appears at collision voltages between 78.3V and 87.8V showing apparent correlations. (Table III-2) For example, Figure 4-5 illustrates that while an averaged collision

voltage of 87.8 V is required to transition half of the control mAb population from the first CIU intermediate observed to the second, progressively lesser voltages are needed to achieve this unfolding transition as mAb conjugation increases in a linear fashion. Although this trend is a long way from ideal and can be less obvious for different batches of samples (Figure III-3F), it is the first time that we observe a trend in the gas-phase unfolding energies that is similar to the correlation observed in the melt temperatures measured by DSC. This relationship strongly suggests that future CIU data for similar systems may be used to estimate mAb melt temperatures in solution.

4.4 Conclusions

This work presents a thorough structural characterization of ADC models using a battery of techniques, including denaturing LC-MS, DSC, SEC, native IM-MS and CIU analysis. Our data suggests that DAR values for these IgG1-biotin conjugates can be estimated based on their average intact masses measured by a Q-ToF mass spectrometer under native conditions, but that native MS remains relatively insensitive to small change in biotin conjugation level. Similarly, though IM measurements performed on native like ions, DSC measurements, and SEC data all reveal trends that indicative of local changes in mAb structure upon biotinylation that ultimately reduce the stabilities of the resultant ADC models. In contrast, however, CIU data demonstrate the ability to detect stability shifts associated with small numbers of bound biotin, while mirroring the structural trends observed in other, lower throughput data types. As such, our data strongly indicates that CIU has a synergistic role to play in ADC development efforts, by providing a means to acquire conjugation-dependent gas-phase stability shift information in a manner that is maximally sensitive to small changes to the target therapeutic.

Our CIU analysis includes RMSD, CIU-50, and peak width values, all of which are able to individually discriminate between ADC mimics. This report represents the first example of such multi-parameter CIU data analysis and presents exciting possibilities for future software development efforts. Interestingly, an analysis of CIU-50 from our data reveals mAb gas-phase stability values that decrease in a fashion similar to what is observed for these same samples by DSC. While this correlation is far from perfect, it presents the first evidence of such a relationship between CIU and DSC data, as well as further experimental evidence indicating strong solution-phase memory effects for large gas-phase protein ions.

Clearly, through continued efforts in method and data interpretation procedures, IM-MS and CIU data will serve to dramatically enhance our understanding of the structures of mAb related drug products, as well as drive future discovery and development efforts.

4.5 Supporting Information

Supporting information can be found in the Appendix III.

4.6 Acknowledgement

This work is a collaborative project with Amgen. Dr. Chawita (Jelly) Netirojjanakul prepared the mAb-biotin conjugates, Dr. Jennifer Lippens collected the denaturing LC-MS data, and Dr. Iain Campuzano performed the SEC-MALS-QELS and drift tube IM measurements.

4.7 References

(1) Chari, R. V. J.; Miller, M. L.; Widdison, W. C. *Angew. Chem. Int. Ed. Engl.* **2014**, *53* (15), 3796–3827.
(2) Lambert, J. M.; Morris, C. Q. *Adv. Ther.* **2017**, *34* (5), 1015–1035.
(3) Beck, A.; Goetsch, L.; Dumontet, C.; Corvaïa, N. *Nat. Rev. Drug Discov.* **2017**, *10* (5), 345–352.
(4) Diamantis, N.; Banerji, U. *Br. J. Cancer* **2016**, *114* (4), 362–367.
(5) Panowski, S.; Bhakta, S.; Raab, H.; Polakis, P.; Junutula, J. R. *MAbs* **2014**, *6* (1), 34–45.

(6) Hamblett, K. J.; Senter, P. D.; Chace, D. F.; Sun, M. M. C.; Lenox, J.; Cerveny, C. G.; Kissler, K. M.; Bernhardt, S. X.; Kopcha, A. K.; Zabinski, R. F.; Meyer, D. L.; Francisco, J. A. *Clin. Cancer Res.* **2004**, *10* (20), 7063–7070.
(7) Valliere-Douglass, J. F.; Hengel, S. M.; Pan, L. Y. *Mol. Pharm.* **2015**, *12* (6), 1774–1783.
(8) Redman, E. A.; Mellors, J. S.; Starkey, J. A.; Ramsey, J. M. *Anal. Chem.* **2016**, *88* (4), 2220–2226.
(9) Kim, M. T.; Chen, Y.; Marhoul, J.; Jacobson, F. *Bioconjug. Chem.* **2014**, *25* (7), 1223–1232.
(10) Luo, Q.; Chung, H. H.; Borths, C.; Janson, M.; Wen, J.; Joubert, M. K.; Wypych, J. *Anal. Chem.* **2016**, *88* (1), 695–702.
(11) Ouyang, J. Humana Press, Totowa, NJ, 2013; pp 275–283.
(12) Bobály, B.; Fleury-Souverain, S.; Beck, A.; Veuthey, J.-L.; Guillarme, D.; Fekete, S. *J. Pharm. Biomed. Anal.* **2018**, *147*, 493–505.
(13) Lazar, A. C.; Wang, L.; Blättler, W. a; Amphlett, G.; Lambert, J. M.; Zhang, W. *Rapid Commun. Mass Spectrom.* **2005**, *19* (13), 1806–1814.
(14) Wakankar, A.; Chen, Y.; Gokarn, Y.; Jacobson, F. S. *MAbs* **2011**, *3* (2), 161–172.
(15) Debaene, F.; Bœuf, A.; Wagner-Rousset, E.; Colas, O.; Ayoub, D.; Corvaïa, N.; Van Dorsselaer, A.; Beck, A.; Cianférani, S. *Anal. Chem.* **2014**, *86* (21), 10674–10683.
(16) Hengel, S. M.; Sanderson, R.; Valliere-Douglass, J.; Nicholas, N.; Leiske, C.; Alley, S. C. *Anal. Chem.* **2014**, *86* (7), 3420–3425.
(17) Valliere-Douglass, J. F.; McFee, W. A.; Salas-Solano, O. *Anal. Chem.* **2012**, *84* (6), 2843–2849.
(18) Rose, R. J.; Damoc, E.; Denisov, E.; Makarov, A.; Heck, A. J. R. *Nat. Methods* **2012**, *9* (11), 1084–1086.
(19) Belov, M. E.; Damoc, E.; Denisov, E.; Compton, P. D.; Horning, S.; Makarov, A. A.; Kelleher, N. L. *Anal. Chem.* **2013**, *85* (23), 11163–11173.
(20) Dyachenko, A.; Wang, G.; Belov, M.; Makarov, A.; de Jong, R. N.; van den Bremer, E. T. J.; Parren, P. W. H. I.; Heck, A. J. R. *Anal. Chem.* **2015**, *87* (12), 6095–6102.
(21) Yang, Y.; Wang, G.; Song, T.; Lebrilla, C. B.; Heck, A. J. R. *MAbs* **2017**, *9* (4), 638–645.
(22) Campuzano, I. D. G.; Netirojjanakul, C.; Nshanian, M.; Lippens, J. L.; Kilgour, D. P. A.; Van Orden, S.; Loo, J. A. *Anal. Chem.* **2018**, *90* (1), 745–751.
(23) Acchione, M.; Kwon, H.; Jochheim, C. M.; Atkins, W. M. *MAbs* **2012**, *4* (3), 362–372.
(24) Wakankar, A. A.; Feeney, M. B.; Rivera, J.; Chen, Y.; Kim, M.; Sharma, V. K.; Wang, Y. J. *Bioconjug. Chem.* **2010**, *21* (9), 1588–1595.
(25) Pan, L. Y.; Salas-Solano, O.; Valliere-Douglass, J. F. *Anal. Chem.* **2014**, *86* (5), 2657–2664.
(26) Pacholarz, K. J.; Porrini, M.; Garlish, R. a; Burnley, R. J.; Taylor, R. J.; Henry, A. J.; Barran, P. E. *Angew. Chem. Int. Ed. Engl.* **2014**, *53* (30), 7765–7769.
(27) Campuzano, I. D. G.; Larriba, C.; Bagal, D.; Schnier, P. D. In *ACS Symposium Series*; 2015; Vol. 1202, pp 75–112.
(28) Ehkirch, A.; D'Atri, V.; Rouviere, F.; Hernandez-Alba, O.; Goyon, A.; Colas, O.; Sarrut, M.; Beck, A.; Guillarme, D.; Heinisch, S.; Cianferani, S. *Anal. Chem.* **2018**, acs.analchem.7b02110.
(29) Dixit, S. M.; Polasky, D. A.; Ruotolo, B. T. *Curr. Opin. Chem. Biol.* **2018**, *42*, 93–100.
(30) Tian, Y.; Han, L.; Buckner, A. C.; Ruotolo, B. T. *Anal. Chem.* **2015**, *87* (22), 11509–11515.

(31) Tian, Y.; Ruotolo, B. T. *Int. J. Mass Spectrom.* **2018**, *425*, 1–9.
(32) Pisupati, K.; Tian, Y.; Okbazghi, S.; Benet, A.; Ackermann, R.; Ford, M.; Saveliev, S.; Hosfield, C. M.; Urh, M.; Carlson, E.; Becker, C.; Tolbert, T. J.; Schwendeman, S. P.; Ruotolo, B. T.; Schwendeman, A. *Anal. Chem.* **2017**, *89* (9), 4838–4846.
(33) Ferguson, C. N.; Gucinski-Ruth, A. C. *J. Am. Soc. Mass Spectrom.* **2016**.
(34) Botzanowski, T.; Erb, S.; Hernandez-Alba, O.; Ehkirch, A.; Colas, O.; Wagner-Rousset, E.; Rabuka, D.; Beck, A.; Drake, P. M.; Cianférani, S. *MAbs* **2017**, *9* (5), 801–811.
(35) Haynes, S. E.; Polasky, D. A.; Dixit, S. M.; Majmudar, J. D.; Neeson, K.; Ruotolo, B. T.; Martin, B. R. *Anal. Chem.* **2017**, acs.analchem.7b00112.
(36) Eschweiler, J. D.; Rabuck-Gibbons, J. N.; Tian, Y.; Ruotolo, B. T. *Anal. Chem.* **2015**, *87* (22), 11516–11522.
(37) Hewitt, D.; Marklund, E.; Scott, D. J.; Robinson, C. V; Borysik, A. J. *J. Phys. Chem. B* **2014**, *118*, 51.
(38) Zheng, K.; Bantog, C.; Bayer, R. *MAbs* **2011**, *3* (6), 568–576.
(39) Pawlowski, J. W.; Bajardi-Taccioli, A.; Houde, D.; Feschenko, M.; Carlage, T.; Kaltashov, I. A. *J. Pharm. Biomed. Anal.* **2018**, *151*, 133–144.
(40) Wu, C.; Siems, W. F.; Asbury, G. R.; Hill, H. H. *Anal. Chem.* **1998**, *70* (23), 4929–4938.
(41) Wyttenbach, T.; von Helden, G.; Bowers, M. T. *J. Am. Chem. Soc.* **1996**, *118* (35), 8355–8364.
(42) Shvartsburg, a a; Smith, R. D. *Anal. Chem.* **2008**, *80* (24), 9689–9699.
(43) Zhong, Y.; Hyung, S.-J.; Ruotolo, B. T. *Analyst* **2011**, *136* (17), 3534–3541.

Chapter 5. Integrating IM-MS and CIU into Multiple Attribute Monitoring Workflow for Comparison of Remicade and the Biosimilar Remsima

This chapter includes elements from two published papers:

Karthik Pisupati, **Yuwei Tian**, Solomon Okbazghi, Alexander Benet, Rose Ackermann, Michael Ford, Sergei Saveliev, Christopher M. Hosfield, Marjeta Urh, Eric Carlson, Christopher Becker, Thomas J. Tolbert, Steven P. Schwendeman, Brandon T. Ruotolo and Anna Schwendeman, *Anal. Chem.*, 2017, **89**, 4838–4846. (DOI: 10.1021/acs.analchem.6b04436)

Karthik Pisupati, Alexander Benet, **Yuwei Tian**, Solomon Okbazghi, Jukyung Kang, Michael Ford, Sergei Saveliev, K. Ilker Sen, Eric Carlson, Thomas J. Tolbert, Brandon T. Ruotolo, Steven P. Schwendeman and Anna Schwendeman, *MAbs*, 2017, **9**, 1197–1209. (DOI: 10.1080/19420862.2017.1347741)

Abstract

Remsima became the first biosimilar monoclonal antibody (mAb) approved by the Food and Drug Administration (FDA) in April 2016. With the expired or expiring patents of currently marketed therapeutic mAbs, biosimilars promise significant cost savings for patients. However, the unavoidable differences between the innovator and copycat biologics raise questions regarding product interchangeability. In this study, Remicade and Remsima were examined by native ion mobility-mass spectrometry (IM-MS), gas-phase unfolding, along with the quantitative peptide mapping. The primary structures were identical, and the major modifications and higher order structures were remarkably similar. We found different levels of C-terminal truncation, soluble protein aggregates, and glycation that all likely have a limited clinical impact. Importantly, we identified more than 25 glycoforms for each product and observed glycoform population

differences, with afucosylated glycans accounting for 19.7% of Remicade and 13.2% of Remsima glycoforms, which translated into a 2-fold reduction in the level of FcγIIIa receptor binding for Remsima. In addition, we studied the stability and aggregation mechanisms of these two mAb products under stress conditions. Despite small initial differences, both products formed the degradation products at similar rates and to the similar abundances in the forced degradation study. Our mass spectrometry-based analysis provides rapid and robust analytical information vital for biosimilar development. We have demonstrated the utility of our multiple attribute monitoring (MAM) workflow using the model mAbs Remicade and Remsima and have provided a template for analysis of future mAb biosimilars.

5.1 Introduction

Following expiry of patents and other exclusively rights that protect many top-selling mAbs, the market may open to the generic or biosimilar versions of these mAbs.[1] Biosimilars are expected to be less expensive and more affordable for patients owing to the lower cost in the research and development.[2,3] In contrast to generic small molecule drugs, it is not possible to produce biosimilar mAbs identical to their template innovator products. By nature, the recombinant manufacturing processes yield heterogeneous products of variants exhibiting differences in glycosylation, oxidation, deamidation, glycation, and aggregation state. The inherent heterogeneity could potentially affect the quality, safety and potency of the biosimilars. Therefore, rigorous analytical characterization of such heterogeneity in the biosimilar product, as well as comparisons to the heterogeneity of the innovator product, is critical for ensuring a similar level of safety and efficacy of the two products. Regulatory agencies have provided guidance on analytical studies to assess the whether the biosimilar product is highly similar to the originator, as part of biosimilarity assessment.[4–7] FDA recommends a stepwise approach for the manufacturer to demonstrate the

biosimilarity and the "totality-of-evidence" approach is emphasized for assessing the demonstration of biosimilarity.[7] The extensive characterization of the proposed biosimilar and the reference products is expected to be performed with the state-of-the-art technologies. First, the primary structure and higher order structures, as well as other critical quality attributes (CQAs) of mAb, e.g., oxidation, glycosylation profiles, glycation, and the amount of aggregation, need to be characterized using appropriate analytical techniques. Then, the structural assessments are combined with functional studies such as bioactivity and receptor binding assays to evaluate whether the biosimilar is highly similar to the reference product. On the basis of these analytical characterization, the role of animal toxicity studies and human clinical studies is determined.[8] Thus, unequivocally showing complete analytical comparability of the biosimilar to the reference product could result in shrinking the scope of clinical studies.[8,9] Hence, biosimilar developers are incentivized to perform complete analytical comparisons of CQA for their own and innovator products using state-of-the art methodologies.

Infliximab, or Remicade (RC), was developed by Janssen and approved in 1998. Remicade was one of the first therapies to target tumor necrosis factor α (TNFα), and its annual sales exceeded $9 billion worldwide in 2014. However, patent exclusivity for infliximab has since expired, and the first infliximab biosimilar, Remsima (RS), was approved in Europe in 2013 and more recently in the United States in 2016. Remsima, also known as Inflectra or CTP-13, was developed and manufactured by Celltrion and licensed to Hospira/Pfizer.[10] Given the approval status of Remsima, the extensive data package that was submitted for regulatory approval effectively proved the two antibodies were similar, yet not identical. Despite the identical amino acid sequences of the two products, the levels of charged variant species attributed to C-terminal truncation and dimer levels were reported and ultimately deemed nonconsequential.[11–13] Both RC and RS contain a

heterogeneous mixture of N-glycans that, when analyzed by orthogonal methods, were assessed overall to be similar, as evidenced in a recent publication by the manufacturer of RS.[14] However, released regulatory documentation acknowledged apparent differences in RS glycosylation, specifically, in the levels of fucosylated glycans, and how this difference affected FcγIIIa receptor (FcγRIIIa) binding and antibody-dependent cell-mediated cytotoxicity (ADCC).[11–13] Mediating ADCC is not thought to be a key component of infliximab's efficacy in the treatment of rheumatologic diseases (e.g., RA or AS) but it is presumed to be partially responsible for its activity in inflammatory bowel disease (IBD) through the modulation of local immune cell populations.[11,12,15] Because of glycosylation and ADCC differences, the Canadian regulatory agency did not approve the use of RS for treatment of IBD and requested additional clinical data for the IBD patients.[15]

As more biosimilar mAbs gain regulatory approval, it is important that a clear framework for a rapid characterization of innovator and biosimilar products exists that could identify clinically relevant differences. Mass spectrometry combined with liquid chromatography is a corner stone for the comparability and biosimilarity assessments, especially in comparing primary structure and PTMs via bottom-up MS analysis. Recently, MS coupled with techniques, such as ion mobility (IM) separation[16] and hydrogen/deuterium exchange (HDX),[17] has also been deployed in probing the higher order structures of proteins. And IM-MS has been demonstrated useful for comparative analysis of therapeutic antibodies.[18] In this study, we applied a comprehensive mass spectrometry (MS)-based strategy using bottom-up, middle-down, and intact strategies. IM-MS and CIU analyses were integrated with bottom-up MS results, as well as data from select biophysical techniques and receptor binding assays to comprehensively evaluate biosimilarity of these two infliximab products. Moreover, since the minor structural differences may by amplified under

stress, we performed native IM-MS measurements on the force degradation products to further the similarity evaluation of these two products. Our ultimate goal was to develop a template that can be applied toward future analytical comparisons of biosimilar mAbs.

5.2 Materials and Methods

Materials

Eight lots of the chimeric antibody infliximab were purchased: four lots of RC and four lots of RS. Both products are supplied as lyophilized powder of identical composition (infliximab, sucrose, sodium phosphate, and polysorbate 80). All samples were reconstituted using pure water for injection (Thermo-HyClone WFI) to a concentration of 1 mg/mL unless specified otherwise.

Enzymatic Digestion

IdeS Digest. Samples were digested with IdeS enzyme (Genovis) to generate Fab and Fc fragments according to the manufacturer's protocol. Briefly, ~1 mg/mL antibody, in 0.55 mM sodium phosphate buffer (pH 7.2), was mixed with enzyme at a ratio of 1 μg of protein per unit of enzyme. The mixture was incubated at 37 °C for 3–4 h to ensure maximal cleavage and the reaction quenched with ice prior to analysis.

Deglycosylation and Reduction. Deglycosylated mAb samples for native IM-MS analysis were prepared without reduction by incubating 10 μL of ~1 mg/mL intact or IdeS-digested mAb sample with 2 μL of PNGase F (glycerol-free, New England Biolabs) in a total reaction volume of 22 μL under native buffer conditions overnight at 37 °C.

Protein stress setup

Powders of Remicade® and Remsima™ contain ~16% of protein by weight. Vials of both products were opened and aliquoted in 1.5 mL Eppendorf tubes (~6.25 mg of powder or 1 mg of infliximab in each tube). Saturated solutions of NaBr and K_2SO_4 in distilled water were prepared to simulate 53% and 97% RH, respectively.[19] Desiccant was used to simulate dry conditions. The infliximab powders in open tubes were placed in desiccators at a specific RH and incubated at 40°C for 1, 2, or 4 weeks. Samples were removed from the desiccators and reconstituted with WFI to 1 mg/mL. Reconstituted samples were further aliquoted for the various analytical assays and stored at either 4°C or −80°C until analysis.

Ion Mobility-Mass Spectrometry and Collision-Induced Unfolding

Reconstituted antibody samples were dialyzed with 100 mM ammonium acetate using Micro Bio-Spin 30 columns (Bio-Rad, Hercules, CA). Sample aliquots (~7 μL) were analyzed by IM-MS on a quadrupole ion mobility time-of-flight mass spectrometry (Q-IM-ToF MS) instrument (Synapt G2 HDMS, Waters, Milford, MA).[20,21] Samples were analyzed in triplicate for each lot. Antibody ions were generated using a nESI source in the positive mode. Capillary voltages of 1.4–1.6 kV were applied, and the sampling cone was operated at 60 V. The trap traveling-wave ion guide was pressurized to 3.4×10^{-2} mbar of argon gas. The traveling-wave ion mobility separator was operated at a pressure of ~2.5 mbar and employed a series of DC voltage waves (40 V wave height traveling at 600 m/s) to generate ion mobility separation. The ToF-MS instrument was operated over the range of 1000−10000 *m*/*z* at a pressure of 1.7×10^{-6} mbar.

CIU experiments were performed on a Waters Synapt G2 HDMS instrument as previously described.[22] The 23^+ charge state of the intact mAb was first selected by tandem MS using a quadrupole mass filter. Collision energy was then added to successive packets of stored, selected ions prior to IM separation. The collision voltage, defined as the accelerating potential between

the end of the quadrupole mass filter and the beginning of the pre-IM ion trap, was ramped from 5 to 200 V in 5 V increments to construct the fingerprint data shown in this report. IM data were recorded for MS-isolated ions at each collision voltage, and the IM data for only those ions corresponding the intact *m*/*z* originally isolated ions were compiled to create the plots and quantitative comparisons that are shown here.

IM-MS and CIU Data Analysis

Mass spectra were calibrated externally using a solution of cesium iodide (100 mg/mL) and processed with Masslynx version 4.1 (Waters). Exact molecular masses of intact mAb and IdeS-digested mAb samples were calculated by assigning the charge states on the basis of the set that gives the smallest standard deviation for a given average mass assignment.[23]

Drift time data were extracted at each collision voltage in Drift Scope (Waters). Extracted CIU data were analyzed using CIUSuite.[24] CIU "fingerprint" data were plotted as a two-dimensional contour plot using the CIUSuite_gen module. The color scale in these plots indicates the signal intensities recorded that were normalized to a maximal value of 1 at each collision voltage and smoothed using a Savitzky–Golay filter. Statistical analysis of CIU data sets was conducted using the CIUSuite_stats function, in which average CIU fingerprints and standard deviation plots were generated for multiple lots of RC and RS samples.

Statistical Analysis

Unless specified otherwise, statistics were determined using Prism 6 (GraphPad). Unpaired *t* tests were performed without assuming a consistent standard deviation. Statistical significance was determined using the Sidak–Bonferroni method, with $\alpha = 5.0\%$.

Details on LC-MS, SEC, and BLI experiments can be found in Appendix IV.

5.3 Results and Discussion

Four lots of each product were procured and analyzed within the expiry period. The number of lots analyzed in this study was lower than typically used for biosimilar regulatory filing. For example, the data for 26 lots of RS and 36 lots of RC were presented by Celltrion in the FDA briefing document, although some assays were performed on as few as three lots for each product.[11–13,25] The methodologies used in this study, quality attributes measured, key findings, and some advantages of using MAM quantitative mass spectrometry are summarized in Table 5-1.

Table 5-1. Analytical Methodologies Used to Compare Remicade and Remsima

analytical method	sample processing	measured attributes	method advantages
native MS, IM-MS	buffer exchange, deglycosylation, IdeS digest	intact mass, fragments, aggregation, glycation, higher-order structure, gas phase stability	limited sample preparation, rapid analysis, low detection limit, high information content
denaturing MS	deglycosylation and reduction	intact masses of subunits, C-terminal Lys truncation	information about accurate subunit mass and heterogeneity
peptide mapping	trypsin digest	sequence, mutations, oxidations, deamidations, glycosylation	single analysis allows for identification and quantification of multiple attributes
	Glu-C digest	glycations	
size exclusion chromatography	none	level of aggregation	not applicable
biolayer interferometry	buffer exchange	Fc receptor binding K_D	not applicable

Intact mAbs were first analyzed by IM-MS under native conditions, using only minimal preparation of the as-produced therapeutic samples. Relatively weak electric fields are used to separate gas phase protein ions according to their orientationally averaged collision cross sections

(CCSs) and charge. RC and RS had similar IM drift times with discrete positions in drift time versus *m*/*z* space for antibody fragments, monomers, and dimers (Figure 5-1A, B). The extracted arrival time distributions were nearly identical for the two mAb monomers, indicating that they possess highly similar gas-phase structures. The intact masses recorded for glycosylated and deglycosylated mAbs were indistinguishable within our experimental error, 149382 ± 222 Da and 146066 ± 38 Da for RC, and 149695 ± 372 Da and 146076 ± 51 Da for RS, respectively. Low levels of misassembled heavy chains (HCs) and light chains (LCs), resulting in mAb impurities, were found in both products: LC_2 or HC, 2.34 ± 0.57% (RC) and 0.09 ± 0.13% (RS) ($p < 0.001$); HC_2, 0.83 ± 0.10% (RC) and 1.36 ± 0.25% (RS) ($p < 0.2$); HC-LC, 0.09 ± 0.13% (RC) and 0.88 ± 0.32% (RS) ($p < 0.1$). The presence of misassembled species was also acknowledged in the regulatory filings for RS, with the intact H_2L_2 being 98.2% (RC) and 95.1% (RS) as measured by capillary electrophoresis.[11,13] The identical sequences of the two mAbs were then confirmed by bottom-up LC–MS analysis with >98% coverage. Similar levels of sequence variants, oxidation and deamidation were found in both products, further suggesting their remarkable similarities. (Figure IV-1)

We further compared the higher-order structures of these two mAbs using CIU. Collisional activation in the gas phase is performed to generate partially unfolded mAb states, which are subsequently separated by IM and then analyzed by MS. The “Fingerprint” plots are created to track the amount of protein unfolding as a function of collisional energy applied, and the unfolding patterns that develop have proven to be highly sensitive to small variations in protein structure that

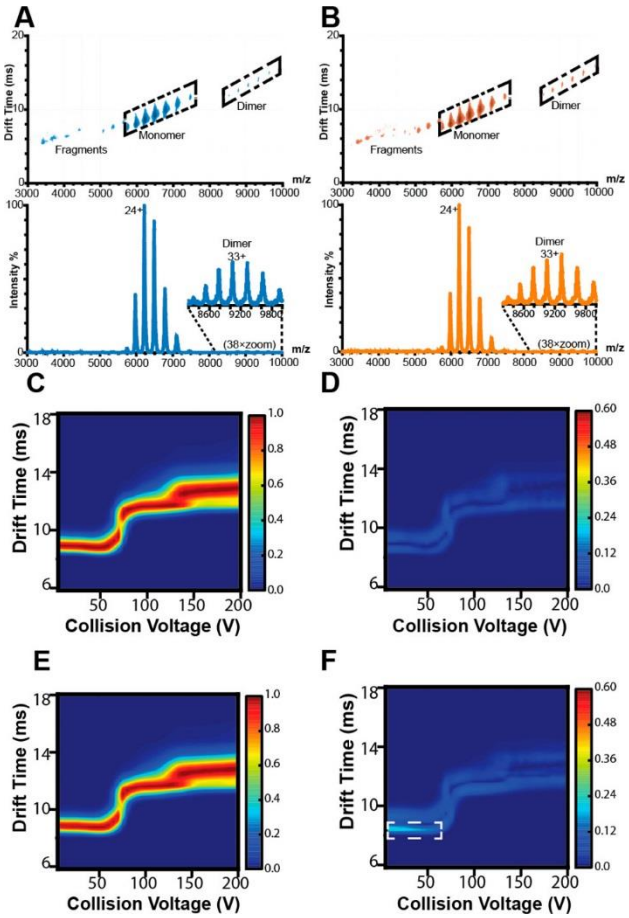

Figure 5-1. Ion mobility mass spectrometry of Remicade and Remsima. Representative IM-MS spectra of (A) RC and (B) RS with annotated fragment, monomer, and dimer species. Average collision-induced unfolding (CIU) fingerprints of (C) RC and (E) RS and standard deviations of (D) RC and (F) RS CIU fingerprints (n = 4 lots).

cannot be easily resolved by IM alone.[21,26–29] These fingerprints have been used to rapidly distinguish between antibody isoforms, sensitive to differences in both glycosylation and disulfide bonding.[22,30] An initial CIU analysis of RC and RS revealed remarkably similar structures and, for the first time, quantitatively compared their gas phase unfolding. The CIU fingerprints of mAb 23+ charge state exhibit the highest degree of similarity at high collision voltages, and the overall variance between RC and RS CIU fingerprints is comparable to levels reported for replicates of the mAb reference standard.[22] Both mAbs unfold in the gas phase to produce two unfolded states from an initial compact state over the probed acceleration voltage range, with nearly identical acceleration voltages required to initiate each CIU transition (Figure 5-1C–F). Conversely, we also

observed a marked difference in the variance associated with the CIU fingerprint for RS at collision voltages below 50 V, which was not observed in RC, highlighted in the white box in Figure 5-1F. Previous evidence has linked this region of mAb CIU plots to the Fc region and glycoform variation, and we interpret the highlighted variation in Figure 5-1F as being related to similar features within RS.

To evaluate chemical modifications of these mAbs in detail and map them to either the Fab or Fc portion of the proteins, the two products were subjected to IdeS digestion. The digestion generates F(ab)′2 and 2Fc fragments (Figure 5-2A), and these fragments were analyzed intact by MS. Glycosylated Fc fragments displayed poor MS spectral resolution, especially for the RS samples (Figure 5-2B), suggesting more heterogeneous structures. Upon deglycosylation, better MS resolution was achieved for both products (Figure 5-2C), and allowed for the identification of C-terminal lysine truncations under native conditions. The denaturing MS analysis after deglycosylation and reduction also confirmed that higher levels of C-terminal Lys-truncated isoforms were present in RS (72.0 ± 3.5%) than in RC (62.0 ± 10.8%). Celltrion reported this difference by identifying mAbs species that have two, one, and zero C-terminal Lys residues present by ion-exchange chromatography, with levels of full-length mAbs of 26.5% (RC) and 16.6% (RS).[13] The manufacturer also confirmed that the presence of a C-terminal Lys has no bearing on infliximab's PK or activity, as it is rapidly cleaved *in vivo* for both products.[13]

Alternatively, for F(ab)′2 mass spectra, several peaks were resolved and showed consistent mass shifts approximately corresponding to the addition of two sugar molecules in a process known as glycation, or the noncovalent linkage of sugar to a lysine residue.[31] Apart from the unmodified Apo state, we observed Apo+1S to Apo+5S states corresponding to addition of 2–10 sugars. The levels of highly glycated Fab (+5S) were higher for RS (5.2 ± 2.9%) than for RC (1.7 ±

0.9%). Sucrose makes up a significant portion of the drug product, and glycation has been observed for other mAb products. The presence of glycation was confirmed by LC–MS/MS quantitative peptide map analysis using Glu-C for digestion, with overall glycation levels of 0.54% for RC and 3.42% for RS (Figure IV-2). Nonenzymatic glycation was analyzed by the manufacturer using a different method involving a deglycosylation/reduction treatment followed by mass analysis and was determined to be 0.8% (HC) and 0.8% (LC) and 4.0% (HC) and 2.4% (LC) for RC and RS, respectively.[13] The manufacturer data showed that none of the glycation sites were located near the TNFα binding sites, thus the glycation is expected to have no impact on their biological activity.[13]

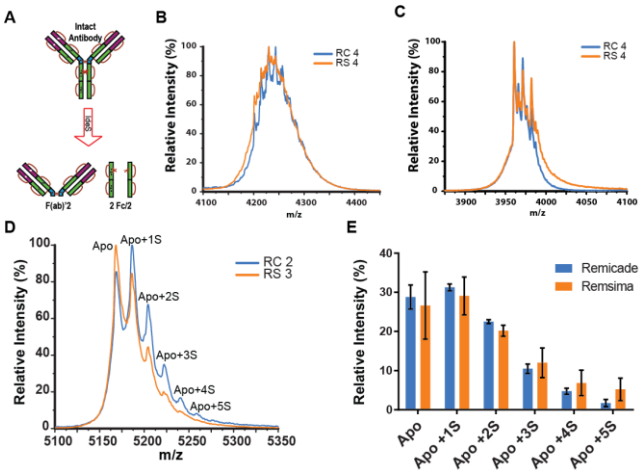

Figure 5-2. Intact mass analysis of IdeS digests of Remicade and Remsima. (A) Schematic for IdeS enzyme cleavage. Representative intact mass spectra of the 12+ charge state of Fc regions for RC lot 4 and RS lot 4 (B) before and (C) after deglycosylation. (D) Representative mass spectra of the 19+ charge state of the Fab region of RC lot2 and RS lot 3 resolved peaks of the apo or unmodified and several sugar-modified variants (Apo+1S to Apo+5S, corresponding number of glycations). (E) Glycation on the Fab region of RC and RS (n = 3 lots per product; mean ± SEM).

The differences in the glycosylation heterogeneity suggested by the IM-MS and CIU data were then evaluated by label-free LC-MS analysis of trypsin-digested peptides. (Table IV-1) More than 24 glycoforms were identified, of which the most abundant were G0F (48.9% RC, 40.7% RS) and G1F (21.6% RC, 37.0% RS), while the least abundant was N-glycolylneuraminic acid (0.03% RC, 0.02% RS). The levels of mannose-terminated glycans, known to reduce the circulation time of mAbs, but possibly also to increase the extent of FcγRIIIa binding, were also found to be different between the two mAbs (14.9 ± 1.5% for RC and 9.0 ± 3.1% for RS). A total of 14 afucosylated

glycoforms were identified in both products with the total afucosylation levels being higher for RC (19.7 ± 1.6%) than for RS (13.2 ± 3.8%). The three most prevalent afucosylated glycoforms were Man5 (7.82% RC, 6.46% RS), G0-Man(3) (3.89% RC, 0.40% RS), and G0-GlcNAc (2.07% RC, 0.43% RS).

To assess how this measured difference in afucosylation levels between RC and RS influences mAb biological activity, we measured binding of RC and RS to FcγRIIIa using biolayer interferometry (BLI).(Figure IV-3) Indeed, RC bound to FcγRIIIa with a K_D (162 ± 18 nM) 2-fold lower than that of RS (351 ± 48 nM). The differences in FcγRIIIa binding between RC and RS have been measured using surface plasmon resonance (SPR) by the biosimilar manufacturer and were reported in the FDA briefing document. [13,25] The levels of binding of RC and RS to FcγRIIIa were reported to be 126 ± 7.7 and 101 ± 2.3%, respectively, relative to the reference standard (for a separate lot of RS vs what is studied here). This difference in FcγRIIIa binding for the two products leads to residual uncertainty regarding the biosimilarity of RC and RS in IBD, as it affects ADCC,[32] and theoreticaclly ADCC could play a role in the mechanism of action of infliximab by downregulating intestinal inflammation.[33] Indeed, a 20% reduction in natural killer cell-induced ADCC activity of RS over RC was reported in the FDA briefing document.[25] However, 90% of all RS lots tested appeared to be within statistical variability of RC's ADCC values. Based on these data along with the extrapolation of the clinical data for RA, RS was approved for the treatment of IBD indications. Our data underscore how chemical analysis of the biosimilar product could be correlated with its bioactivity to define clinical efficacy testing requirements.

To further examine how analytical characterization could be used to foresee potential clinical safety issues, we have used native IM-MS data together with size exclusion chromatography to examine RS and RC aggregation. The presence of protein aggregates has long been attributed to

increased immunogenicity with the formation of antidrug antibodies and neutralizing antibodies (NAbs).[34] IM-MS analysis confirmed the presence of mAb dimers, 0.78 ± 0.22% for RC and 1.26 ± 0.99% for RS. The large dimer differences between the two products as measured by IM-MS may be attributed to method variability and should be interpreted with caution, as only two batches of each product were analyzed. Size exclusion chromatography (SEC) corroborated our IM-MS data, detecting small differences in soluble dimer levels of RC (0.06 ± 0.02%) and RS (0.37 ± 0.17%). (Figure IV-4) The higher levels of high-molecular weight forms were reported in regulatory filing of 0.2% (RC) and 0.8% (RS) as measured by SEC. Another factor that may affect immunogenicity is the presence of subvisible particulates, and biologic production processes are in place to limit such particulates in the 10–25 μm size range. Regulatory filings suggest both RS and RC have a varied range of subvisible particles between the sizes of 1–100 μm, as measured by light obscuration and microflow imaging, but the levels across the products were comparable.[13] However, infliximab is highly immunogenic because of its chimeric nature, and detectable levels of NAb were found in >50% of RA patients in both the RC and RS treatment arms.[11,13,35] The response of the patient to the murine portion of infliximab likely dominates its immunogenicity over any small differences in aggregation state.

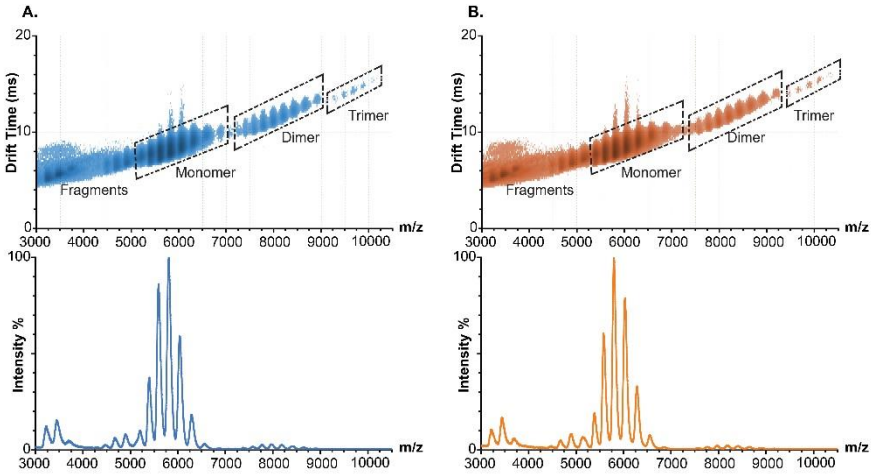

Figure 5-3. IM-MS spectra of A) Remicade, B) Remsima after 4 weeks at 97% relative humidity. Fragment, monomer, dimer and trimer species annotated in ion mobility spectra.

Following the assessment of aggregation state, we performed a forced degradation study to evaluate the similarity between the two mAbs regarding their stability and degradation pathways. The IM-MS results suggested that small initial levels of antibody impurities increase significantly after humidity and temperature stressing (Figure 5-3). For example, the presence of dimer and trimer protein aggregates, as well as 50 and 100 kDa antibody fragments, were observed in stressed samples. Appearance of these species was evident from the different drift times relative to protein monomer drift time, as observed in IM-MS spectra (Figure 5-3). While the initial levels of aggregates were slightly higher for Remsima™ than for Remicade®, these differences did not result in faster aggregation upon stress for Remsima™. The levels of dimer were similar in stressed samples for Remsima™ (12.4% by SEC and 3.5% by IM-MS) and Remicade® (12.7% by SEC and 3.0% by IM-MS), and the presence of trimers was detected at 0.1% in both products by IM-MS. The PTMs were assessed for the stressed samples via LC-MS analysis, revealing increased levels of deamidation in both Remicade and Remsima that were comparable.(Table IV-2) In addition, the kinetics of monomer loss were monitored by SEC measurements and were highly similar for the two mAbs. (Table IV-3) Despite the differences observed initially, Remicade and

Remsima displayed almost identical degradation mechanism and kinetics. The forced degradation study results reinforced the exceptional comparability of the biosimilar to the originator infliximab.

5.4 Conclusions

RS is just the first of multiple mAb biosimilar products that are on track for approval by the FDA. While individual analytical assays can distinguish product variants and impurities, lab-to-lab variability in analytical methods and equipment makes the comparison of data cumbersome. This study represents an example of a rapid and thorough examination of two products by an independent laboratory, allowing the identification of clinically relevant differences such as afucosylated glycans levels (RC, 19.7%; RS, 13.2%) and FcγRIIIa binding (RC, 162 nM; RS, 351 nM). The analytical tools described here can provide extensive data, ranging from primary modifications (levels as low as <0.2%) to intact structural features, and could be a compelling template for emerging MAM workflows.[36,37] The ability to rapidly characterize and quantify complex mAb glycoforms will be especially critical for examining the biosimilarity of oncology products that are reliant on an ADCC mechanism of action driven by afucosylation levels. Rapid quantification of oxidation, deamidation, glycation, and aggregation improves our general understanding of both the product and process variability inherent in therapeutic development pipelines and pinpoints “hot spots” leading to protein instability. Such MAM approaches will undoubtedly provide invaluable insights for mAb development and biosimilar comparison, as well as characterization of post-approval innovator product changes, resulting from process modifications, scale-up, and plant transfers.

5.5 Supporting Information

Supporting information can be found in Appendix IV.

5.6 Acknowledgement

Work in this chapter was performed in collaboration with Anna Schwendeman Group at the University of Michigan. Karthik Pisupati provided the Remicade and Remsima samples, offered great discussion along the way, and combined our IM-MS data with all other analytical and biophysical results for publication.

5.7 References

(1) Beck, A. *MAbs* **2011**, *3* (2), 107–110.
(2) Mulcahy, A. W.; Predmore, Z.; Mattke, S. .
(3) Mulcahy, A. W.; Hlavka, J. P.; Case, S. R. **2017**, No. July.
(4) Kozlowski, S.; Woodcock, J.; Midthun, K.; Behrman Sherman, R. *N. Engl. J. Med.* **2011**, *365* (5), 385–388.
(5) European Medicines Agency (EMA). *Guideline on similar biological medicinal products containing monoclonal antibodies – non-clinical and clinical issues.* **2014**.
(6) Food and Drug Administration. *Quality Considerations in Demonstrating Biosimilarity of a Therapeutic Protein Product to a Reference Product to a Reference Products*; **2015**.
(7) Food and Drug Administration. *Scientific Considerations in Demonstrating Biosimilarity to a Reference Product Guidance for Industry*; **2015**.
(8) Product, P. *Biotechnol. Law Rep.* **2012**, *31* (2), 185–195.
(9) Konara, C. S.; Barnard, R. T.; Hine, D.; Siegel, E.; Ferro, V. *Trends Biotechnol.* **2016**, *34* (1), 70–83.
(10) Beck, A.; Reichert, J. M. *MAbs* **2013**, *5* (5), 621–623.
(11) European Medicines Agency (EMA). *Assessment report Inflectra*; 2013; Vol. 44.
(12) European Medicines Agency (EMA). *REMSIMA - Assessment report*; 2013; Vol. 44.
(13) *CT-P13 FDA Advisory Committee Briefing Document CT-P13 (infliximab biosimilar) BRIEFING DOCUMENT FOR THE ARTHRITIS ADVISORY COMMITTEE*; 2016.
(14) Jung, S. K.; Lee, K. H.; Jeon, J. W.; Lee, J. W.; Kwon, B. O.; Kim, Y. J.; Bae, J. S.; Kim, D.-I.; Lee, S. Y.; Chang, S. J. *MAbs* **2014**, *6* (5), 1163–1177.
(15) Health Canada. Summary Basis of Decision - Inflectra https://hpr-rps.hres.ca/reg-content/summary-basis-decision-detailTwo.php?linkID=SBD00253.
(16) Kanu, A. B.; Dwivedi, P.; Tam, M.; Matz, L.; Hill, H. H. Ion mobility-mass spectrometry. *Journal of Mass Spectrometry*, 2008, *43*, 1–22.
(17) Engen, J. R.; Wales, T. E. *Annu. Rev. Anal. Chem.* **2015**, *8* (1), 127–148.
(18) Ferguson, C. N.; Gucinski-Ruth, A. C. *J. Am. Soc. Mass Spectrom.* **2016**.
(19) Greenspan, L. *J. Res. Natl. Bur. Stand. -A. Phys ics Chem. 81* (1).
(20) Giles, K.; Williams, J. P.; Campuzano, I. *Rapid Commun. Mass Spectrom.* **2011**, *25* (11), 1559–1566.
(21) Zhong, Y.; Hyung, S.-J.; Ruotolo, B. T. *Analyst* **2011**, *136* (17), 3534–3541.
(22) Tian, Y.; Han, L.; Buckner, A. C.; Ruotolo, B. T. *Anal. Chem.* **2015**, *87* (22), 11509–11515.
(23) McKay, A. R.; Ruotolo, B. T.; Ilag, L. L.; Robinson, C. V. *J. Am. Chem. Soc.* **2006**, *128*

(35), 11433–11442.
(24) Eschweiler, J. D.; Rabuck-Gibbons, J. N.; Tian, Y.; Ruotolo, B. T. *Anal. Chem.* **2015**, *87* (22), 11516–11522.
(25) *FDA Briefing Document Arthritis Advisory Committee Meeting. BLA 125544 CT-P13, a proposed biosimilar to Remicade® (infliximab)*; 2016.
(26) Hyung, S.-J.; Robinson, C. V; Ruotolo, B. T. *Chem. Biol.* **2009**, *16* (4), 382–390.
(27) Han, L.; Hyung, S. J.; Mayers, J. J. S.; Ruotolo, B. T. *J. Am. Chem. Soc.* **2011**, *133* (29), 11358–11367.
(28) Han, L.; Hyung, S.-J.; Ruotolo, B. T. *Angew. Chemie Int. Ed.* **2012**, *51* (23), 5692–5695.
(29) Rabuck, J. N.; Hyung, S.-J.; Ko, K. S.; Fox, C. C.; Soellner, M. B.; Ruotolo, B. T. *Anal. Chem.* **2013**, *85* (15), 6995–7002.
(30) Tian, Y.; Ruotolo, B. T. *Int. J. Mass Spectrom.* **2018**, *425*, 1–9.
(31) Miller, A. K.; Hambly, D. M.; Kerwin, B. A.; Treuheit, M. J.; Gadgil, H. S. *J. Pharm. Sci.* **2011**, *100* (7), 2543–2550.
(32) Dörner, T.; Kay, J. *Nat. Rev. Rheumatol.* **2015**, *11* (12), 713–724.
(33) Peake, S. T. C.; Bernardo, D.; Mann, E. R.; Al-Hassi, H. O.; Knight, S. C.; Hart, A. L. *Inflamm. Bowel Dis.* **2013**, *19* (7), 1546–1555.
(34) Ratanji, K. D.; Derrick, J. P.; Dearman, R. J.; Kimber, I. *J Immunotoxicol* **2014**, *11* (2), 1547–1691.
(35) Yoo, D. H.; Hrycaj, P.; Miranda, P.; Ramiterre, E.; Piotrowski, M.; Shevchuk, S.; Kovalenko, V.; Prodanovic, N.; Abello-Banfi, M.; Gutierrez-Ureña, S.; Morales-Olazabal, L.; Tee, M.; Jimenez, R.; Zamani, O.; Lee, S. J.; Kim, H.; Park, W.; Müller-Ladner, U. *Ann. Rheum. Dis.* **2013**, *72* (10), 1613–1620.
(36) Berkowitz, S. a.; Engen, J. R.; Mazzeo, J. R.; Jones, G. B. *Nat. Rev. Drug Discov.* **2012**, *11*, 527–540.
(37) Pais, D. A. M.; Carrondo, M. J.; Alves, P. M.; Teixeira, A. P. *Curr. Opin. Biotechnol.* **2014**, *30*, 161–167.

Chapter 6. A Novel Hydrogen/Deuterium Exchange-Mass Spectrometry Workflow for the Analysis of High Concentration Antibody Formulations

Abstract

High concentration biotherapeutic formulations are often required to deliver large doses of drugs to achieve a desired degree of bioavailability and efficacy. Despite this, highly concentrated protein-containing solutions may exhibit undesirable therapeutic properties; such as increased viscosity, aggregation, and phase separation that can affect drug efficacy and raise safety issues. Therefore, the characterization of high concentration protein formulations is a critical yet challenging analytical task for therapeutic development efforts, due to the lack of technologies capable of making accurate measurements under such conditions. To address this issue, we have developed a novel hydrogen/deuterium exchange (HDX) mass spectrometry (MS) method for the direct conformational analysis of high concentration biotherapeutics. In this work, we first dialyzed mAbs in either hydrogen or deuterium containing buffers at low salt and pH. At high protein concentrations, phase separation can occur, and both phases are subjected to HDX-MS analysis through discrete sample and mixing heavy and light labeled samples produced for opposite phases. Our HDX-MS results analyzed at a global protein level reveal less deuterium incorporation for the protein-enriched phase compared to the protein-depleted phase present in high concentration formulations. A peptide level analysis further confirmed these observed differences, and a detailed statistical analysis provided direct information surrounding the details of the conformational changes observed. We conclude by proposing possible structures for the

self-associated mAbs present at high concentrations based on our HDX-MS results. Our new method can potentially provide useful insights on the unusual behavior of therapeutic proteins in high concentration formulations, helping with the development of such therapeutics.

6.1 Introduction

Over the past few decades, monoclonal antibodies (mAbs) have grown significantly as treatment strategies for cancers and chronic diseases.[1,2] For certain clinical indications, frequent high therapeutic doses (> 1mg/kg) are often required to achieve a desired bioavailability and efficacy.[3] Conventionally, such protein therapeutics are delivered via intravenous (IV) administration in order to take advantage of the improved bioavailability and the greater control offered by the method during clinical development when compared with other approaches to drug administration.[4] Despite the wide usage of IV administration, large doses of biopharmaceuticals can take a long time to be delivered intravenously and often require frequent hospital visits, leading to substantial cost increases for patients and healthcare providers. Subcutaneous (SC) injections can serve as an alternative drug administration strategy, allowing for patient self-administration and reducing overall costs, but very high therapeutic concentrations (>100 mg/mL) are required to deliver high doses.[5]

Despite the advantages of SC administration, development of mAbs formulated at such high concentrations presents many challenges in processing, manufacturing, storage and delivery, mainly owing to the non-ideal behaviors of highly concentrated proteins that are quite different from those observed for dilute solutions. Unusual protein behaviors at high concentrations often stem from protein self-association, leading to undesired solution properties such as: increased solution viscosity, opalescent solution appearance, and liquid-liquid phase separation.[3,6–9] These unwanted properties can affect drug efficacy and raise safety issues. Liquid-liquid phase separation

(LLPS) poses an especially challenging array of problems in the context of biopharmaceutical development efforts.[9–14] LLPS is a thermodynamically driven process, during which a homogeneous protein solution forms two distinct phases. The less dense phase typically exhibits a lower protein concentration, whereas the higher density phase is protein-enriched. LLPS is usually induced by antibody self-association at low temperatures, resulting in protein concentrations for the two phases that are dependent on both temperatures and buffer conditions. LLPS represents a metastable state of the protein solution and can be reversed upon changes in temperature or formulation environment. Many studies have been carried out to investigate the manner in which LLPS phase diagrams are affected by buffer composition, pH, ionic strength and various excipients.[10,11] Characterization of the two protein phases has been performed using various analytical and biophysical techniques, such as size exclusion chromatography (SEC), ion exchange chromatography (IEX), analytical ultracentrifugation (AUC), dynamic light scattering (DLS), turbidity and viscosity tests.[13] However, most of the abovementioned techniques can only be performed on diluted solutions, and thus fail to probe the resulting protein structures prevalent at such high concentrations. Therefore, analytical techniques that require minimal sample manipulation and dilution are needed to better understand the structural consequences of highly concentrated proteins that are of relevance to biopharmaceutical development efforts.

Hydrogen/deuterium exchange-mass spectrometry (HDX-MS) is a versatile tool for the assessment of protein conformations, dynamics and interactions, and is now increasingly applied toward mAb analysis.[15–19] However, traditional HDX-MS workflows are typically initiated through the exchange of labile backbone amide hydrogens by diluting protein samples into a D_2O-containing buffer.[19] Thus, the use of HDX-MS has been limited for analyzing protein samples at very high concentrations. Recently, HDX-MS workflows designed for the analysis of high

concentration protein samples have been described .[20,21] For example, a recently described HDX-MS methodology that relies upon reconstituting lyophilized mAb powders in a deuterated buffer was able to characterize mAb structures at 60 mg/mL.[20] This approach identified protein-protein interfaces associated with a concentration-dependent reversible self-association. While lyophilization combined with HDX-MS can provide protein structure information in a dilution-free mode, the workflow introduces a reconstitution step and is limited to those buffers amenable to the lyophilization process. To overcome these limitations, a dialysis-coupled HDX-MS strategy was recently reported for mAb analysis, in which passive dialysis microcassettes are used for HDX labeling.[21] While this approach successfully sampled high concentration (200 mg/mL) IgG4 formulations for comparison with low concentration (3 mg/mL) samples, the long timescales needed for dialysis likely render many known modes of protein motion inaccessible to the technology.

In this work, we describe a refined dialysis strategy for HDX-MS of high concentration protein samples. We begin by preparing two mAb samples at fixed concentrations using dialysis in either hydrogen or deuterium containing buffers under the same conditions. To keep protein concentration constant, HDX reactions were initiated by mixing the two protein fractions in a 1 to 1 ratio, followed by MS analysis of either intact protein or peptide level. We then applied this HDX-MS approach toward the characterization of phase separated IgG4 samples. Our global HDX-MS data reveals less deuterium uptake for mAbs in the high-density phase when compared to those in the low-density phase, suggesting the prevalence of less dynamic mAb conformations within the former phase. A statistical analysis of our HDX-MS results acquired at the peptide level identified mAb regions exhibiting significant decreases in HDX for mAbs present in the high-

density phase. We conclude by proposing a molecular mechanism that describes our phase separated IgG4 samples.

6.2 Materials and Methods

Materials

A humanized IgG4 monoclonal antibody (referred to as "Mab4") was expressed, purified and formulated at Eli Lilly and Company. Deuterium oxide (99.9% atom D) was purchased from Sigma-Aldrich. Tris(2-carboxyethyl) phosphine hydrochloride (TCEP·HCl), 8M guanidine-HCl Solution, formic acid (FA), trifluoroacetic acid (TFA) and Slide-A-Lyzer™ MINI dialysis device (10K MWCO, 2 mL) were purchased from ThermoFisher Scientific. All other chemicals were purchased from Fisher Scientific.

Buffer Screening Experiments

10 mM citrate buffers at pH 5.5, 6, and 6.5 were prepared by dissolving citrate acid solid and monosodium citrate solid at specific ratios. Sodium chloride solid was weighed and dissolved in the citrate buffer to keep the ionic strengths. Buffer pH was measured and adjusted using a calibrated pH meter at room temperature. Mab4 was buffer exchanged through overnight dialysis using the 10K MWCO dialysis device. After protein dialysis, Mab4 samples were stored at 5 ºC at least overnight to allow phase separation. After phase separation, the concentrations of Mab4 in the two phases were measured with UV-Vis at 280 nm. The results were discussed in the Supporting Information and were used to determine the buffer condition for the following phase separation study.

Phase Separation Sample Preparation for HDX-MS

10 mM citrate buffer with 50 mM NaCl at pH 6 was chosen for phase separation study. Two buffers were prepared for HDX-MS, using water or deuterium oxide as solvent. Two fractions of Mab4 samples were prepared. One Mab4 fraction was dialyzed into the buffer prepared in water and another fraction was dialyzed into the buffer prepared in D_2O. Mab4 samples were then incubated at 5 ºC for one week, allowing phase separation. Longer incubation time also permits the hydrogen deuterium exchange to reach equilibrium for Mab4 prepared in D_2O buffer. Concentrations of the two protein phases were measured with UV-Vis at 280 nm.

Biophysical Assays - Differential Scanning Calorimetry and Dynamic Light Scattering

Protein samples were taken from the two separated phases and diluted to 1 mg/mL using the same buffer. DSC measurements were performed on a MicroCal DSC instrument (Malvern Panalytical technologies). Temperature was ramped from 25 ºC to 90 ºC at 1 ºC/min rate. The buffer-buffer baseline was measured before running the protein sample. The baseline subtracted thermograms were plotted. The onset temperature and max temperature for unfolding transition were obtained from the DSC data.

DLS measurements were performed on four protein concentrations: 0.5 mg/ml, 1 mg/ml, 2 mg/ml, and 3 mg/ml. Protein samples were taken from the two separated phases and diluted to the target concentrations. The interactions parameter (k_D) value was then determined by a linear fit of the measured (mutual) diffusion coefficients (Dm) as a function of concentration.

Global Hydrogen Deuterium Mass Spectrometry

For proteins in the upper phase, 10 µL of sample in water buffer was taken and mixed with 10 µL of sample in D_2O buffer. The mixture was incubated in the LC autosampler at ~ 5 ºC. LC-MS sequence was set up to inject the sample at 100s, 460s, 7300s, 1000s, 10000s, 20080s, and 29980s.

The HDX reaction was quenched once the protein sample was loaded into the LC sample loop and mixed with acidified mobile phase. The protein sample was desalted and eluted on a reverse phase column (Agilent PLRS 1 x 50 mm, 1000 Å, 5 µm), using mobile phase composed of 0.05% TFA in H_2O and 0.04% TFA in acetonitrile. The LC column was kept in an ice bath to minimize back exchange. Following on-line LC separation, MS analysis was performed on a Water Synapt G2-Si Q-Tof mass spectrometer. For protein sample in the lower phase, global HDX-MS analysis was performed following the same protocol as above.

Bottom-up Hydrogen Deuterium Exchange Mass Spectrometry

A quench buffer containing 0.45 M TCEP, 3.6 M GdnHCl and 0.18 M phosphate at pH 2.3 was prepared and equilibrated at ~0 ºC. For analysis of Mab4 in the upper phase, 2 µL of protein sample in H_2O buffer was mixed with 2 µL of the sample in D_2O buffer and incubated at 5 ºC for five labeling time points: 30s, 100s, 1000s, 2000s, and 10000s. At each timepoint, the exchange reaction was quenched by quickly adding 60 µL of quench buffer at 0 ºC, followed by the dilution with 60 µL of 0.1% FA, pH 2.5. The quench and dilution time was carefully controlled at 1 min. The labeled and quenched sample was then subject to protease digestion by incubating with 8 µL of 10 mg/mL pepsin at 0 ºC for 3.5 min. For analysis of proteins in the concentrated phase, the exchange reaction was carried out and quenched in the same fashion, except that 28 µL of 10 mg/mL pepsin were used to produce more effective digestion due to the higher protein concentration. Consequently, the volume of 0.1% formic acid added to the higher density phase sample was lowered to 40 µL, in order to keep the sample dilution levels consistent with the sample from the lesser density phase

The digested sample was immediately analyzed by LC-MS. Peptides were separated on a C18 column (Waters ACQUITY UPLC CSH C18, 1.7µm, 2.1 x 50mm). To minimize back exchange,

the LC column was kept in an ice bath. Mobile phase was comprised of H_2O and acetonitrile, both containing 0.1% FA. An acetonitrile gradient from 10% to 50% was used to elute the peptides. The eluents were directly analyzed by a Thermo Scientific Orbitrap Fusion Lumos Tribrid™ Mass Spectrometer running in positive mode.

HDX-MS Data Analysis

Masslynx (Waters Corp.) was used to process global HDX-MS data. The zero-charge mass spectrum was generated by performing the MaxEnt deconvolution. The global HDX-MS kinetic plot was created by plotting the measured intact mass of the deuterium labeled mAb against the reaction time. For peptide level HDX-MS data, MS/MS data collected for the control sample was processed using Proteome Discoverer (Thermo Scientific) to generate a reference peptide list. The HDX-MS data were then analyzed using Mass Spec Studio.[22] Briefly, both a master peptide list and the raw MS data were input into the software to produce initial peptide identifications. Peptides identified based on both their monoisotopic mass and retention time were then manually validated. Though Mass Spec Studio cannot directly deconvolute the bimodal distributions detected for our deuterated peptide signals, it is capable of estimating the deuterium content by fitting a subset of isotopic peaks to an isotope expansion model. Statistical analysis was performed to calculate the averaged standard deviation of deuterium uptake across all peptide replicates. In addition to the 2x standard deviation criteria, a two-tailed Student's t-test was performed using pooled standard deviation to calculate the p-values from the replicate data on a per-peptide basis A homology model was built based on the crystal structure of IgG4 (PDB: 5DK3) using PyMod 2.0 within Pymol.[23,24] Statistical analysis of the HDX-MS was performed using the statistical analysis module in Mass Spec Studio and the results were visualized using our homology model.

6.3 Results and Discussion

DSC and DLS Measurements Reveal Concentration Dependent mAb Structures

As reported in the literature and observed in our buffer screening experiments, LLPS is a reversible process for high concentration mAb samples. When the temperature is higher than the critical temperature (T_C), the two phases merge and reform one homogeneous phase.[10] Similarly, if the highly concentrated solution is diluted to a concentration lower than the concentration of upper phase, then phase separation will not occur. Despite previous studies, many questions remain surrounding the structures of phase separated mAbs. Specifically, these questions include those focused on whether proteins possess any specific structural characteristics that favor one phase over another, and if proteins can adapt their conformations upon phase separation. In addition, it is not clear if proteins are able to maintain structural properties acquired during phase separation at high concentration following sample dilution. In an effort to answer some of the questions above, we assembled an array of biophysical tools to study Mab4 under LLPS conditions.

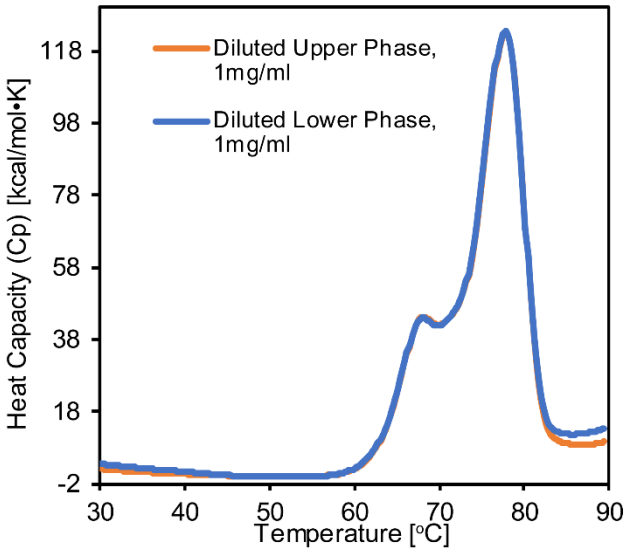

Figure 6-1. DSC thermograms of Mab4 from upper phase (orange) and lower phase (blue). Both samples were diluted to 1 mg/mL. Protein denaturation was induced by ramping temperature to 90 °C at 1 °C/min rate.

We performed DSC measurements in order to characterize the thermal stability of phase separated Mab4. Samples from the two phases were taken and diluted to 1 mg/mL prior to DSC measurements. As shown in Figure 6-1, the two samples exhibit highly similar melt temperature profiles, consisting of two major transitions taking place around 68.0 ºC and 77.8 ºC. The nearly identical DSC profiles recorded for the two Mab4 samples strongly indicate that the mAbs occupy similar structures regardless of the phases they are present in during phase separation process, or that any phase-dependent structural changes are not retained following the sample dilution step necessary for DSC. DLS measurements for diluted Mab4 samples produced results similar to our DSC experiments. A diffusion interaction parameter (k_D) can be empirically determined by measuring the diffusion coefficient (D) for mAbs as a function of protein concentration based on DLS data. Within the concentration range from 0.5 mg/mL to 3 mg/mL, extracted k_D values are -52.1 mL/g and -50.8 mL/g for Mab4 in the low and high-density phases respectively. Negative k_D values represent attractive intermolecular interactions, suggesting a tendency for Mab4 to self-associate and aggregate independent of the protein concentration.

An HDX-MS workflow for phase separated mAb samples at high concentration

In order to assess protein structures directly at high concentration, we designed an HDX-MS workflow that can be performed in the absence of dilution. The experimental procedure is shown in Figure 6-2. Generally, the sample preparation begins with overnight dialysis of protein into the target formulation. (Fig. 6-2A, B) Dialysis is performed using a 10 kDa MWCO MINI dialysis device that can hold 2 mL maximum sample volume, placed in a 50 mL conical tube containing the dialysis buffer. The conical tube is gently shaken at ~200 rpm to avoid agitation-induced aggregation. Dialysis buffer is changed twice during dialysis to reach full equilibrium. Two dialysis buffers comprising the same chemical formulation are prepared, of which one was in H_2O

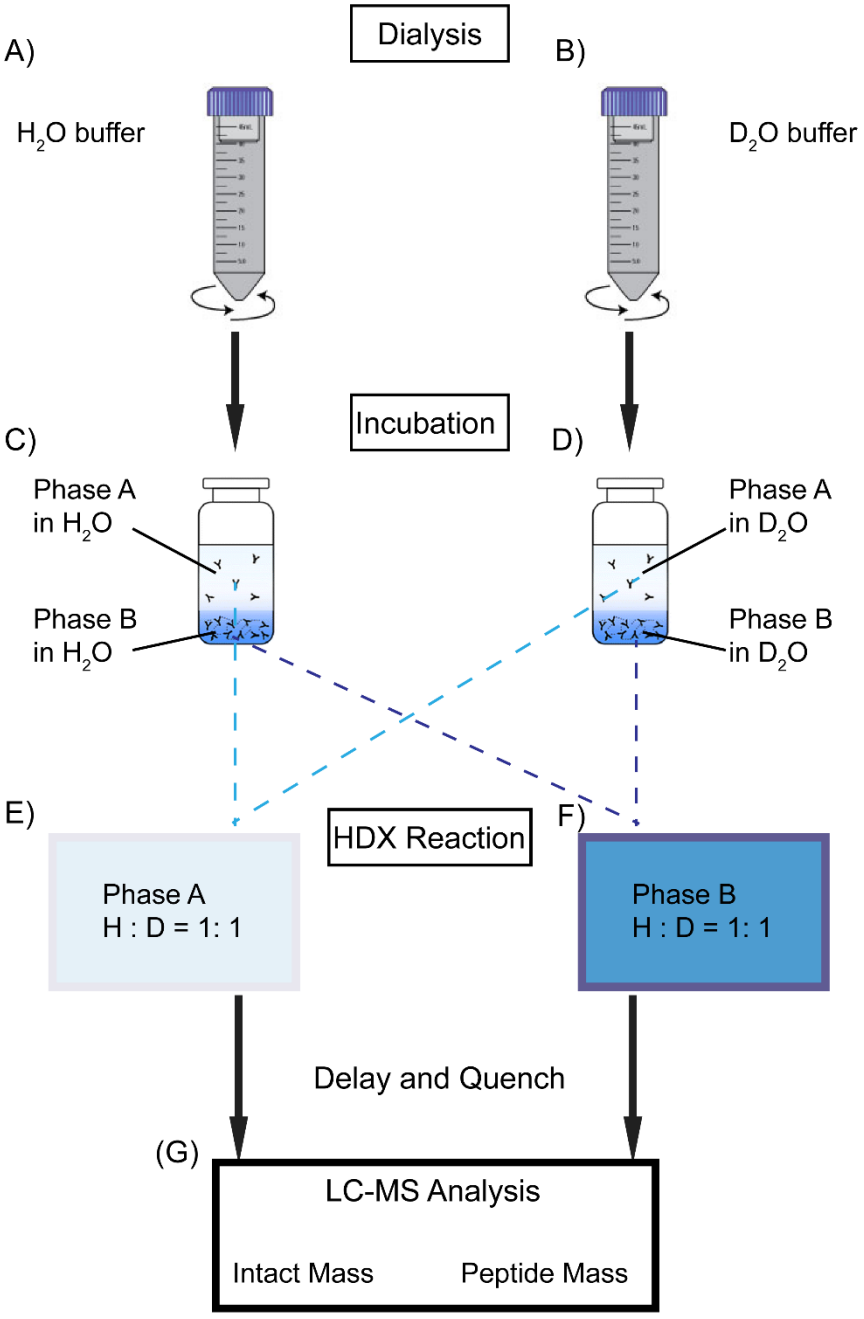

Figure 6-2. Schematic of dilution-free HDX-MS workflow, taking phase separation sample as an example. The experiment starts with sample dialysis into the target formulation in H_2O (A) or D_2O (B). Protein samples are then incubated at certain temperature allowing equilibration (C, D). HDX reaction is initiated through mixing H_2O sample with D_2O sample at 1:1 ratio (E, F) and quenched at certain time points, followed by MS analysis at intact protein or peptide level.

solvent and the another in D_2O. Following the dialysis protocol described above, two fractions of the protein samples were buffer exchanged into the H_2O buffer and the D_2O buffer separately.

Meanwhile, protein in the D_2O buffer undergoes HDX. The samples are incubated for at least one week to ensure that the exchange reaches equilibrium. (Fig. 6-2C, D) Following sample preparation, HDX is initiated by mixing H_2O buffered sample with that in the D_2O buffer using a 1:1 ratio. (Fig. 6-2E, F) Because the D_2O buffer also contains protein, the overall protein concentration of the sample analyzed by MS can be maintained. Mixed samples are then subjected to MS analysis at intact protein or peptide levels.(Fig. 6-2G)

One of the advantages of this work flow over previous approaches is the ability to study the impact of LLPS and other solution phase properties on protein structure at high concentration. HDX-MS of Mab4 samples prepared at a concentration of 50 mg/mL were dialyzed into the 10 mM citrate buffer with 50 mM NaCl at pH 6. Once dialysis was complete, Mab4 solutions were stored at 5 ºC to bring about phase separation. Following LLPS, protein concentration was measured to be 28 mg/mL for the lower density phase and 150 mg/mL for the higher density phase. Previous reports have demonstrated that the impact of increased solution viscosity on the rate of HDX is negligible.[25–27] Thus, we assumed that a direct comparison of HDX profiles could be performed for Mab4 in the two liquid phases observed in our samples.

Comparative HDX-MS analysis of intact mAbs

Intact Mab4 masses were recorded for samples following HDX to provide an overall picture of antibody structural changes as a function of phase. For each mAb charge state, two resolved peaks were detected at the first reaction time point (100s), with the lower mass species corresponding to those mAbs having been incubated in hydrogen-containing buffer, and the higher mass species having fully exchanged in the presence of D_2O As HDX labeling time is increased, fully exchanged mAbs back exchange with H_2O while unexchanged mAbs undergo the forward HDX reaction, resulting in the coalescence of the separated features recorded in initial mass spectra.

Deconvoluted masses were used in our data analysis workflow to track the amount of HDX achieved experimentally.

To capture our protein level HDX results, we plotted the deuterium uptake level against HDX labeling time in order to generate an "exchange-in" profile for Mab4 sampled from the lower and higher density phases prepared in the H_2O buffer (Figure 6-3A). We observe that Mab4 sampled from the lower density phase within our samples exhibits larger mass shifts when compared Mab4 taken from the higher density phase across all labeling time points, indicating increased flexibility and surface accessibility for Mab4 molecules in the lower density phase. We also monitored HDX back-exchange, or the "exchange-out" profile for our data, and observe a different trend. (Fig. 6-3B and Fig. V-2B) Critically, the observed hydrogen uptake level is almost identical for mAbs sampled from the two phases, suggesting similar protein conformations and dynamics regardless of protein concentration.(Fig. 6-3B) The observation indicates that substituting the readily exchangeable hydrogens with deuterons as a starting point for our experiments may induce

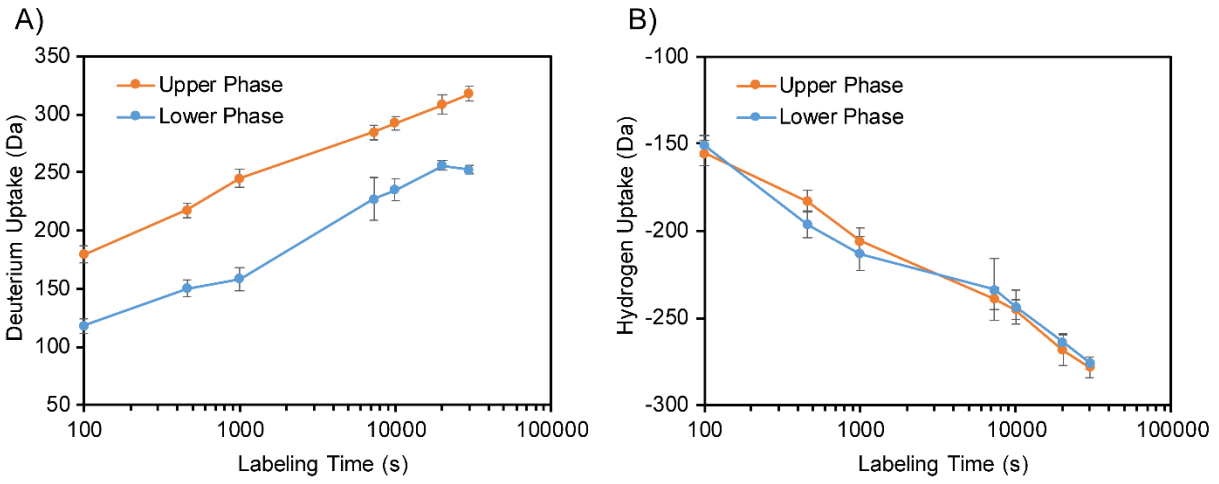

Figure 6-3. HDX exchange profiles measured by intact MS analysis. Error bars represent standard deviation from 3 individual experiments. (A) Mass increase is observed for the samples prepared in H_2O buffer. Mab4 in the upper phase exhibit higher deuterium incorporation level. (B) Mass decrease is observed for the sample prepared in D_2O buffer as the deuterated Mab4 exchange with H_2O. The deuterated proteins from the two phases have almost identical deuterium/hydrogen exchange rate.

structural changes in the antibody, causing us to focus primarily on Figure 6-3A when constructing our LLPS protein structure models below.

HDX-MS at the Peptide Level Defines Local Conformational Differences in phase separated mAbs

We probed local conformational differences in phase separated Mab4 samples using bottom-up HDX-MS. HDX labeling was carried out over five time points: 30s, 100s, 1000s, 2000s, and 10000s. In total, we detected more than 100 peptides reproducibly during our bottom-up HDX-MS analysis, producing a sequence coverage of 77.4% for the Mab4 heavy chain and 100% for the Mab4 light chain. Similar to our intact mass measurements, a bimodal distribution of isotopic peaks was typically observed for all peptides detected after the HDX reaction. However, not all deuterated species were well resolved, owing to the smaller mass differences and relatively wider isotopic distributions exhibited by small peptides upon deuteration in comparison to protein data, where average mass data is collected. Such bimodal distributions in m/z posed challenges in processing our HDX data, which were largely overcome by using Mass Spec Studio to produce an integrative data processing workflow.

Figure 6-4 shows representative selection of twelve peptides, covering all Mab4 domains, where deuterium uptake is tracked as function of labeling time. In general, most peptides detected from the higher density phase show lower deuterium uptake levels when compared to those extracted from the lesser density phase. For some of these peptides, deuteration differences observed between the two phases are consistent across all labeling time points, whereas some peptides display noticeable trends in their relative deuteration levels. To evaluate the significance of the observed differences, we used a statistical analysis module within Mass Spec Studio to further analyze our peptide HDX-MS results, outputting mass difference values across peptides and

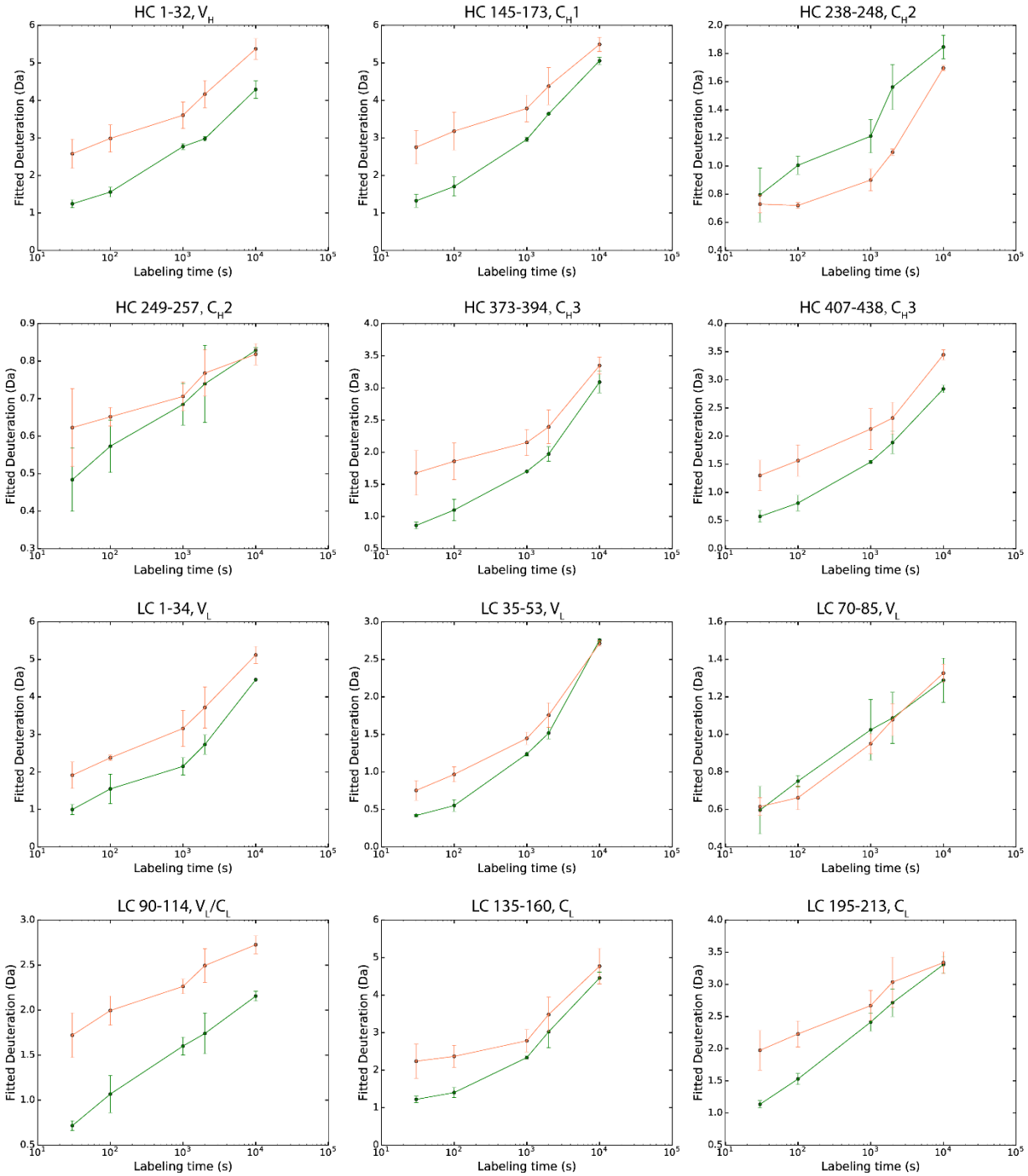

Figure 6-4. Deuterium uptake plots for 12 representative peptides in the upper phase (orange) and lower phase (green), covering all domains of Mab4. Error bars represent standard deviation from 3 individual experiments.

evaluating these changes against the mean variation in our samples to assess the statistical significance of the changes in deuterium incorporation detected. Figure 6-5. shows a global view

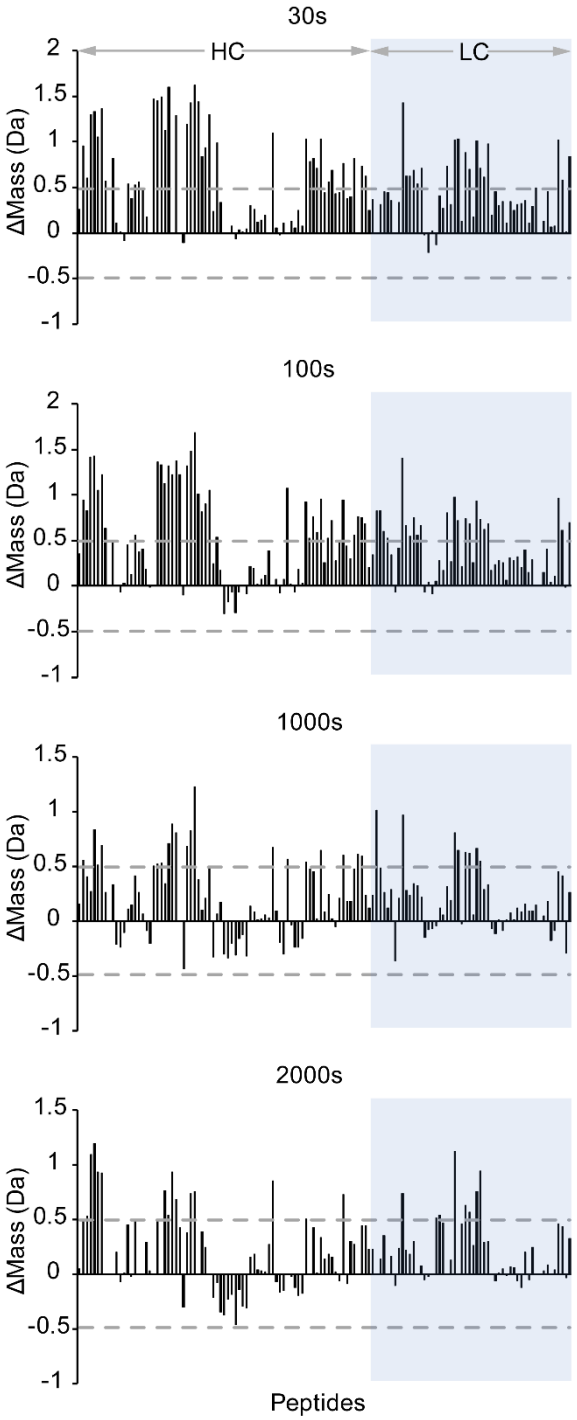

Figure 6-5. Relative mass differences in deuterium uptake at 4 time points for all peptides identified of Mab4 in the diluted phase versus in the concentrated phase. Dashed line represents the 2x standard deviation value as the cutoff limit for statistical significance.

of our statistically processed data by plotting the mass differences of all peptides and projecting gray dashed lines that represent a two standard deviation threshold (±0.48 Da) identified by our analysis as a minimal difference value to assign significance to the detected change at the 95% confidence interval. At labeling times of 30s and 100s, almost all identified peptides exhibit decreased HDX in the high-density phase, of which about 40% represent significant changes. We also note an apparent decrease in differentiated exchange patterns at longer labeling time points, likely due to false negative peak identifications due to increased mass overlap due to large absolute levels of HDX. As such, these longer timepoints are not considered in our detailed structural analysis below.

In order to begin building a molecular model of mAb conformational changes that occur during LLPS based on our data,

we mapped the HDX-MS results onto a homology model of Mab4 built from an IgG4 crystal structure. Figure 6-6 shows significant HDX differences mapped on the homology model at time points 30s and 100s. Peptide segments within Mab4 where we observed significantly decreased deuterium uptake in the high-density phase are colored blue, gray-colored areas represent peptide segments showing no significant differences between the two phases, and green regions indicate those missing from our dataset. Though we did not achieve complete sequence coverage for Mab4, the peptides identified in HDX-MS experiments comprehensively cover all Mab4 domains, giving us a detailed view on LLPS-associated structural changes. In general, we observe peptides that exhibit significant changes in deuterium uptake across all regions of the antibody, with most of detected shifts in protein flexibility and/or accessibility present in the antigen-binding fragment (Fab) and in Fc region proximal to the site of N-linked glycosylation.

Although the HDX-MS experiments cannot unambiguously map sites on the protein associated with altered structure or protein-protein contacts, our results clearly indicate that mAb conformation and dynamics are perturbed at the local level by LLPS and associated shifts in protein concentration. One possible explanation for these observations is the formation of antibody clusters in the condensed, high-density phase involving specific points on the mAb surface. The overall decrease in the deuterium uptake for molecules in the higher density phase may also be influenced by molecular crowding, which may act to rigidify the domain movements. Significant deuteration differences observed in the Fab region can be rationalized by a combination of crowding effects and the formation of mAb oligomers with protein-protein interfaces associated with the Fab and Fc regions of Mab4.

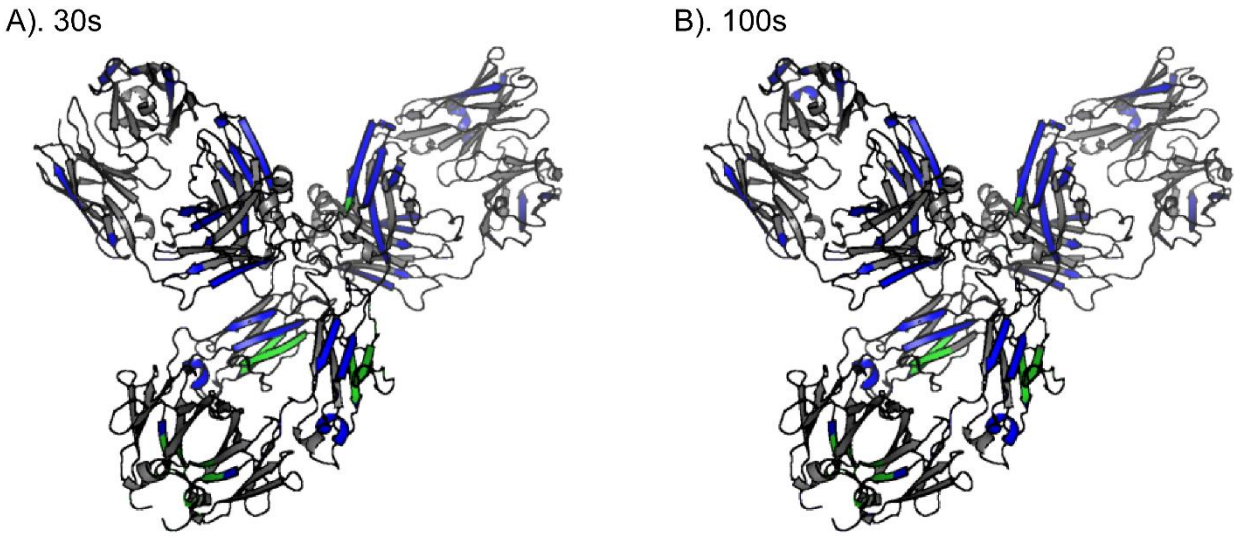

Figure 6-6. HDX-MS results mapped on a homology model, at (A) 30s and (B) 100s labeling time points. Regions where significant decreased deuterium uptake observed in the condensed phase are colored blue and regions showing no significant differences are colored gray. Green represents no HDX-MS data available.

6.4 Conclusions

Understanding the behavior of therapeutic proteins within high concentrations is of interest due to the growing demand for such high concentration formulations as treatment options. However, a lack of dilution-free analytical techniques poses many challenges in characterizing the concentration dependent protein properties. In this work, we utilized a novel HDX-MS strategy to perform a comparative conformational analysis of mAbs in a phase separated sample. Phase separation was observed for an IgG4 prepared at specific ionic strength, pH and at low temperatures, where a less dense phase containing lower concentration protein and higher density phase consisting concentrated protein were formed. We were able to carry out the deuterium labeling reaction directly at high protein concentration by mixing the protein sample with D_2O buffer containing the identical protein. In the HDX-MS monitored at the intact protein level, measured masses of deuterated Mab4 sampled from the high-density phase was constantly lower than Mab4 extracted from the low-density phase, suggesting mAb structural changes induced by phase separation. A more comprehensive HDX-MS analysis at the peptide level provided localized

structural information. Our results were mapped on a homology model, highlighting regions of the Fab and Fc regions that are likely involved in either local conformation changes or protein-protein association events at high concentrations. Ongoing efforts in experimental method development and data processing will continue to build and refine HDX-MS approaches into validated methods that can increase our understanding protein structures over an ever-wider array of therapeutically relevant conditions.

6.5 Supporting Information

Supporting information can be found in Appendix V.

6.6 Acknowledgement

I would like to thank Ning Wang and Lihua Huang for their guidance and great discussion on this project during my 6-month internship. Matthew Hyatt at Eli Lilly collected the biophysical data.

6.7 References

(1) Walsh, G. *Nat. Biotechnol.* **2014**, *32* (10), 992–1000.
(2) Ecker, D. M.; Jones, S. D.; Levine, H. L. *MAbs* **2015**, *7* (1), 9–14.
(3) Shire, S. J.; Shahrokh, Z.; Liu, J. *J. Pharm. Sci.* **2004**, *93* (6), 1390–1402.
(4) Lobo, E. D.; Hansen, R. J.; Balthasar, J. P. *J. Pharm. Sci.* **2004**, *93* (11), 2645–2668.
(5) Turner, M. R.; Balu-Iyer, S. V. *J. Pharm. Sci.* **2018**, *107* (5), 1247–1260.
(6) Yadav, S.; Laue, T. M.; Kalonia, D. S.; Singh, S. N.; Shire, S. J. *Mol. Pharm.* **2012**, *9* (4), 791–802.
(7) Yadav, S.; Liu, J.; Shire, S. J.; Kalonia, D. S. *J. Pharm. Sci.* **2010**, *99* (3), 1152–1168.
(8) Chi, E. Y.; Krishnan, S.; Randolph, T. W.; Carpenter, J. F. *Pharm. Res.* **2003**, *20* (9), 1325–1336.
(9) Ahamed, T.; Esteban, B. N. A.; Ottens, M.; van Dedem, G. W. K.; van der Wielen, L. A. M.; Bisschops, M. A. T.; Lee, A.; Pham, C.; Thömmes, J. *Biophys. J.* **2007**, *93* (2), 610–619.
(10) Mason, B. D.; Zhang-van Enk, J.; Zhang, L.; Remmele, R. L.; Zhang, J. *Biophys. J.* **2010**, *99* (11), 3792–3800.
(11) Nishi, H.; Miyajima, M.; Nakagami, H.; Noda, M.; Uchiyama, S.; Fukui, K. *Pharm. Res.* **2010**, *27* (7), 1348–1360.

(12) Lewus, R. A.; Darcy, P. A.; Lenhoff, A. M.; Sandler, S. I. *Biotechnol. Prog.* **2011**, *27* (1), 280–289.
(13) Chow, C.-K.; Allan, B. W.; Chai, Q.; Atwell, S.; Lu, J. *Mol. Pharm.* **2016**, *13* (3), 915–923.
(14) Reiche, K.; Hartl, J.; Blume, A.; Garidel, P. *Biophys. Chem.* **2017**, *220*, 7–19.
(15) Konermann, L.; Pan, J.; Liu, Y.-H. *Chem. Soc. Rev.* **2011**, *40* (3), 1224–1234.
(16) Huang, R. Y.-C.; Chen, G. *Anal. Bioanal. Chem.* **2014**, *406* (26), 6541–6558.
(17) Masson, G. R.; Jenkins, M. L.; Burke, J. E. *Expert Opin. Drug Discov.* **2017**, *12* (10), 981–994.
(18) Wei, H.; Mo, J.; Tao, L.; Russell, R. J.; Tymiak, A. A.; Chen, G.; Iacob, R. E.; Engen, J. R. *Drug Discov. Today* **2014**, *19* (1), 95–102.
(19) Houde, D.; Engen, J. R. 2013; Vol. 988, pp 269–289.
(20) Arora, J.; Hickey, J. M.; Majumdar, R.; Esfandiary, R.; Bishop, S. M.; Samra, H. S.; Middaugh, C. R.; Weis, D. D.; Volkin, D. B. *MAbs* **2015**, *7* (3), 525–539.
(21) Houde, D.; Nazari, Z. E.; Bou-Assaf, G. M.; Weiskopf, A. S.; Rand, K. D. *J. Am. Soc. Mass Spectrom.* **2016**, *27* (4), 669–676.
(22) Rey, M.; Sarpe, V.; Burns, K. M.; Buse, J.; Baker, C. A. H.; van Dijk, M.; Wordeman, L.; Bonvin, A. M. J. J.; Schriemer, D. C. *Structure* **2014**, *22* (10), 1538–1548.
(23) Bramucci, E.; Paiardini, A.; Bossa, F.; Pascarella, S. *BMC Bioinformatics* **2012**, *13* (Suppl 4), S2.
(24) Janson, G.; Zhang, C.; Prado, M. G.; Paiardini, A. *Bioinformatics* **2016**, *33* (3), 444–446.
(25) Wang, A.; Robertson, A. D.; Bolen, D. W. *Biochemistry* **1995**, *34* (46), 15096–15104.
(26) Lim, W. K.; Rösgen, J.; Englander, S. W. *Proc. Natl. Acad. Sci.* **2009**, *106* (8), 2595–2600.
(27) Manikwar, P.; Majumdar, R.; Hickey, J. M.; Thakkar, S. V; Samra, H. S.; Sathish, H. A.; Bishop, S. M.; Middaugh, C. R.; Weis, D. D.; Volkin, D. B. *J Pharm Sci* **2013**, *102*, 2136–2151.

Chapter 7. Conclusions and Future Directions

7.1 Conclusions

Over the past few decades, biopharmaceuticals have proven to be a rapidly growing class of therapeutics for various clinical indications.[1,2] Most of the biopharmaceuticals are protein-based drug products, namely monoclonal antibodies (mAbs) and related therapeutics. Many attributes, including mAb primary structures, PTMs, HOS, and degradation products need to be extensively characterized to ensure the consistency, efficacy, and safety of the biopharmaceutical. However, these therapeutic proteins are inherently large, complex and heterogeneous, thus their structural characterization is of critical importance yet poses challenges during their discovery and development.[3] Mass spectrometry has evolved into a rapid and sensitive tool for assessing the structures, stabilities, and dynamics of such proteins.[4,5] A key technology in this family is ion mobility coupled to mass spectrometry, which can provide information on protein size and shape. As some structural changes induced by PTMs or mutations can be too subtle to be captured by IM separation alone, collision induced unfolding (CIU) has been developed to resolve such conformational differences. The major part of this dissertation has focused on developing IM-MS and CIU approaches for characterization of therapeutic antibodies and antibody related drugs.

In this dissertation, a CIU strategy was developed for rapid differentiation of intact antibodies possessing different disulfide bonding patterns and general levels of glycosylation. (Chapter 2) Despite the nearly identical masses and arrival time profiles, human IgG subclasses exhibited distinct gas-phase unfolding responses upon collisional activation. Quantitative comparative

analysis of CIU fingerprints revealed antibody structural changes upon removal of N-linked glycosylation. Moreover, we validated our CIU protocol through control experiments and systematic statistical evaluations of CIU reproducibility. We further investigated the sensitivity of CIU to antibody glycoforms with subtle structural differences. (Chapter 3) Quantitative differences in CIU responses revealed changes in gas-phase structures and stabilities of intact antibodies and Fc fragments upon sequential elimination of terminal sugars in N-linked glycans. These results demonstrated that CIU assays can be used to quantitatively determine the amount of glycosylation in the antibody, given a reference dataset.

Following the initial method development, we applied IM-MS and CIU approaches to characterize pharmaceutically relevant mAbs. In Chapter 4, global CIU comparison along with the width and CIU50 analysis captured subtle differences in the gas-phase structures and stabilities of antibodies containing increasing levels of biotin conjugation, which we treated as surrogates for ADCs. These observations showed the capabilities of CIU in structural characterization of mAb-related therapeutics that are highly heterogeneous and dynamic. In Chapter 5, we demonstrated that the native IM-MS and CIU along with other MS-based methods can provide rapid and comprehensive assessment of mAb biosimilarity. These two examples of CIU applications further highlighted the possibility of integrating native IM-MS and CIU analysis into the roadmap of biopharmaceutical discovery and development.

In addition to IM-MS based approaches, we have also developed a hydrogen/deuterium exchange mass spectrometry strategy for mAb conformational analysis deployable in high concentration formulations. Since its introduction over twenty-five years ago, HDX-MS has been extensively exploited in academia, and this technique has more recently found a role in the pharmaceutical industry for characterizing structural changes induced within proteins upon ligand binding,

modification, and changes in formulation.[6,7] However, traditional HDX-MS requires diluting protein samples in the D_2O buffer, thus has limitations in assessing mAb conformations within high concentration formulations that are relevant to drug product development.[8] In Chapter 6, we analyzed an antibody sample that phase separated into a protein-depleted phase and a protein-concentrated phase using HDX-MS. The differences in deuterium uptake levels observed indicated a less dynamic structure for antibodies in the condensed phase compared to those in the depleted phase.

7.2 Future Directions

7.2.1 Structural MS for forced degradation studies to investigate mAb aggregation mechanisms

In Chapter 6, we used a novel HDX-MS strategy for mAb conformational analysis at high concentration. This is of particular interest mainly because proteins in solution at high concentrations tend to have a higher propensity for aggregation. Aggregation is one of the most common degradation pathways for therapeutic antibodies, causing activity loss, decreased solubility, and enhanced unwanted immunogenicity. Therefore, it is critical to monitor aggregate formation through multiple stages of biopharmaceutical development. In addition to high protein concentration, numerous stresses can induce the aggregation of therapeutic proteins, e.g. shaking, freeze-thaw cycle, pH changes, and light.[9] Although mAb aggregation has been extensively studied using a range of analytical and biophysical techniques, the underlying mechanisms are still not well understood.[10,11]

Protein aggregation is usually initiated by two monomers self-associating to form a dimer, which may further accumulate into larger oligomers and aggregates. Different IgG subclasses under

different stress conditions can form dimers of various structures, suggesting different aggregation pathways.[12–14] For example, a 'bone-like' dimer structure is observed by TEM for process stressed IgG1 whereas the pH stressed IgG1 dimer has a 'close' conformation where two monomers are attached to each other via two interaction sites.[12] HDX-MS analysis of Bevacizumab aggregates induced from multiple freeze/thaw cycles were observed to possess exchange profiles indistinguishable from native mAbs, whereas a similar analysis of thermally-induced aggregates revealed large changes in exchange behavior within mAb CDR regions.[13] Native MS is also a useful tool for characterizing mAb aggregates, as the noncovalent protein-protein interactions can be preserved during nESI process.[15] Coupled with IM separation and gas-phase unfolding, native MS may provide us more insights into the structure of antibody oligomers and elucidate the aggregation pathways. Native IM-MS analysis detected higher abundance of fragments, dimer, and trimer species for humidity-stressed infliximab products in comparison with non-stressed samples. (Chapter 5) Preliminary IM-MS data were collected for an antibody standard after H_2O_2 oxidation and heat-stress. It is interesting to note that we observed increased levels of mAb fragments, as well as very similar level of mAb dimers in stressed sample compared to the control mAb data. CIU fingerprints of the mAb monomers revealed minor structural changes induced by stress.

These experiments were conducted in the ammonium acetate buffer which is amenable to native MS ionization but not pharmaceutical-relevant. Thus, refined forced degradation studies should be performed for mAbs in the commonly used biopharmaceutical formulations under stress conditions that are well-controlled. Stressed mAb monomers and oligomers can be separated and enriched, and then subjected to a set of structural MS analyses, such as bottom-up/top-down sequencing, native IM-MS, gas-phase unfolding, and chemical labeling MS. Information on mAb

primary structure, PTMs, HOS, P-P interactions and stabilities can be extracted from MS datasets. Future efforts should be made to combine all structural MS data with other biophysical characterization to build the mechanistic understanding of mAb aggregation, and ultimately allow the quick differentiation of distinct types of oligomers and the identification of aggregation prone molecules.

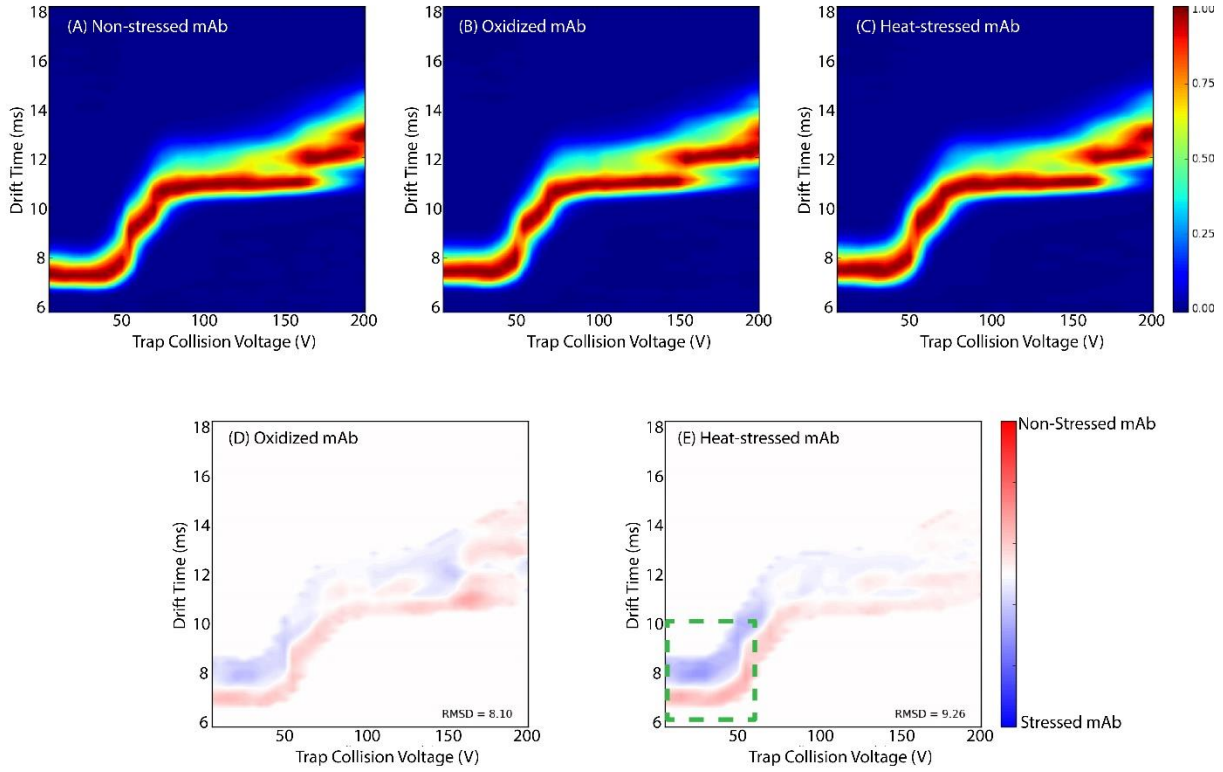

Figure 7-1. CIU fingerprints for (A) non-stressed mAb control, (B) H_2O_2 oxidized mAb, and (C) heat-stressed mAb. Difference plots reveal gas-phase unfolding changes across all energy region for oxidized mAb (D), whereas major structural changes are observed at lower energy region for heat-stressed mAb(E).

7.2.2 Native IM-MS and CIU for characterizing next generation mAb therapeutics

The therapeutic antibody market is expected to be reshaped by several next generation mAb-related therapeutics, such as ADCs[16,17] and bispecific antibodies (bsAbs)[18]. As these therapeutic constructs are often achieved through multiple chemical strategies, they exhibit large amounts of structural heterogeneity and thus pose more challenges for drug development. (Figure 7-2) For instance, ADCs are tripartite molecules with potent small molecule drugs conjugating to the mAb

via chemical linkers. Conjugation can occur either at cysteine residues or lysine residues using diverse chemistries. Different conjugation strategies may affect the structure, stability and biological activity of ADCs.[19] Our CIU data suggests that structure and stability changes occur within mAbs upon biotin conjugation at lysine residues. (Chapter 4)

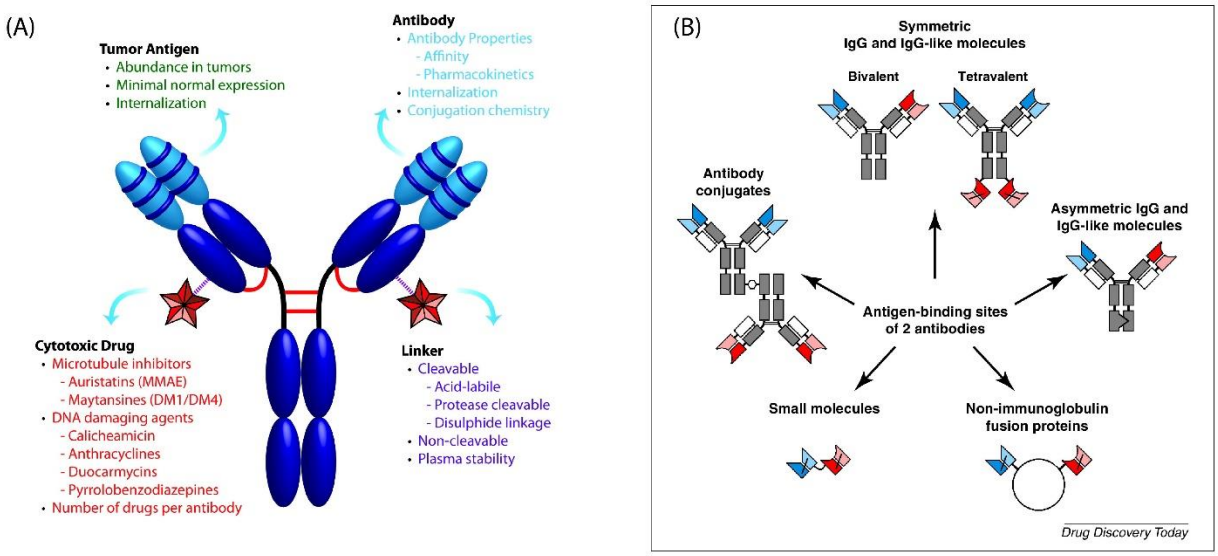

Figure 7-2. (A) Key structural components of ADCs that affect their performances. (Reused from Ref. 16., DOI: 10.4161/mabs.27022. Copyright © 2014 Landes Bioscience) Optimization of these components are essential. (B) A Schematic showing different strategies used to generate bispecific antibodies (bsAbs) derived from the antigen-binding sites of two different antibodies. (Reused from Ref. 18, DOI: 10.1016/j.drudis.2015.02.008. Copyright © 2015 Roland E. Kontermann,Ulrich Brinkmann. Published by Elsevier Ltd.)

Work moving forward should establish CIU protocols to determine the structure and stability of mAbs influenced by diverse linkers, conjugation sites, and small molecule structures. Another mAb-related therapeutic class of interest is bsAbs, which combine specificities of two antibodies and simultaneously address different antigens or epitopes. The production of this therapeutic class may result in molecules with incorrect subunit linkages, further the increasing necessity for exhaustive characterization. Native MS combined with IM separation have been used to monitor the Fab-arm exchange, which represents one strategy for bsAb formation.[20] Continuing development of native IM-MS and CIU techniques will clearly advance the growth of this appealing class of therapeutics.

7.2.3 CIU as high-throughput assays for structure and stability characterization in biopharmaceutical discovery and development

The sensitivity of CIU to structural differences induced by PTMs such as disulfide bond and glycosylation has been evaluated in Chapters 2 and 3. Future work should aim to move beyond the model systems studied here and build a broad "antibody CIU fingerprint database" that seeks to classify mAb CIU data in pursuit of better quantifying the impact of different primary structures and PTMs on protein gas-phase structures and stabilities. Obtaining large numbers of antibody sequences to build this database will certainly require collaborations across multiple labs in both academia and industry. Once sufficient samples are acquired, major challenges win high-throughput sample delivery and data interpretation will need to be overcome to generate a sufficient CIU database. Integrating the automated sample handling and high-throughput sample delivery systems, such as microfluidic devices, with current CIU workflows will clearly facilitate CIU database construction and expand the applications of native IM-MS and CIU approaches generally.

Evaluation of the sensitivity and resolution of CIU is also essential for developing this technique into a robust assay that can rapidly quantify mAb PTMs and identify unknown impurities. After CIU fingerprint database creation, more IM-MS case studies of antibody mixtures should be conducted to quantitatively characterize the capacity of CIU resolving structural distinct antibodies. Data analysis will likely present a range of challenges, as protein mixtures may result in convoluted CIU fingerprints. Continuing software development for multiple feature detection and quantification will undoubtedly enhance the sensitivity of CIU assays.

Furthermore, since CIU fingerprints reflect the stabilities of proteins in the gas phase upon collision activation, CIU assays can potentially be deployed as a stability-screening tool in

biopharmaceutical discovery and development. DSC is commonly used in the pharmaceutical industry for protein stability analysis by measuring heat capacity changes associated with mAb unfolding at elevated temperatures. DSC and CIU measurements of mAb-biotin conjugates (Chapter 4) have shown that both assays can detect destabilization caused by biotin conjugation. Thus, it would be informative to collect a broader range of DSC and CIU data for antibody sequences with various modifications and formulations. If any correlation between the solution-phase and gas-phase stabilities can be drawn from the melting temperature (T_m) derived from DSC thermograms and the transition voltages observed by CIU, then rapid CIU analyses can be implemented as a robust technique for mAb stability assessments to select optimized drug candidates.

7.3 References

(1) Walsh, G. *Nat. Biotechnol.* **2014**, *32* (10), 992–1000.
(2) Ecker, D. M.; Jones, S. D.; Levine, H. L. *MAbs* **2015**, *7* (1), 9–14.
(3) Barton, C.; Spencer, D.; Levitskaya, S.; Feng, J.; Harris, R.; Schenerman, M. A. In *State-of-the-Art and Emerging Technologies for Therapeutic Monoclonal Antibody Characterization Volume 1. Monoclonal Antibody Therapeutics: Structure, Function, and Regulatory Space*; ACS Symposium Series; American Chemical Society, 2014; Vol. 1176, pp 3–69.
(4) Beck, A.; Debaene, F.; Diemer, H.; Wagner-Rousset, E.; Colas, O.; Dorsselaer, A. Van; Cianférani, S. *J. Mass Spectrom.* **2015**, *50* (2), 285–297.
(5) Rathore, D.; Faustino, A.; Schiel, J.; Pang, E.; Boyne, M.; Rogstad, S. *Expert Rev. Proteomics* **2018**, 14789450.2018.1469982.
(6) Masson, G. R.; Jenkins, M. L.; Burke, J. E. *Expert Opin. Drug Discov.* **2017**, *12* (10), 981–994.
(7) Wei, H.; Mo, J.; Tao, L.; Russell, R. J.; Tymiak, A. A.; Chen, G.; Iacob, R. E.; Engen, J. R. *Drug Discov. Today* **2014**, *19* (1), 95–102.
(8) Shire, S. J.; Shahrokh, Z.; Liu, J. *J. Pharm. Sci.* **2004**, *93* (6), 1390–1402.
(9) Chaudhuri, R.; Cheng, Y.; Middaugh, C. R.; Volkin, D. B. *AAPS J.* **2013**, *16* (1), 48–64.
(10) Li, W.; Prabakaran, P.; Chen, W.; Zhu, Z.; Feng, Y.; Dimitrov, D. *Antibodies* **2016**, *5* (3), 19.
(11) Roberts, C. J. *Trends Biotechnol.* **2014**, *32* (7), 372–380.
(12) Paul, R.; Graff-Meyer, A.; Stahlberg, H.; Lauer, M. E.; Rufer, A. C.; Beck, H.; Briguet, A.; Schnaible, V.; Buckel, T.; Boeckle, S. *Pharm. Res.* **2012**, *29* (8), 2047–2059.
(13) Zhang, A.; Singh, S. K.; Shirts, M. R.; Kumar, S.; Fernandez, E. J. *Pharm. Res.* **2012**, *29* (1), 236–250.

(14) Arosio, P.; Rima, S.; Morbidelli, M. *Pharm. Res.* **2013**, *30* (3), 641–654.
(15) Kükrer, B.; Filipe, V.; Van Duijn, E.; Kasper, P. T.; Vreeken, R. J.; Heck, A. J. R.; Jiskoot, W. *Pharm. Res.* **2010**, *27* (10), 2197–2204.
(16) Panowski, S.; Bhakta, S.; Raab, H.; Polakis, P.; Junutula, J. R. *MAbs* **2014**, *6* (1), 34–45.
(17) Beck, A.; Goetsch, L.; Dumontet, C.; Corvaïa, N. *Nat. Rev. Drug Discov.* **2017**, *10* (5), 345–352.
(18) Kontermann, R. E.; Brinkmann, U. *Drug Discov. Today* **2015**, *20* (7), 838–847.
(19) Acchione, M.; Kwon, H.; Jochheim, C. M.; Atkins, W. M. *MAbs* **2012**, *4* (3), 362–372.
(20) Debaene, F.; Wagner-Rousset, E.; Colas, O.; Ayoub, D.; Corvaïa, N.; Van Dorsselaer, A.; Beck, A.; Cianférani, S. *Anal. Chem.* **2013**, *85* (20), 9785–9792.

Appendix I. Supporting Information for Chapter 2.

Table I-1. Uniprot entry identifier numbers for human IgG subtype constant regions.

Protein Names	Entry
Ig gamma-1 chain C region	P01857
Ig gamma-2 chain C region	P01859
Ig gamma-3 chain C region	P01860
Ig gamma-4 chain C region	P01861

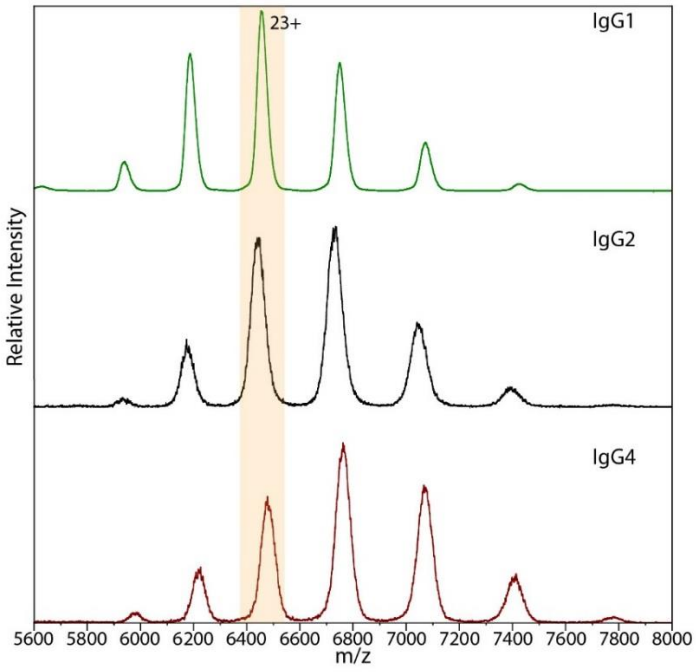

Figure I-1. MS spectra for human IgG1κ, IgG2κ, and IgG4κ. 23^{+} ions are selected for CIU analysis.

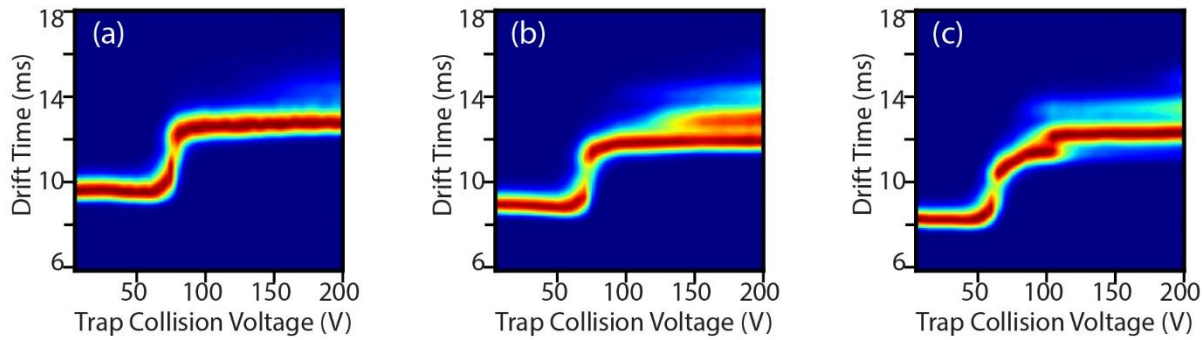

Figure I-2. CIU fingerprints for various charge states of IgG1κ. 22+ ions (a) only exhibit one unfolded state, whereas both 23+ (b) ions and 24+ ions (c) occupy two unfolded states and an additional low intensity fourth feature.

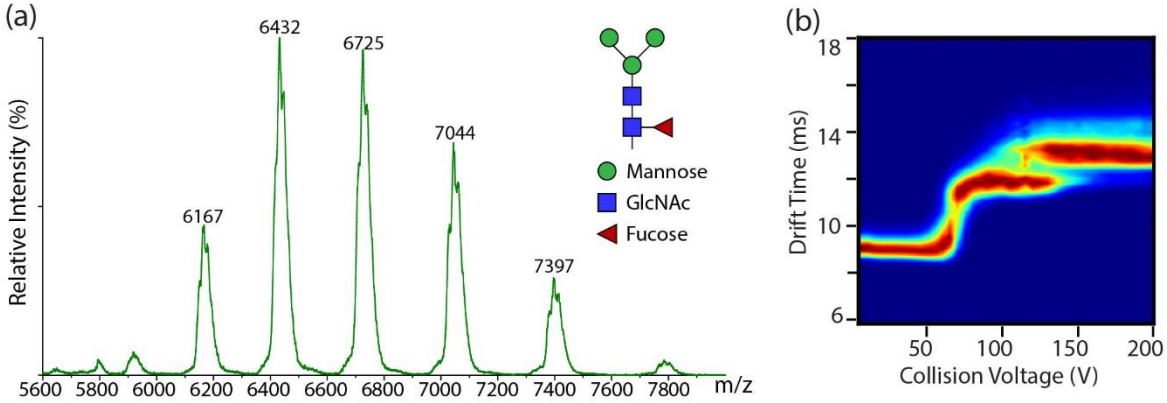

Figure I-3. (a) MS spectrum of Waters intact mAb check standard upon removal of N-Acetylglucosamine (GlcNAc) from the N-linked glycans (shown on the right upper comer). (b) CIU fingerprints for the 23+ ions of this mAb glycoform exhibit very similar gas phase unfolding pathways to that of mAb glycoform mixtures.

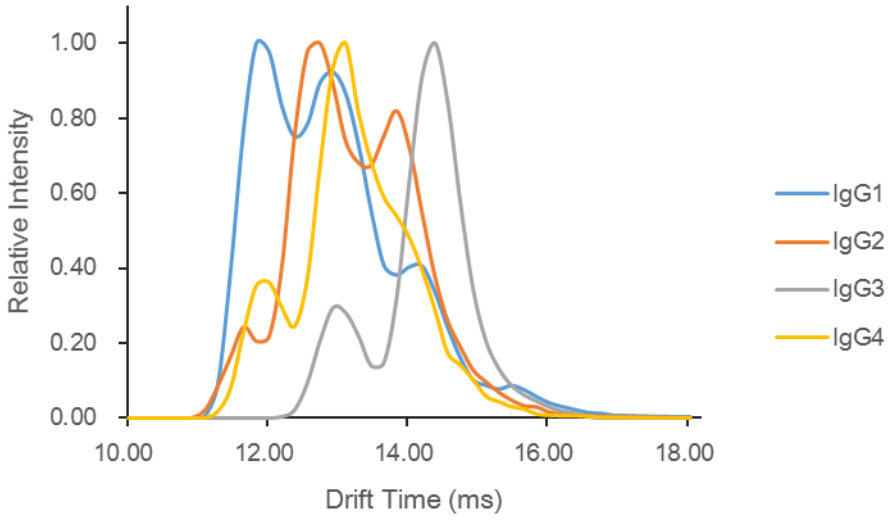

Figure I-4. An overlay of IM spectra for IgG subtypes at 200 V trap collision voltage.

Appendix II. Supporting Information for Chapter 3

Table II-1. Experimental masses for IgG monomer glycoforms.

Glycoform	Experimental Mass (Da)	Sequence Mass (Da)
Native	147488.2 ± 18.7	-
$(G0F)_2$	147472.8 ± 26.0	146658.4
$(M3N2F)_2$	147091.0 ± 28.5	145845.6
$(M1N2F)_2$	146258.6 ± 20.3	145197.0
$(N1F)_2$	145036.7 ± 25.3	144466.4
Deglycosylated	144670.0 ± 30.0	143767.7

Table II-2. Experimental masses for IdeS digest IgG glycoforms.

Glycoform	Fc		$F(ab')_2$	
	Experimental Mass (Da)	**Sequence Mass (Da)**	**Experimental Mass (Da)**	**Sequence Mass (Da)**
Native	50567.3 ± 2.2	-	96651.2 ± 32.7	96305.5
$(G0F)_2$	50524.2 ± 9.9	50398.3	96692.0 ± 32.0	
$(M3N2F)_2$	49707.4 ± 27.9	49585.6	96642.2 ± 61.0	
$(M1N2F)_2$	49043.4 ± 21.0	48937.0	96652.2 ± 70.5	
$(N1F)_2$	48343.8 ± 19.8	48206.3	96557.4 ± 29.4	
Deglycosylated	47513.02 ± 4.3	47507.7	96652.2 ± 70.5	

Table II-3. CIU features for IgG monomers output from CIUSuite_Detect. (Savitsky-Golay Smoothing Filter = 5, Intensity Threshold = 90, Scaling Factor = 2.)

Glycoform	Feature 1 Centroid Voltage (V)	Feature 1 Stability (V)	Feature 1 Drift Time (ms)
Native	35	60	9.1
$(G0F)_2$	35	60	9.1
$(M3N2F)_2$	35	60	9.1
$(M1N2F)_2$	35	60	8.918
$(N1F)_2$	32.5	55	8.827
Deglycosylated	32.5	55	8.645
	Feature 2 Centroid Voltage (V)	**Feature 2 Stability (V)**	**Feature 2 Drift Time (ms)**
Native	95	40	11.557
$(G0F)_2$	97.5	45	11.648
$(M3N2F)_2$	97.5	45	11.648
$(M1N2F)_2$	92.5	35	11.648
$(N1F)_2$	87.5	25	11.648
Deglycosylated	87.5	25	11.648
	Feature 3 Centroid Voltage (V)	**Feature 3 Stability (V)**	**Feature 3 Drift Time (ms)**
Native	157.5	85	12.831
$(G0F)_2$	162.5	75	12.922
$(M3N2F)_2$	160	80	13.013
$(M1N2F)_2$	157.5	85	12.922
$(N1F)_2$	150	100	12.831
Deglycosylated	150	100	12.649

Table II-4. CIU features for IgG Fc fragments output from CIUSuite_Detect. (Savitsky-Golay Smoothing Filter = 5, Intensity Threshold = 90, Scaling Factor = 2.)

Glycoform	Feature 1 Centroid Voltage (V)	Feature 1 Stability (V)	Feature 1 Drift Time (ms)
Native	22.5	35	6.417
$(G0F)_2$	22.5	35	6.417
$(M3N2F)_2$	22.5	35	6.417
$(M1N2F)_2$	22.5	35	6.348
$(N1F)_2$	20	30	6.31
Deglycosylated	20	30	6.003
	Feature 2 Centroid Voltage (V)	**Feature 2 Stability (V)**	**Feature 2 Drift Time (ms)**
Native	85	50	8.418
$(G0F)_2$	85	50	8.418
$(M3N2F)_2$	82.5	40	8.418
$(M1N2F)_2$	80	30	8.349
$(N1F)_2$	70	30	8.28
Deglycosylated	70	30	8.073
	Feature 3 Centroid Voltage (V)	**Feature 3 Stability (V)**	**Feature 3 Drift Time (ms)**
Native	130	20	9.867
$(G0F)_2$	130	20	9.867
$(M3N2F)_2$	127.5	25	9.798
$(M1N2F)_2$	125	30	9.798
$(N1F)_2$	117.5	45	9.729
Deglycosylated	117.5	45	9.591

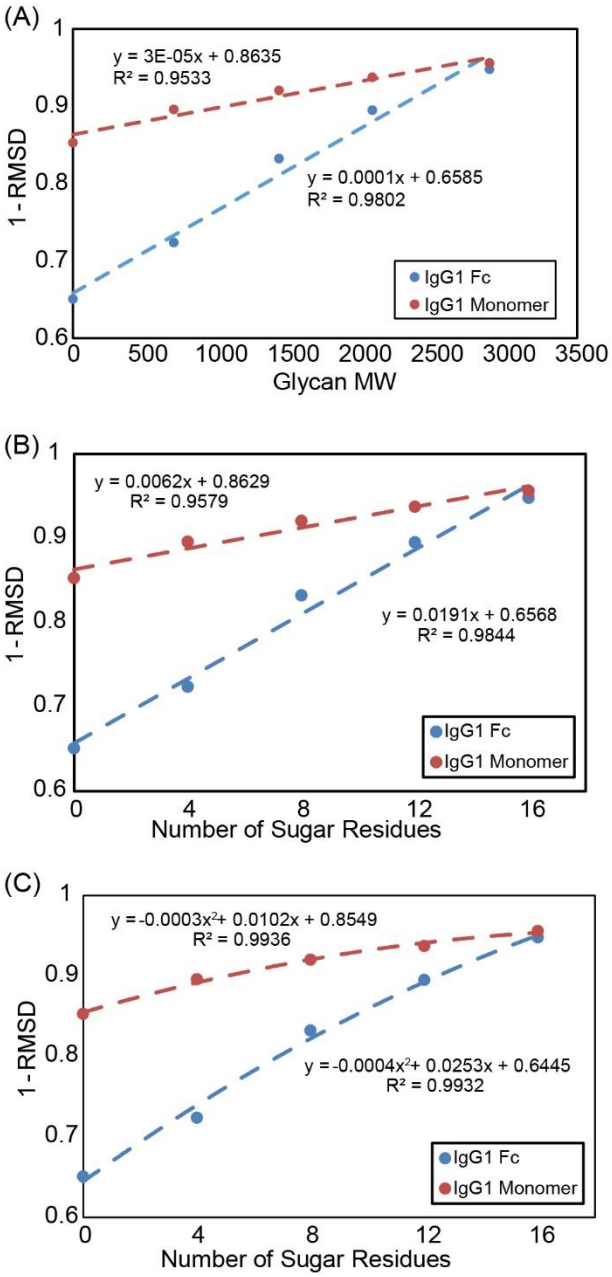

Figure II-1. (A) Plot of 1-RMSD values against the molecular weight of N-linked glycans attached in the antibody Fc region. Data is fitted to a linear relationship, generating an R^2 value of < 0.99. (B) Plot of 1-RMSD values against the number of sugar residues remaining in the N-linked glycans attached to the antibody Fc region. Data is fitted into a linear function. (C) Plot of 1-RMSD values against the number of sugar residues remaining in the N-linked glycans attached to the antibody Fc region. Data is fitted to a quadratic function.

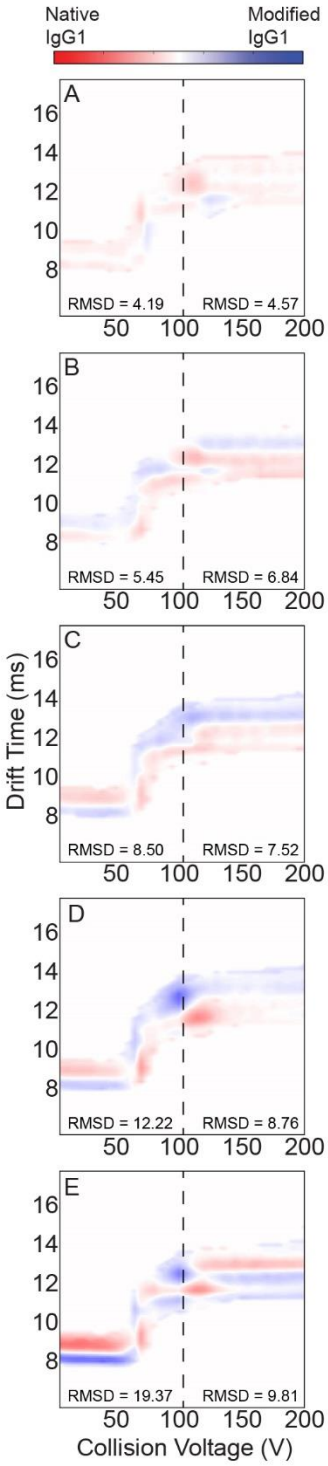

Figure II-2. CIU difference plots comparing intact antibody ions that have native glycosylation patterns (red) and Fc $(G0F)_2$ glycoforms (A, blue), $(M3N2F)_2$ glycoforms (B, blue), $(M1N2F)_2$ glycoforms (C, blue), $(N1F)_2$ glycoforms (D, blue), and completely deglycosylated IgG1 (E, blue). RMSD values are calculated for both lower energy regions where trap collision voltages are below 100 V, and high energy regions at collision voltages above 100 V.

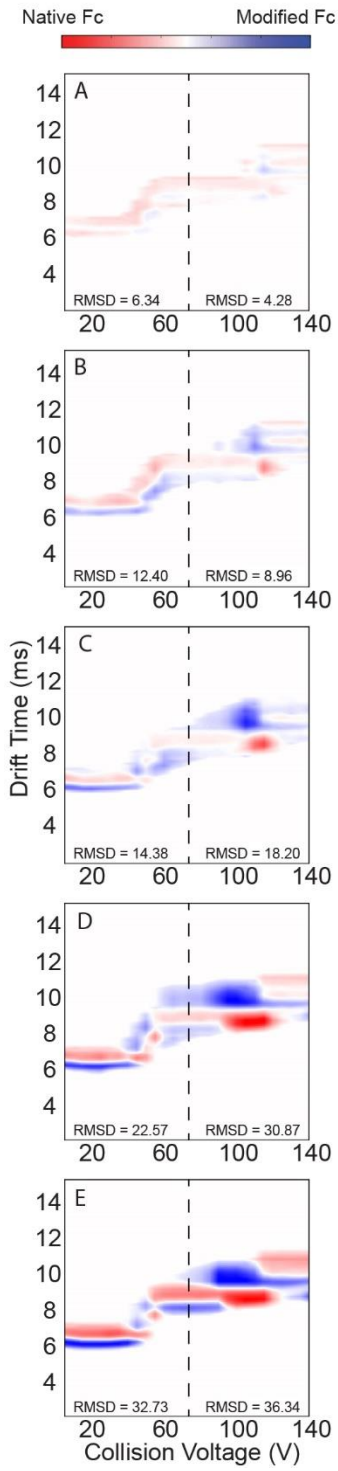

Figure II-3. CIU difference plots that compare Fc fragments that bear native glycosylation (red) and Fc $(G0F)_2$ glycoforms (A, blue), $(M3N2F)_2$ glycoforms (B, blue), $(M1N2F)_2$ glycoforms (C, blue), $(N1F)_2$ glycoforms (D, blue), and completely deglycosylated IgG1 (E, blue). RMSD values are calculated for both lower energy regions where trap collision voltages are below 75 V and high energy regions at collision voltages above 75 V.

Appendix III. Supporting Information for Chapter 4

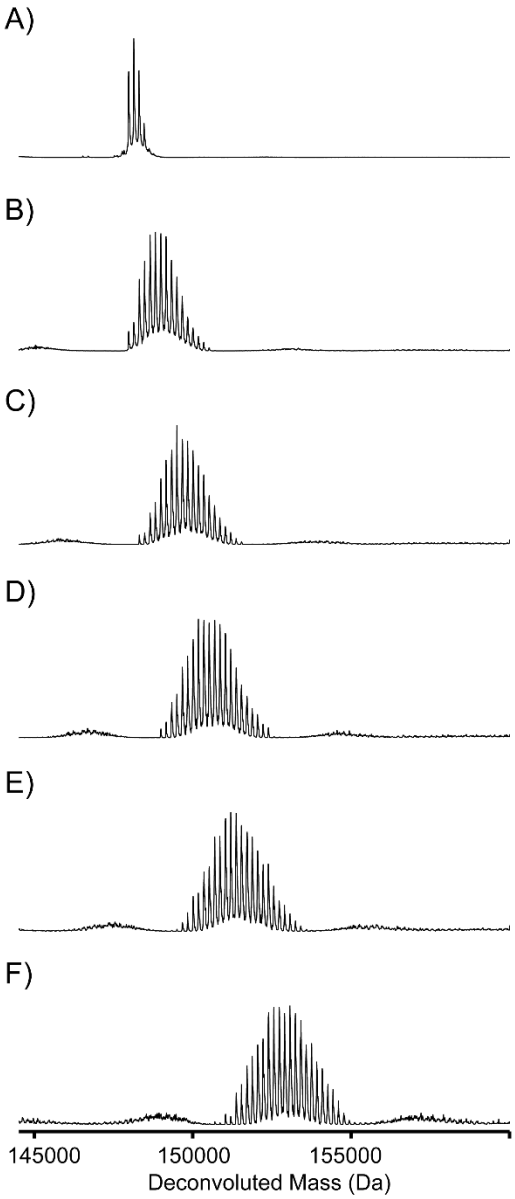

Figure III-1. (A) Deconvoluted mass spectrum for glycosylated parent mAb recorded from denaturing LC-MS analysis. Antibody glycoforms are resolved. (B-F) Deconvoluted mass spectra for the biotinylated mAbs with intact glycosylation.

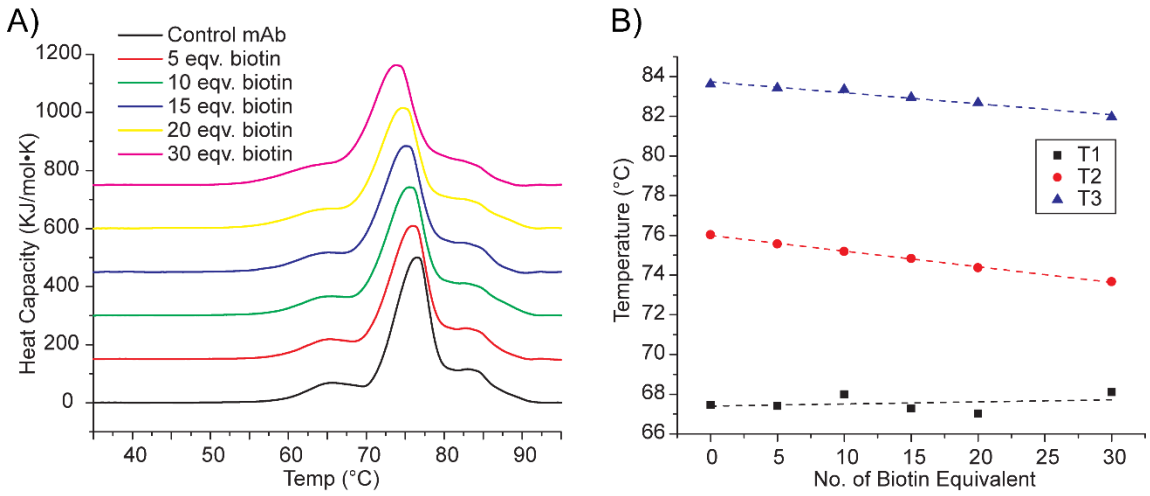

Figure III-2. (A) Overlay of the baseline subtracted DSC thermograms for the biotinylated mAbs after the removal of N-linked glycosylation. (B) The transition temperatures extracted from the DSC thermograms plotted as a function of biotin equivalents reacted with the mAb.

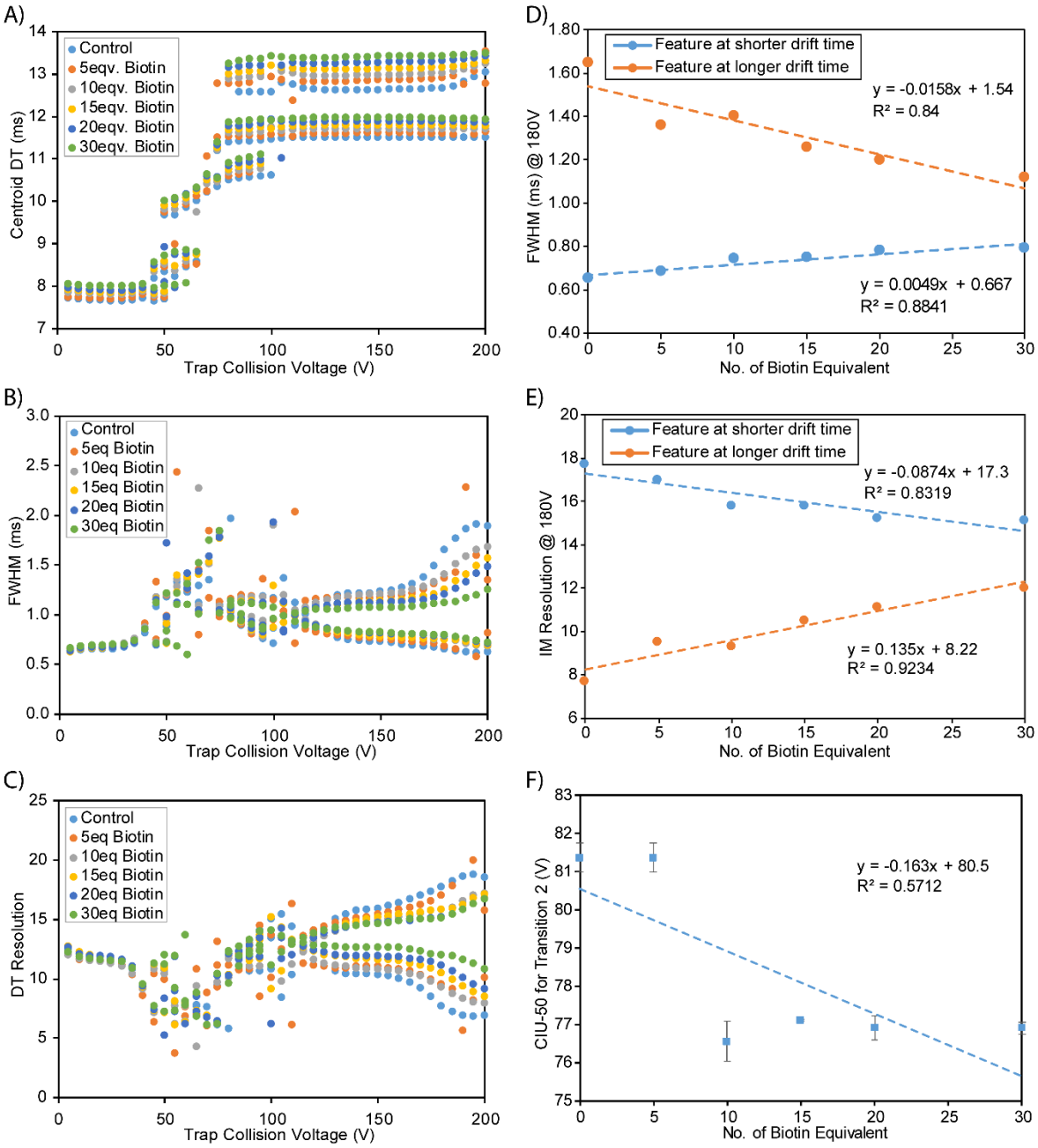

Figure III-3. CIU width analysis results. (A) Centroid drift times (DT), (B) full-width at half maximum (FWHM), and (C) the IM drift time resolution of the protein arrival time distributions were determined from the Gaussian fitting results and plotted against the trap collision voltage. Data for each sample is color-coded. (D) FWHM and (E) IM resolution for biotinylated mAbs at trap collision voltage of 180V. (F) CIU-50 values for another batch of ADC mimics prepared on different days from the samples used in the main text, plotted against the number of biotin equivalent.

Table III-1. Travelling wave ion mobility (TWIM) derived CCS values in nitrogen, RF-confining drift cell measured CCS values in helium, and SEC-MALS/QELS determined hydrodynamic radius.[a]

	Ω_{N2} (nm^2)	Ω_{He} (nm^2)	R_h (nm)
Glycosylated			
parent mAb	76.2 ± 0.8	70.32 ± 0.28	5.06 ± 0.1
mAb + 5eqv. biotin	76.0 ± 0.7	70.24 ± 0.47	5.17 ± 0.1
mAb + 10 eqv. biotin	76.8 ± 0.4	70.91 ± 0.38	5.11 ± 0.1
mAb + 15 eqv. biotin	77.3 ± 1.0	72.32 ± 0.60	5.10 ± 0.1
mAb + 20 eqv. biotin	77.2 ± 0.9	68.94 ± 0.39	5.11 ± 0.1
mAb + 30 eqv. biotin	77.8 ± 1.0	71.66 ± 0.48	5.10 ± 0.1
Deglycosylated			
parent mAb	75.0 ± 0.7	69.34 ± 0.57	5.04 ± 0.1
mAb + 5eqv. biotin	75.1 ± 0.7	69.34 ± 0.57	5.16 ± 0.1
mAb + 10 eqv. biotin	75.4 ± 0.6	70.04 ± 0.43	5.12 ± 0.1
mAb + 15 eqv. biotin	75.8 ± 0.9	70.38 ± 0.17	5.10 ± 0.1
mAb + 20 eqv. biotin	75.9 ± 0.6	70.04 ± 0.40	5.07 ± 0.1
mAb + 30 eqv. biotin	76.2 ± 0.6	71.17 ± 0.23	5.13 ± 0.1

a. CCS values are averaged from all charge states.

Table III-2. CIU-50 analysis results for glycosylated ADC models.[a]

	Transition 1(V)	Transition 2 (V)
parent mAb	57.0 ± 0.3	87.8 ± 2.5
mAb + 5eqv. biotin	57.0 ± 0.2	81.7 ± 0.0
mAb + 10 eqv. biotin	56.7 ± 0.1	83.1 ± 1.9
mAb + 15 eqv. biotin	56.9 ± 0.2	82.4 ± 0.4
mAb + 20 eqv. biotin	56.6 ± 0.0	81.8 ± 0.0
mAb + 30 eqv. biotin	56.8 ± 0.1	78.3 ± 1.9

a. CIU-50 values are averaged from triplicate CIU datasets.

Appendix IV. Supporting Information for Chapter 5

IV.1 Liquid Chromatography-Mass Spectrometry Experiment

IV.1.1 Enzymatic Digestion

Tryptic Digest Antibody tryptic digests were prepared according to the procedure for the low-pH protein digestion kit (Promega, CAS Registry No. CS1895A1). Antibody samples were denatured in 8 M urea, reduced, and alkylated with iodoacetamide. The samples were diluted 7-fold and mixed with Trypsin Gold and Lys-C (Promega) in a 20:1:1 (w/w/w) ratio. Samples were digested overnight at 37 °C and acidified with TFA prior to analysis.

Glu-C Digest. Antibody samples were denatured, reduced, and alkylated as described above. Then the reaction mixtures were diluted 4-fold with 130 mM ammonium bicarbonate (pH 7.8) and 0.027% ProteaseMAX surfactant buffer and digested with Glu-C (Promega) at a 5:1 (w/w) ratio overnight at 37 °C. The digests were acidified by addition of TFA to a final concentration of 1%, and particulate material was removed via centrifugation at 16000*g*.

Deglycosylation and Reduction. For liquid chromatography–mass spectrometry (LC–MS) analysis, 40 μg of antibody was incubated with 4 μL of PNGase F (Promega) for 3 h at 37 °C. Reduction was performed by adjusting the volume to 100 μL with 10 mM DTT in 25 mM NH_4HCO. The sample was acidified with TFA prior to analysis. Deglycosylated mAb samples

IV.1.2 LC-MS

Intact mAb Analysis

Five micrograms of each sample was analyzed by LC–MS using a C4 column (Waters Xbridge BEH300 3.5 μm) interfaced with a ThermoFisher Q Exactive HF mass spectrometer. Data were acquired in the range of *m*/*z* 600–2000 using the Orbitrap for detection.

Peptide Mapping

Five hundred nanograms of each digested sample was analyzed by nano UPLC–MS/MS with a Proxeon EASY-nLC 1000 HPLC system interfaced with a ThermoFisher Q Exactive HF mass spectrometer. Peptides were loaded on a trapping column and eluted over a 75 μm × 50 cm analytical column (Thermo Fisher P/N ES-803) at a rate of 300 nL/min by using a 2 h reverse phase gradient; both columns were packed with PepMap LC C18, 2 μm resin. The mass spectrometer was operated in data-dependent mode, with MS and MS/MS performed in the Orbitrap at 70000 and 17500 full width at half-maximal resolutions, respectively. The 15 most abundant ions were selected for MS/MS.

IV.2 Size Exclusion Chromatography (SEC)

SEC was performed using a Waters Alliance HPLC system equipped with UV detector set at 220 nm. A TSK Gel 3000 SW_{xl} column (Tosoh, 7.8 mm × 30 cm, 5 μm) was used to perform the separation. The mobile phase [PBS (pH 7.4)] was delivered at a rate of 1 mL/min. Samples were filtered with a 0.45 μm filter (Millipore), and a 25 μL injection volume was used.

IV.3 FcγRIIIa Binding Assessed via Biolayer Interferometry (BLI)

The binding of different lots of RC and RS with FcγRIIIa was tested by BLI using a BLITZ instrument (Fortebio, Menlo Park, CA). The procedure used here was adopted from the method reported previously.[1,2] Protein G biosensor tips were utilized, and the binding measurement was performed at 25 °C. Samples were diluted to 0.8 μM mAb with kinetic buffer (PBS buffer containing 1 mg/mL casein as a blocking agent). The protein G biosensor tips were loaded (120 s) with the RC or RS samples. A baseline (240 s) was established followed by the association (180 s) and dissociation (360 s) of FcγRIIIa measured by dipping the biosensor into solutions of FcγRIIIa (FcγRIIIa-V158 variant) and PBS kinetic buffer, respectively. The biosensor tips were regenerated as described previously[2] after each assay cycle. To determine the dissociation constant (K_D) for the different lots of RC and RS, a range of FcγRIIIa concentrations from 0.4 to 3.2 μM were evaluated. Data generated were collected in triplicate for each lot and globally fitted to a 1:1 binding model using BLITZ Pro software to calculate k_a, k_d, and K_D.

References:

(1) Alsenaidy, M. A.; Okbazghi, S. Z.; Kim, J. H.; Joshi, S. B.; Middaugh, C. R.; Tolbert, T. J.; Volkin, D. B. *J. Pharm. Sci.* **2014**, *103* (6), 1613–1627.

(2) Okbazghi, S. Z.; More, A. S.; White, D. R.; Duan, S.; Shah, I. S.; Joshi, S. B.; Middaugh, C. R.; Volkin, D. B.; Tolbert, T. J. *J. Pharm. Sci.* **2016**, *105* (2), 559–574.

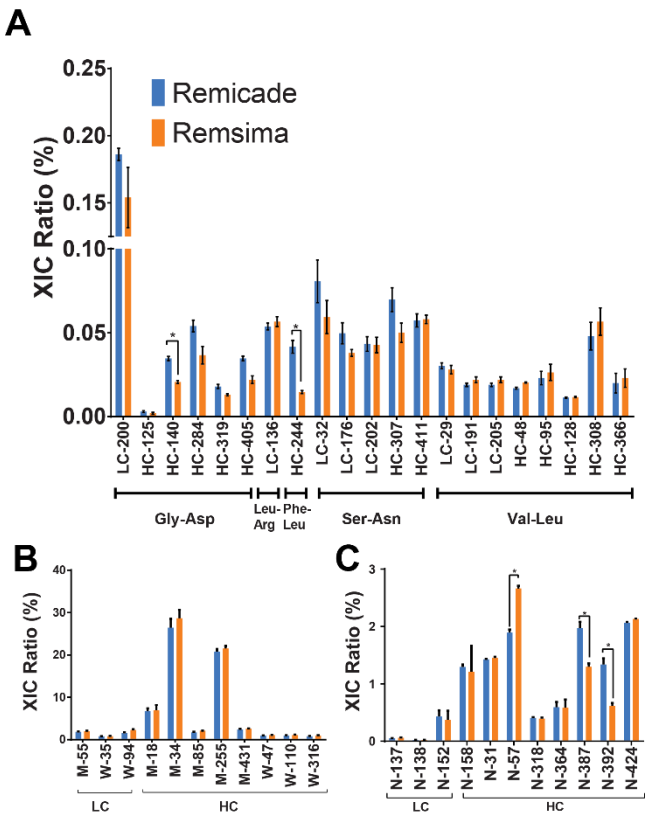

Figure IV-1. LC/MS/MS analysis of trypsin digests of Remicade and Remsima. A, sequence variants B, oxidation and C, deamidation (n = 4 lots, mean ± SEM). (*) denotes significance at $p<0.05$.

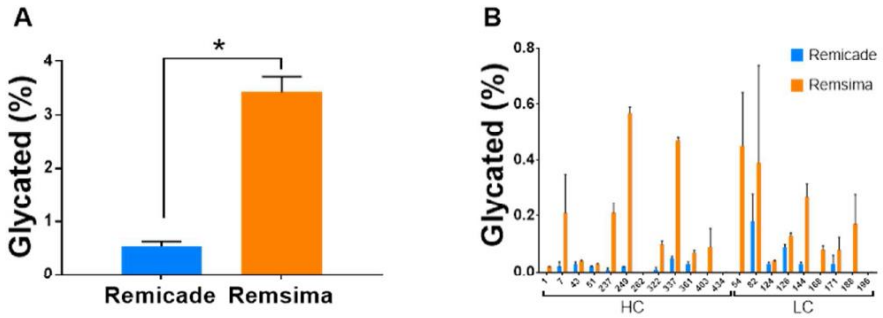

Figure IV-2. Glycation of Remicade and Remsima. A, average sum of percent glycated peptides for Remicade and Remsima peptides after Glu-C digest B, Levels of glycation of specific Lys residues determined after Glu-C digest. (n= 4 lots each, average ± S.D.)

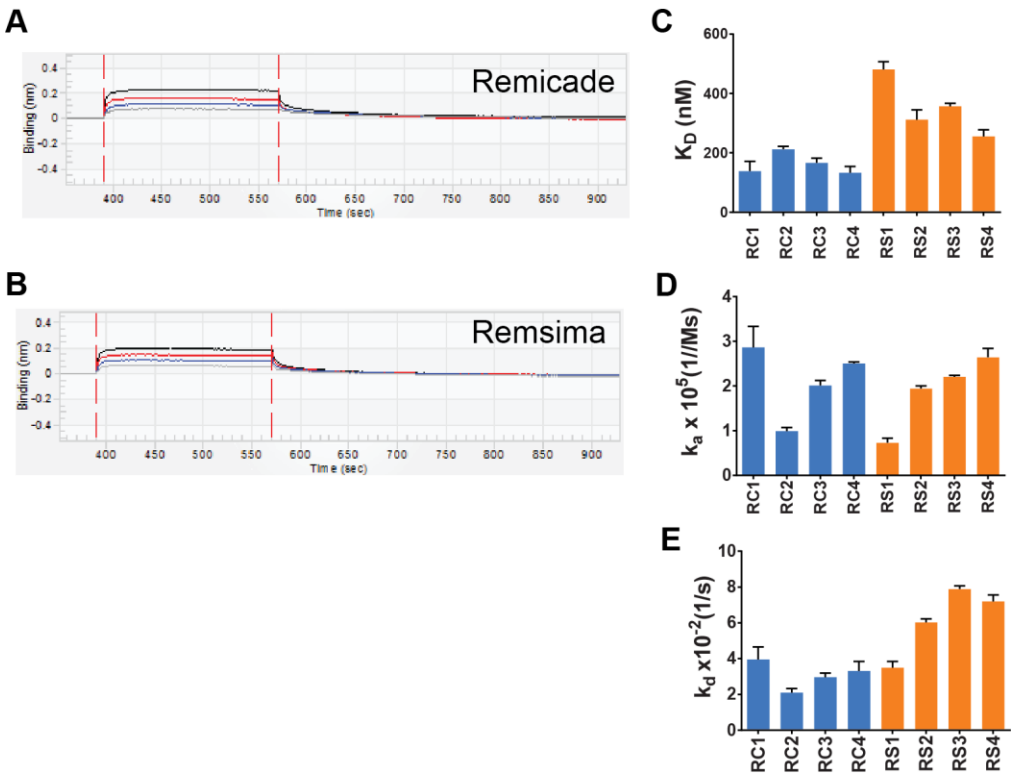

Figure IV-3. Binding kinetics of infliximab samples to FcγRIIIa receptors. Representative binding curves to in vitro FcγRIIIa receptors for a given lot of A, Remicade or B, Remsima measured via biolayer interferometry using BLITZ instrument. Calculated C, equilibrium disassociation (K_D), D, on (k_a), and D, off (k_d) rates for each of the lots of Remicade and Remsima using 1:1 fitting model with BLITZPro software. The data shown are mean ± SEM for each lot of Remicade or Remsima (n = 3 measurements per each lot).

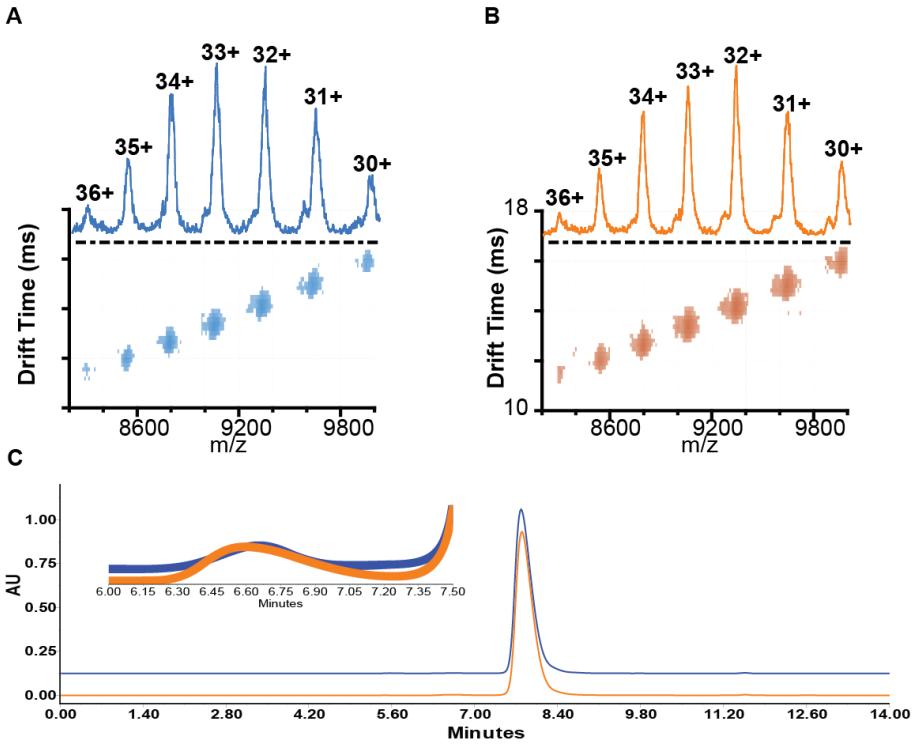

Figure IV-4. Dimers of Remicade and Remsima. Representative IM-MS spectra of dimer species of A, Remicade and B, Remsima with annotated charges. C, Representative size exclusion chromatography (SEC) profiles of Remicade (blue) and Remsima (orange). Inset shows the dimer peaks.

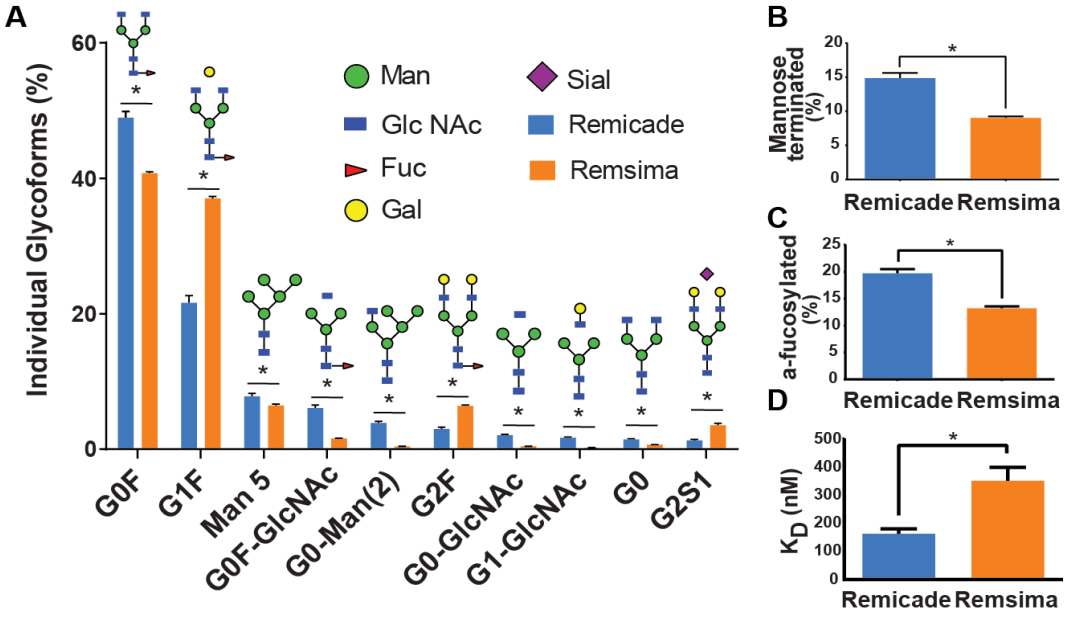

Figure IV-5. Remicade and Remsima glycosylation heterogeneity and FcγR-IIIa binding. A, Quantification of N-glycans following LC/MS/MS analysis of RC B, total mannose terminated forms C, total afucosylated forms. D, Average K_D of RC and RS receptor binding to FcγIIIa as measured by biolayer interferometry (n = 4 lots, mean ± SEM; * denotes significance at $p<0.05$).

Table IV-1. Glycan profiles for Remicade and Remsima

Modifications Name	Abbreviated Name	Remicade Average	Remicade Stdev	Remsima Average	Remsima Stdev
HexNAc(4)Hex(3)Fuc(1)	G0F	48.93%	1.85%	40.74%	0.45%
HexNAc(4)Hex(4)Fuc(1)	G1F	21.63%	2.09%	37.03%	0.55%
HexNAc(2)Hex(5)	Man 5	7.82%	0.85%	6.46%	0.43%
HexNAc(3)Hex(3)Fuc(1)	G0F-Man	6.10%	0.82%	1.60%	0.05%
HexNAc(3)Hex(5)	G0-Man(3)	3.89%	0.43%	0.40%	0.06%
HexNAc(4)Hex(5)Fuc(1)	G2F	2.99%	0.56%	6.41%	0.20%
HexNAc(3)Hex(3)	G0-GlcNAc	2.07%	0.23%	0.43%	0.03%
HexNAc(3)Hex(4)	G1-GlcNAc	1.71%	0.18%	0.22%	0.02%
HexNAc(4)Hex(3)	G0	1.47%	0.16%	0.68%	0.04%
HexNAc(4)Hex(5)Fuc(0)NeuAc(1)	G2S1	1.32%	0.29%	3.56%	0.53%
HexNAc(4)Hex(4)	G1	0.58%	0.14%	0.54%	0.10%
HexNAc(4)Hex(6)Fuc(1)	Bisecting GlcNac-F	0.32%	0.08%	0.50%	0.04%
HexNAc(2)Hex(4)	Man 4	0.16%	0.03%	0.11%	0.01%
HexNAc(2)Hex(6)	Man 6	0.18%	0.03%	0.21%	0.02%
HexNAc(4)Hex(5)Fuc(0)NeuAc(0)NeuGc(2)	G2N2	0.04%	0.07%	0.02%	0.03%
HexNAc(2)Hex(3)	Man 3	0.27%	0.09%	0.41%	0.04%
HexNAc(1)	Man 7	0.10%	0.01%	0.06%	0.02%
HexNAc(2)Hex(3)Fuc(1)	Man 3-F	0.09%	0.01%	0.01%	0.00%
HexNAc(2)Hex(7)	Man 7	0.07%	0.01%	0.08%	0.01%
HexNAc(2)Hex(5)Fuc(1)	Man 5-F	0.04%	0.01%	0.02%	0.01%
HexNAc(4)Hex(5)Fuc(1)NeuAc(0)NeuGc(2)	G2FN2	0.12%	0.05%	0.40%	0.10%
HexNAc(1)Fuc(1)	*	0.04%	0.01%	0.02%	0.00%
HexNAc(2)Hex(8)	Man 8	0.04%	0.01%	0.06%	0.01%
HexNAc(2)Hex(4)Fuc(1)	Man 4-F	0.02%	0.01%	0.00%	0.00%
HexNAc(4)Hex(5)Fuc(1)NeuAc(1)	G2FS1	0.03%	0.00%	0.05%	0.01%
HexNAc(2)Fuc(1)	*	0.00%	0.00%	0.01%	0.00%
HexNAc(4)Hex(5)Fuc(1)NeuAc(1)NeuGc(1)	G2FS1N1	0.00%	0.00%	0.01%	0.00%
HexNAc(4)Hex(5)Fuc(1)NeuAc(2)	G2FS2	0.00%	0.00%	0.00%	0.00%
A-fucosylated		19.70%	1.57%	13.22%	3.75%
Mannose terminated		14.86%	1.53%	9.01%	3.11%
Immunogenic (NANA)		1.35%	0.29%	3.61%	1.32%
Anti-inflammatory (NGNA)		0.17%	0.03%	0.42%	0.18%

Table IV-2 Deamidation levels of Remicade and Remsima before and after 4-week incubation at 40°C and 97% relative humidity

Method	Attribute	Remicade			Remsima		
		0 days	4 weeks	Statistics	0 days	4 weeks	Statistics
LC-MS	Deamidation LC-N_{158}, %	0.6 ± 0.1	7.5 ± 0.7	$P < 0.05$	0.5 ± 0.4	7.5 ± 0.5	$P < 0.05$
	Deamidation HC-N_{57}, %	1.7 ± 0.2	17.6 ± 1.9	$P < 0.05$	2.2 ± 0.1	18.9 ± 0.8	$P < 0.05$
	Deamidation HC-N_{392}, %	1.3 ± 0.1	10.3 ± 1.8	NS	0.5 ± 0.1	11.2 ± 1.5	$P < 0.05$

Table IV-3 Fitted rates of monomer loss for Remicade and Remsima samples after incubation at 40°C and various relative humidity levels.

	Monomer Loss Rate (day^{-1}) ± SD (R^2)		
	50% RH	**75% RH**	**97% RH**
Remsima	-0.19 ± 0.01 (0.99)	-0.23 ± 0.06 (0.86)	-0.42 ± 0.01 (0.99)
Remicade	-0.20 ± 0.01 (0.99)	-0.18 ± 0.03 (0.92)	-0.44 ± 0.01 (0.99)

Appendix V. Supporting Information for Chapter 6

Determining the buffer conditions that promote antibody liquid-liquid phase separations

In order to study the LLPS behavior of Mab4 at high concentrations, we started by screening a series of buffers and visually inspecting the degree of phase separation achieved. Though the design of this experiment is similar to solubility tests typically conducted during formulation development, the purpose is clearly different. We screened various salt concentrations and pH values to determine a formulation in which Mab4 LLPS is observed. Specifically, Mab4 samples at a concentration of 50 mg/mL were dialyzed into a citrate buffer at pH 5.5, with NaCl concentrations ranging from 30 mM to 100 mM. The solution pH of these samples following NaCl addition was ~ 5.3. At room temperature, three out of five of the salt concentrations screened remained homogeneous, whereas the solutions containing 50 mM and 30 mM of NaCl phase separated during dialysis. To promote the LLPS of all protein solutions, the samples were stored at 5 ºC overnight, leading to phase separation in all samples. The phase separation behavior is represented as a mAb-vs.-salt concentration diagram shown in Figure V-1. The trendline shown was fitted using a third-order polynomial function, intended to guide the eye. These results show that Mab samples are more prone to phase separation at low salt concentrations, as evidenced by the higher critical temperature needed to generate the phase transition and larger disparity observed in protein concentration in the phases generated.

We also investigated the impact of pH on LLPS behavior for Mab4. In addition to those discussed above, a further four buffer conditions were screened in our experiments, that included pH values

of 6 and 6.5 generated using a 10 mM citrate buffer, using 50 and 75 mM NaCl concentrations for the lower pH solutions and 30 and 50mM NaCl for the higher. Surprisingly, LLPS was not observed for the Mab4 solutions at pH 6 containing 75 mM NaCl, or at pH 6.5 containing 50 mM NaCl. Proteins in the other two solutions remained as one phase at room temperature, but phase separated after being stored at low temperature. When keeping salt concentration constant at 50mM and increasing the pH from 5.3 to 6, the protein concentration of the low-density phase increased from 7.4 mg/mL to 28 mg/mL and the protein concentration in the higher density phase decreased from 178 mg/mL to 150 mg/mL. In addition to these concentration changes, differences in the solution appearance were observed as well. For example, we observed opalescent qualities for Mab4 solutions present in buffers likely to generate phase separation. Taken together, our results indicate that IgG4 possesses a higher propensity for LLPS at lower pH, salt concentrations and temperatures. It is also noteworthy that the solution viscosity increases at higher protein concentrations, and that handling such viscous protein solutions with precision remains challenging.[1,2] Based on our survey, we chose to work with Mab4 samples prepared in a 10 mM citrate buffer, containing 50 mM NaCl at pH 6 for our HDX-MS experiments.

References:

(1) Yadav, S.; Laue, T. M.; Kalonia, D. S.; Singh, S. N.; Shire, S. J. *Mol. Pharm.* **2012**, *9* (4), 791–802.

(2) Lilyestrom, W. G.; Yadav, S.; Shire, S. J.; Scherer, T. M. *J. Phys. Chem. B* **2013**, *117* (21), 6373–6384.

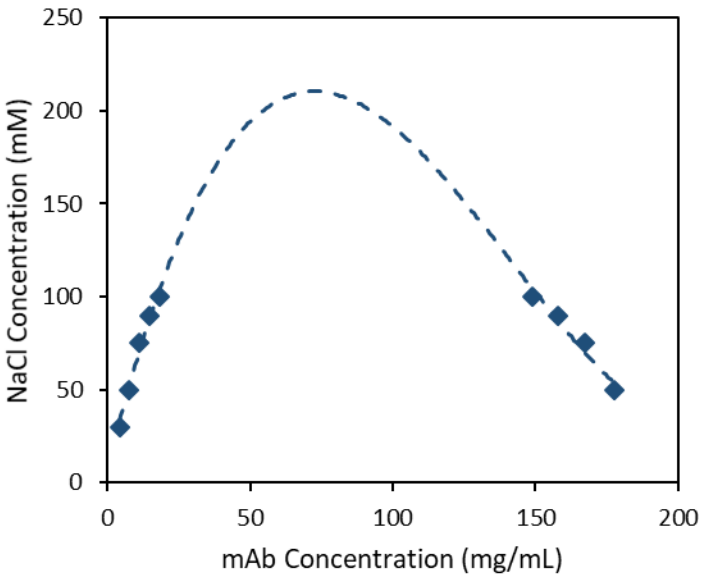

Figure V-1. Phase diagram of Mab4 at 5 ºC in 10 mM citrate buffer at pH 5.3, containing NaCl salt with various concentrations. The trend line was fitted using a third-order polynomial curve. The phase separation region lies below the curve.

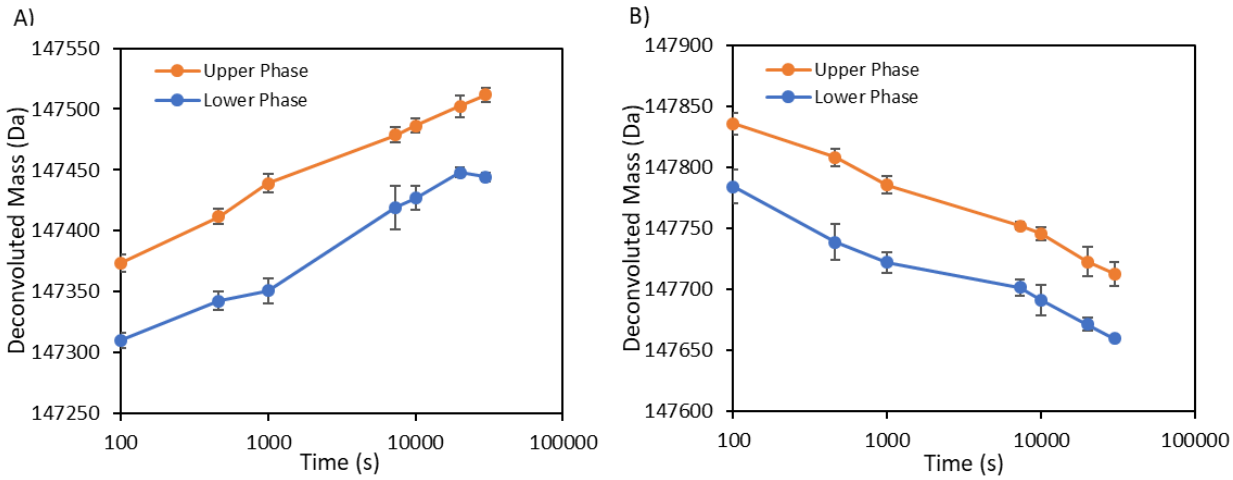

Figure V-2. Intact mAb masses for the Mab4 prepared in H_2O (A) or in D_2O (B) plotted as a function of the HDX reaction time.